UNIVERSITÀ
DEGLI STUDI
DI PADOVA

Sede Amministrativa: Università degli Studi di Padova

Dipartimento di Costruzioni e Trasporti
Centro di Meccanica dei Materiali Biologici

SCUOLA DI DOTTORATO DI RICERCA IN INGEGNERIA INDUSTRIALE

INDIRIZZO DI INGEGNERIA DELLA PRODUZIONE INDUSTRIALE

CICLO XXIV

BIOMECHANICAL ANALYSIS OF THE LIGAMENTS OF THE HINDFOOT: CONSTITUTIVE FORMULATION AND PARAMETERS IDENTIFICATION FOR NUMERICAL MODELLING

Direttore della Scuola: Ch.mo Prof. Paolo Bariani

Coordinatore d'indirizzo: Ch.mo Prof. Enrico Savio

Supervisore: Ch.mo Prof. Arturo N. Natali

Dottorando: Antonella Forestiero

ABSTRACT

The biomechanical behaviour of the hindfoot ligaments is investigated by means of a combined experimental and computational approach. To interpret the typical features of ligaments mechanical response, as anisotropic configuration, geometric non-linearity, non-linear elasticity and time-dependent behaviour, a specific fiber reinforced visco-hyperelastic model is provided. In order to define the constitutive parameters, analytical and numerical models that interpret tensile tests are defined. Model and experimental results are compared by a cost function, whose minimization leads to the optimal set of parameters. In detail the analytical method offers a preliminary set of constitutive parameters. Numerical models that consider the complex histo-morphometric configuration of samples are defined and numerical analyses that interpret the experimental conditions are performed. The analyses assume several sets of constitutive parameters, which are estimated starting from the preliminary set. The minimization of the discrepancy between numerical and experimental results entails the definition of a reliable set of parameters. Once constitutive parameters are evaluated, the biomechanical behaviour of the ligaments of the hindfoot is evaluated in several physiological conditions such as dorsiflexion, plantarflexion and inversion of the foot. This work offers the possibility to interpret and analyse the ankle joint trauma such as the ligaments rupture.

SOMMARIO

Lo studio del comportamento biomeccanico dei legamenti del retro piede ha richiesto un approccio fortemente integrato di tipo computazionale e sperimentale. Al fine di analizzare aspetti tipici della risposta meccanica dei legamenti, come la non linearità per geometria e materiale, la configurazione anisotropa e la dipendenza dal tempo è stato utilizzato un modello visco-iperelastico fibro-rinforzato. La valutazione dei parametri costitutivi ha richiesto lo sviluppo di modelli analitici e numerici capaci di interpretare prove di trazione monoassiale, eseguite su campioni costituiti dal legamento e dalla coppia di ossa congiungenti il legamento stesso. I risultati di modello ed i risultati sperimentali sono stati confrontati attraverso una funzione costo, la cui minimizzazione ha portato alla definizione dei parametri oggetto dello studio. In dettaglio, attraverso l'utilizzo di un modello analitico, è stato possibile definire per ciascun legamento un primo set di parametri. Al fine di interpretare correttamente le reali caratteristiche isto-morfometriche dei tessuti, sono stati sviluppati modelli numerici rappresentativi i campioni sperimentali. Le analisi numeriche sono state eseguite per differenti sets di parametri costitutivi definiti a partire dal set preliminare. La minimizzazione delle discrepanza tra i risultati di modello numerico ed i risultati sperimentali ha condotto alla definizione dei parametri ottimali. Una volta definiti i parametri costitutivi di ciascun legamento, si è andati a studiare il loro comportamento biomeccanico in differenti condizioni fisiologiche: dorsiflessione, plantar-flessione ed inversione del piede. Il lavoro presentato fornisce le basi per la valutazione della funzionalità biomeccanica del retro piede in seguito alla rottura dei legamenti della caviglia.

INDEX

INTRODUCTION

The aim of this work is to develop a computational model of the foot, and in detail of the hindfoot, to investigate the biomechanical behaviour of the ligament tissue. In particular the attention is focused on ankle and subtalar joint for the important function that they cover in human activity such as walking.

The investigation of the biomechanical behaviour of the hindfoot ligaments is a complex problem that requires the analysis of different aspects.

The preliminary step pertains to the morphometric and histological analysis. Morphometry of the hindfoot and, in detail, of its ligaments is investigated through computed tomography, magnetic resonance images and morphometric data from literature. The histological analysis allows to evaluate the tissue micro-structural configuration that is a fundamental tool for the definition of the constitutive model. The hindfoot ligaments tissue is characterised by a hierarchical configuration and the overall mechanical behaviour is determined by the mechanical properties of sub-components and the biological and mechanical interactions developing between them. The ligaments tissue is composed of few cells embedded within an extracellular matrix (ECM). The ECM is a fiber reinforced composite material, composed of collagen fibers embedded in a ground substance matrix. Collagen fibers are closely packed and mainly distributed along one preferential direction that is correlated to the functional behaviour and entails the characteristic anisotropic response. The crimped conformation of collagen fibers and the interaction phenomena between fibers and ground substance determine the non-linearity of the material response. The fluid present in the ground substance is also responsible for the time-dependent and almost incompressible mechanical properties of ligament tissue.

To interpret the over mentioned characteristics, a specific anisotropic fiber reinforced visco-hyperelastic constitutive model is provided.

In order to evaluate the constitutive parameters analytical and numerical models that interpret specific experimental situations are defined. With regard to experimental activities on ankle ligaments, only few papers report experimental data

that provide accurate information about the ligament force-elongation response. Tensile tests performed on bone-ligament-bone specimens are adopted. Model and experimental results are compared by a cost function, whose minimization leads to the optimal set of parameters.

To define a preliminary set of constitutive parameters analytical model is provided and compared with the achieved stress-strain experimental data of each ligament. Stress-strain curves are computed from force-elongation data under the assumption of uniform uni-axial stress conditions. The minimization of the discrepancy between experimental and analytical model results determines the preliminary sets of constitutive parameters. Since it is easy to manage these analytical models, the analysis of these tests offer a quick evaluation of a preliminary set of constitutive parameters. In spite of this, the analytical models that are developed not accounting for the real geometry of the specimen and introducing some hypotheses, such as perfectly uni-axial loading condition, homogeneous stress-strain fields and uniform distribution of collagen fibers. For this purpose the constitutive parameters are upgraded by means of the numerical analyses that interpret the experimental conditions with really greater accuracy.

The numerical models of the bone-ligament-bone specimens are provided by a finite element discretization of virtual solid models, which are developed starting from computed tomography, magnetic resonance imaging and morphometric data. The proposed fiber reinforced visco-hyperelastic formulation is implemented in a general purpose finite element code. Collagen fibers distribution is evaluated by considering the conformation revealed at different points within the ligament by the analysis of histological data. Numerical analyses are provided to interpret the experimental situation, assuming several sets of constitutive parameters, which are evaluated starting from the preliminary set obtained by means of the analytical approach. The numerical analyses allow to evaluate the trend of the discrepancy between numerical and experimental results with different set of constitutive parameters. The minimization of such discrepancy entails the definition of a reliable set of parameters.

The procedure adopted offers the possibility of obtaining a proper evaluation of the biomechanical behaviour of the ligaments of the hindfoot under different loading

condition. The biomechanical response of the hindfoot ligaments during dorsiflexion and plantarflexion movements of the foot are evaluated and compared with experimental data. As matter of example the characteristic phenomenon of inversion of the ankle joint is also reported.

This work is the basis for the evaluation of the influence of each ligament in foot biomechanics. This kind of effort offers the possibility to interpret and analyse the ankle joint trauma that is a social health problem of great interest. Indeed, the ankle damage is one of the most common injuries in athletes. It makes up 25% of all sports-related injuries, 75% of all ankle injuries are sprains and 40% of these sprains will have a chronic symptoms.

CHAPTER 1

MORPHOMETRIC AND BIOMECHANICAL ANALYSIS OF THE FOOT

1.1 Introduction

The foot is one of the most complex parts of the body, consisting of bones connected by numerous joints, muscles, tendons, and ligaments surrounded by soft tissues. All of them interact with each other and allow the foot to carry out its functions. The foot plays an extremely important role in the biomechanical function of the lower extremity and is controlled by both intrinsic and extrinsic muscles. It is the only part of the body that acts on an external surface, providing support and balance during standing and stabilizing the body during gait.

This chapter reports an anatomical description of the foot with particular regard to the hindfoot region. The hindfoot is composed by the ankle and subtalar joint that together transfer forces between the lower leg and foot. These joints are also important in the kinematics of the foot because they allow movements, such as flexion/extension, inversion/eversion and abduction/adduction. To this purpose the contribution of the ligaments is essential to control the excessive movement of the subtalar and ankle joint during human activity. A brief note is also reported with regard to the gait cycle and the ground reaction forces generated during walking. At this purpose experimental gait analysis tests are performed.

1.2 Notes on the anatomy of the foot

The human foot is a complex multi-articular mechanical structure consisting of bones, joints and soft tissues that plays an extremely important role in the biomechanical function of the lower extremity and is controlled by both intrinsic and extrinsic muscles.

As reported in Figure 1.1 the foot can be divided into three main regions: the forefoot (and phalanges), the midfoot and the hindfoot.

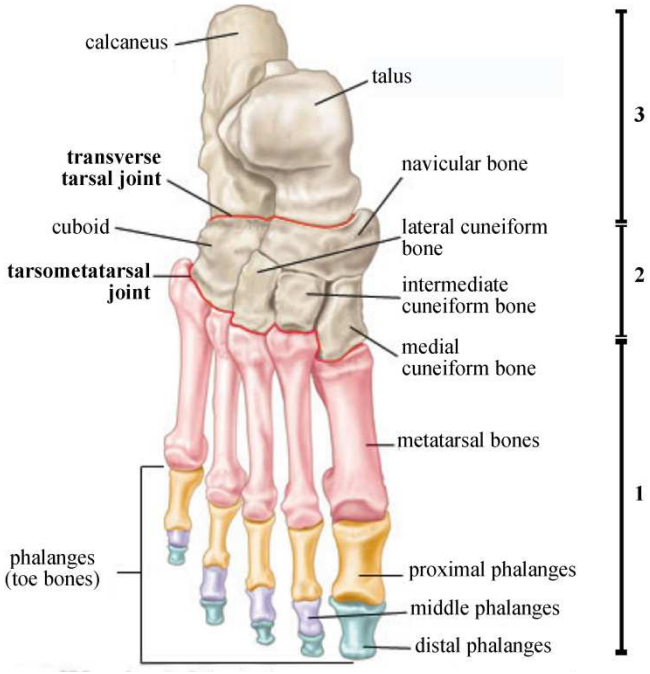

Figure 1.1. Main region of the foot: the forefoot and phalanges (1), the midfoot (2) and the hindfoot (3)

1.2.1 The forefoot and phalanges

The framework of the forefoot is formed by five metatarsal bones and 14 phalanges (the bones of the digits or toes). Each digit has three phalanges (proximal, middle, and distal), except for the big toe, which has only the proximal and distal once. The digits and their metatarsal rays are numbered from one to five, starting with the big toe. The metatarsals and phalanges are long bones. The proximal end or base of each bone has a smooth articular surface where it forms a joint with the adjacent bone. The distal end or head also has an articular surface, except for the distal phalanges, whose distal ends provide attachment for the soft tissue of the digit tips.

Of the metatarsal bones, the first bears the most weight and plays the most important role in propulsion and, therefore, it is the shortest. It provides attachment for several tendons, including the tibialis anterior and the peroneus longus. The fifth metatarsal has a protuberance on the lateral side of its base, to which the peroneus brevis tendon is attached. The second, third, and fourth are the most stable of the metatarsals, in part because of their protected position, but also because they have only minor tendon attachments, and therefore are not subjected to strong pulling forces.

The joints between the metatarsals and the proximal phalanges are called the metatarsophalangeal (MTP) joints. Each digit also has two interphalangeal (IP) joints, proximal (PIP) and distal (DIP), except for the big toe, which has only one IP joint. Each MTP and IP joint is bound together by several ligaments, one on each side of the joint (medial and lateral collateral ligaments), and one along the plantar surface (plantar ligament). The metatarsophalangeal joints are important also because they are the attachment points of the plantar fascia (Figure 1.2). The plantar fascia consists in a thin fibrous band that spans between the medial process of the calcaneal tuberosity, diverging distally to form five bands to continuing up to metatarsophalangeal joints. It is considered to be one of the major stabilizing structures of the longitudinal arch of human foot (Wangdo et al. 1995).

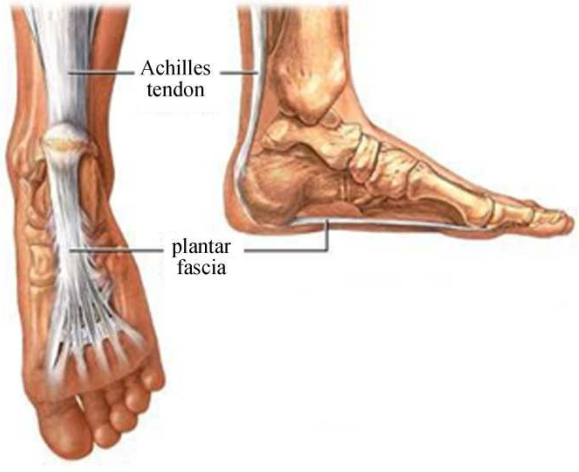

Figure 1.2. Representation of the plantar fascia

The first MTP joint has an additional feature. Near the head of the first metatarsal, on the plantar surface of the foot, there are often two sesamoid bones. A sesamoid is a

small, oval-shaped bone which develops inside a tendon, where the tendon passes over a bony prominence. These sesamoid bones articulate with the head of the first metatarsal, and function as part of the first MTP joint. They are held in place by their tendons, and are also supported by ligaments. These include the sesamoid collateral ligaments (which bind the sesamoids to the metatarsal head) and the intersesamoidal ligament (which connects the sesamoids to each other).

1.2.2 The midfoot

As reported in Figure 1.1 the midfoot is composed of five of the seven tarsal bones, the navicular, cuboid, and three cuneiform bones. These can be thought of as being arranged in two irregular rows, with the cuboid occupying space in both rows. The proximal row contains the navicular on the medial side of the foot and the cuboid on the lateral side. The distal row contains the three cuneiforms (medial, intermediate, and lateral) and the cuboid. The boundary between the midfoot and forefoot consists of five tarsometatarsal (TMT) joints, the joints between the distal row of the midfoot and the bases of the metatarsals. The medial, intermediate, and lateral cuneiforms articulate with the first, second, and third metatarsals, respectively; the cuboid articulates with the fourth and fifth metatarsals. There are also multiple joints within the midfoot itself. The distal row of the midfoot has two intercuneiform joints (between adjacent cuneiforms) and a cuneocuboid joint (between the lateral cuneiform and the cuboid). Proximally, the three cuneiforms articulate with the navicular bone (the cuneonavicular joints). In some individuals, there is also a small articulation between the cuboid and navicular.

In addition to its articular surfaces, each tarsal bone has specific features adapted for each function. For example, the medial surface of the navicular projects downward to form a tuberosity, which serves as an attachment for the tibialis posterior tendon. The lateral surface of the cuboid also has a tuberosity, which serves as a ligament attachment. The cuboid bone has no major tendon attachments; however, the peroneus longus tendon passes across the cuboid tuberosity, to run in a groove on the plantar surface of the bone. The peroneus longus tendon often contains a sesamoid bone, which articulates with a small facet on the tuberosity.

1.2.3 The hindfoot

The articulations of the human hindfoot play an integral role in gait and other movements of the foot. The hindfoot is actually composed of multiple joints that combined, allow for movements such as dorsiflexion, plantarflexion, inversion, and eversion. The talocrural joint (or ankle) is the articulation between the tibia, fibula and the talar dome, and is mainly responsible for plantar/dorsiflexion. Another joint of the hindfoot is the sub-talar joint, which is the articulation between the talus and the calcaneus that provides the inversion and eversion motions. In addition to the bony support, the talocrural and the sub-talar joint also receive substantial support from ligaments and other soft tissue structures.

1.2.3.1 Bones of the hindfoot

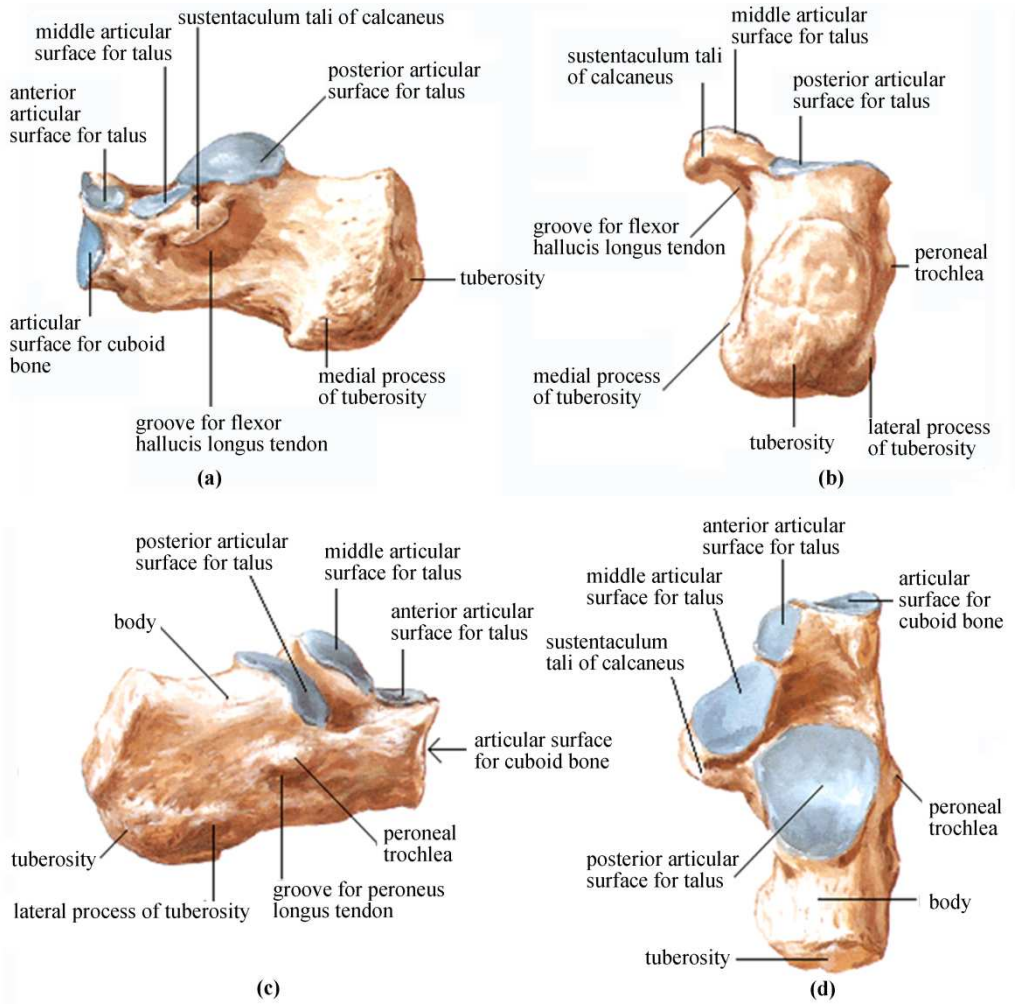

Figure 1.3. Calcaneus: lateral (a), posterior (b), medial (c) and superior (d) view

The calcaneus (Figure 1.3) is located under the talus and has six top faces. Behind the veneer postero-lateral, the upper surface of the bone becomes irregularly cylindrical. The underside is irregular, has a rear tuberosity of the calcaneus that presents two tubercles, medial and lateral. At its front end face it is bound by another tubercle. On the frontal side there is the trochlear process, which is known as the union of the anterior third with the middle third, above and below which there are two grooves for the passage of the peroneal tendons. The medial surface is characterized by the presence of a long shower crossed by tendons, blood vessels and nerves, which start on the leg and finish on the foot. It is bounded in the back of the medial tubercle of the calcaneus, in front of a strong capital know as sustentaculum, because on it rests the medial talus. The base of the sustentaculum is cut by a groove for the passage of the flexor hallucis longus tendon. The anterior articular surface has a vertical concave and convex transversely, so as to comply with the surface articulations of the cuboid. The face is tilted back and corresponds to the projection of the heel. At the bottom it is rough and gives insertion to the calcaneal tendon (Achilles') on the top it is smooth and is separated by a grant from the synovial tendon.

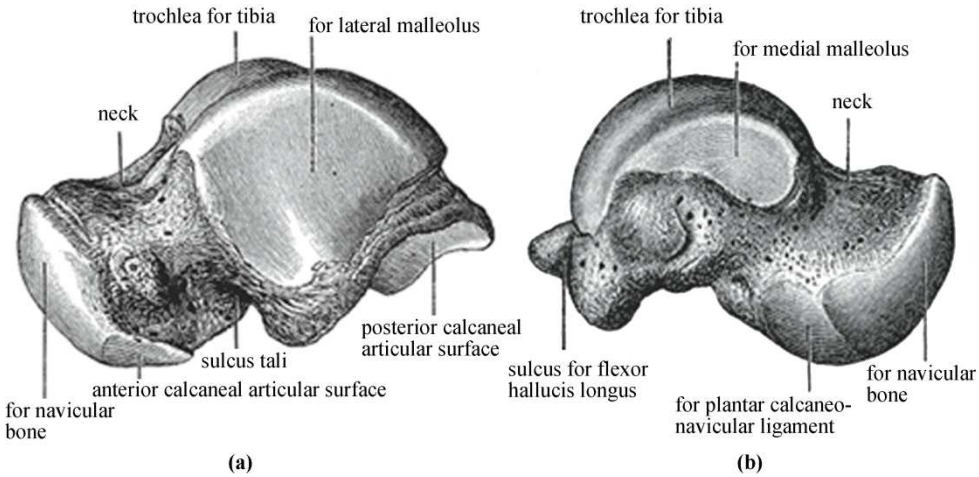

Figure 1.4. Talus: lateral (a) and medial (b) view

The talus (or astragalus), reported in Figure 1.4, is one of the most important bones of the foot. It is possible to distinguish between three parts, namely a rear body, a front head and a collar that is located between the two previous parts. Overall, the

talus is composed of six faces: top, bottom, medial, lateral, front and rear. The upper surface is entirely occupied by a trochlear articular surface cross-shaped with regard to axis of rotation, the pulley has a central groove bounded by two sides recognized in sagittal course. The underside has two flat facets for articulation with the calcaneus. The two facets are divided into the postero-lateral and anterior-medial, and shower are separated by a transverse groove on the talus. In the articulated skeleton, opposite to the groove of the talus, there is an identical semicanal of the calcaneus. This is like a conduit, the tarsal sinus. The anterior-medial articular facet for the calcaneus is, in turn, divided into a front facet and a medial facet. The medial and lateral articular facets are arranged in a sagittal plane to the faces of the tibio-talar joint, which may be regarded as employees of the talar trochlea and both have a shaped crescent with a concave bottom.

The back is occupied from the rear of the pulley, below which there is a sagittal sulcus, for the passage of the flexor hallucis longus tendon. This groove is bordered by two tubercles, lateral and medial, of which the first area is more important. The front face is occupied by the irregularly shaped head, and enters into articulation with the navicular tarsal bone, and continues down to the facet joints below the calcaneus.

The tibia is a long, massive and robust bone, located in the anterior-medial leg region. It is not perfectly straight and has an indentation that is at the top and lower medial side, thus assuming an S-shape, as well as a twist along its longitudinal axis. The tibia can be regarded as a body with two extremities. The body is a triangular prism with three faces and three edges. The medial surface is slightly convex. The lateral surface is concave up, which provides insertion to the anterior tibial muscle. At the bottom, however, it becomes convex. The back is smooth and convex in its whole extent, except in its upper portion where it is crossed by a rough ridge directed downwards and medially to the oblique line (or line of the soleus muscle). The front edge is chamfered at the ends, as it tends to become sharper in the center of the bone, following the winding of the shaft and the bottom fold and medially terminating at the medial malleolus. The medial margin is not very pronounced. The lateral margin (or interosseous) is sharp and offers attachment to the interosseous membrane of the leg. The upper end is quite developed, especially in the transverse direction and expands in two masses, the tibial condyles. The top face of each of these has a

shallow glenoid cavity for articulation with the femoral condyles. Between the two cavities there is the intercondylar eminence, formed by two tubercles, the medial and the lateral tubercles intercondylar, respectively. The condyles converge on a relief, the tibial tuberosity; however, in the posterior region they are separated by a groove. The lower end, which is less developed than the upper surface, is concave antero-posterior and is divided into two sides by a sagittal crest corresponding to the trochlea of the talus. Medially to the lower end, it expands to the medial malleolus. The medial malleolus is the seed coat and is furrowed by the passage of the tendons of the flexor muscles, and has a lateral facet, which is opposed to the medial talar articular surface. On the lateral side of the distal tibia there is also a small articular surface for the fibula.

The fibula is a long bone, thinner than the tibia. It is formed by a body and two extremities. The body is straight and has a triangular prismatic form. In the frontal side it is smooth, except at the center of the bone where there is a depression to accommodate the lateral peroneal muscles. The medial surface is covered by a vertical relief, where the interosseous membrane is inserted. The back is rough for a variety of muscle insertions. The three margins are thin and sharp. The upper end has a flat articular facet, once up and medially, joining with the articular facet of tibia. On the lateral side, the fibula raises a pyramidal projection, the styloid process of fibula, where the insertion of the biceps femoris takes place. The bottom has bulges in the lateral malleolus. The surface of the medial malleolus is divided up with the approved tibial facet, down with the articular surface of the talus. Behind this veneer there is always a very clear depression where the posterior talo-fibular ligament is. Under the lateral malleolus there is a sagittal sulcus for the passage of tendons of the peroneal muscles.

1.2.3.2 Ligaments of the hindfoot

The ligaments of the hindfoot are very important because they stabilize and support the ankle and the sub-talar joints that have a fundamental role during the motion of the foot. These ligaments are responsible for ankle sprains that are the most common type of acute sport trauma (Fong et al. 2009).

The ligaments around the ankle complex joint can be divided, depending on their anatomic position, into four groups: the lateral ligaments, the medial (or deltoid) ligament, the ligaments of the tibiofibular syndesmosis and the ligaments of the subtalar articulation.

1.2.3.2.1 Lateral collateral ligaments

The lateral collateral ligament complex (Figure 1.5) consists of the anterior talofibular (ATFL) ligament, the calcaneofibular (CFL), and the posterior talofibular ligaments (PTFL).

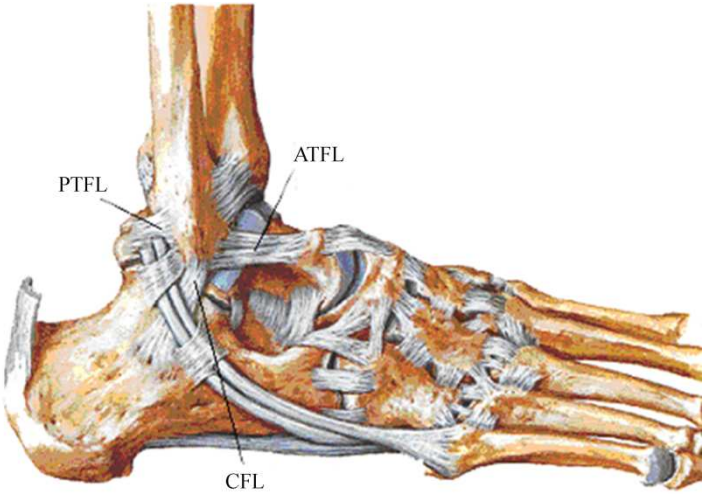

Figure 1.5. Lateral collateral ligaments of the ankle

The anterior talofibular ligament is the most frequently injured ligament of the ankle (Van Den Bekeron et al. 2008; Taser et al. 2006; Kumai et al. 2002). This ligament is closely related to the ankle joint capsule and is typically composed of two separate bands. In literature, numerous anatomic descriptions have been given, varying from a single up to three bands (Taser et al. 2006; Milner and Soames 1997; Burks et al. 1994). The anterior talofibular ligament is a flat, quadrilateral ligament that originates at the anterior margin of the lateral malleolus. The center is on average 10 mm proximal to the tip of the fibula as measured along the axis of the fibula itself. The overall width of this ligament does not appear to vary greatly irrespective of the number of bands present, suggesting that the variations observed do not modify the ligament's function. From its origin, it runs anteromedially to the

insertion on the talar body immediately anterior to the joint surface occupied by the lateral malleolus. The ligament is virtually horizontal to the ankle in the neutral position but inclines upward in dorsiflexion and downward in plantar flexion. It is only in the latter position that the ligament comes under strain and is vulnerable to injury, in particular when the foot is inverted. In the plantar flexion, the inferior band of the ligament remains relaxed while the upper band becomes taut. In dorsiflexion, the upper band remains relaxed, and the inferior band becomes tight. From a morphometric point of view the anterior talofibular ligament is approximately 6-10 mm in width, 15-20 mm in length and 2 mm in thickness (Van Den Bekerom et al. 2008). The average area of attachment is 8.2 mm in the sagittal dimension and 5.4 mm in the coronal dimension. The anterior talofibular is directed at an average of 44.8° medially from the fibula toward the talus in the coronal plane. It makes a mean angle of 25° with horizontal plane and a mean angle of 47° with the sagittal plane.

The calcaneofibular ligament originates from the anterior part of the lateral malleolus. It is anatomically positioned just below the lower band of the anterior talofibular ligament. In the neutral ankle position, the ligament runs obliquely downwards and backwards to attach to the posterior region of the lateral calcaneal surface. This ligament is superficially crossed by the peroneal tendons which can leave a concavity over the ligament. In cross section the ligament is rounded and has a diameter of 6-8 mm, and is about 20 mm in length. The calcaneofibular ligament is the only ligament bridging both the talocrural joint and subtalar joint. The insertion of this ligament and its axis of rotation allow flexion and extension movements of the talocrural joint. Depending on its bi-articular characteristic, this ligament also permits subtalar movement. Variants in the orientation of the calcaneofibular ligaments were studied by Ruth (1961). The calcaneofibular ligament becomes horizontal during extension and vertical in flexion, remaining tense throughout its entire arc of motion. In cross section the ligament is a strong cord-like or flat oval ligament and measures approximately 4-8 mm in diameter, about 20 mm in length and 4-5.5 mm in width. With the foot in the plantigrade position, the calcaneofibular ligament forms an angle of 47° with the fibula. Ruth defined a mean angle of 40° (22°-58°) with the horizontal plane, and a mean angle of 51° (32° - 60°) with the

sagittal plane. The angle between the calcaneofibular and the anterior talofibular ligament is approximately 132 °.

The posterior talofibular ligament originates from the malleolar fossa, located on the medial surface of the lateral malleolus, running almost horizontally to insert in the posterolateral talus. Due to its multifascicular aspect, it inserts not just in a specific area. Fibers insert in the posterior surface of the talus, in the lateral talar process. The posterior attachment on the talus measures 24.1 mm by 6 mm. Some fibers can contribute towards forming the tunnel for the flexor hallucis longus tendon. In plantar flexion and in the neutral ankle position, the ligament is relaxed, while in dorsiflexion, the ligament is tensed. A group of fibers of the posterior talofibular ligament is fused with the posterior intermalleolar ligament. Because of its limited size and therefore difficult assessment during an ankle dissection, this ligament can be absent. Moreover in the posterior view, the posterior intermalleolar ligament is situated between the transverse ligament and the posterior talofibular ligament and runs obliquely from lateral to medial and from downwards and upwards. The shape of the posterior intermalleolar ligaments is variable. These variations depend on its medial arising sites, the number of composing fiber bundles and the degree of bundle compactness. The posterior intermalleolar ligament tenses during dorsiflexion and relaxes during plantar flexion. This ligament is trapezoidal in contour and measures about 30 mm in posterior length, 5 mm in width at the fibular origin, and 5-8 mm in thickness.

1.2.3.2.2 Deltoid ligament

The anatomical description of the medial collateral ligament (Figure 1.6) varies widely in the literature; however most agree that it is composed of two layers: the superficial and deep (Morvan et al. 2001). It is a multifascicular ligament, originating from the medial malleolus to insert in the talus, calcaneus and navicular bone. Nonetheless, most descriptions proposed in the literature of the anatomy of this ligament and its components are still confusing.

Posterior tibiotalar ligament (PTTL): the PTTL ligament originates from

the medial malleolus. The fibers of the ligament insert on the posterior process of the talus.

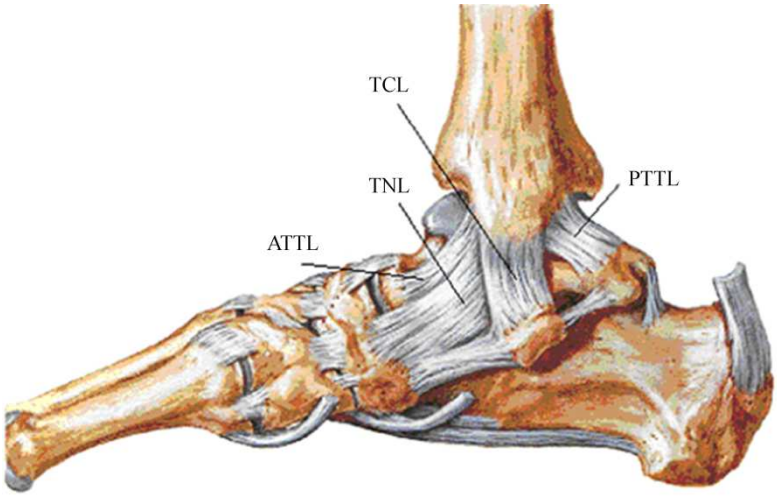

Figure 1. 6. Deltoid ligament of the ankle

Tibiocalcaneal ligament (TCL): the TCL ligament originates from the medial malleolus. The fibers of the ligament insert on the sustentaculum tali of the calcaneus.

Tibionavicular ligament (TNL): the TNL ligament originates from the medial malleolus. The fibers of the ligament insert on the navicular bone

Anteriot tibiotalar ligament (ATTL): the ATTL ligament originates from the medial malleolus. The fibers of the ligament insert on the neck of the talus

1.2.3.2.3 Ligaments that join the distal epiphyses of the tibia and fibula

The ligaments that join the distal epipheses of the tibia and fibula are the anterior (ATiFL) and posterior tibiofibular (PTiFL) ligament and the interosseous ligament.

The anterior (or anterior inferior) tibiofibular ligament originates in the anterior tubercle of the tibia: it is on average 5mm above the articular surface (Van Den Bekeron et al. 2007), and its fibers extend in a distal and lateral direction to the insertion site in the anterior margin of the lateral malleolus, with increased length of the fibers distally. Most of the distal fascicle of the anterior tibiofibular ligaments

appears to be independent from the rest of the structure. The anterior tibiofibular ligament is highlighted in Figure 1.7.

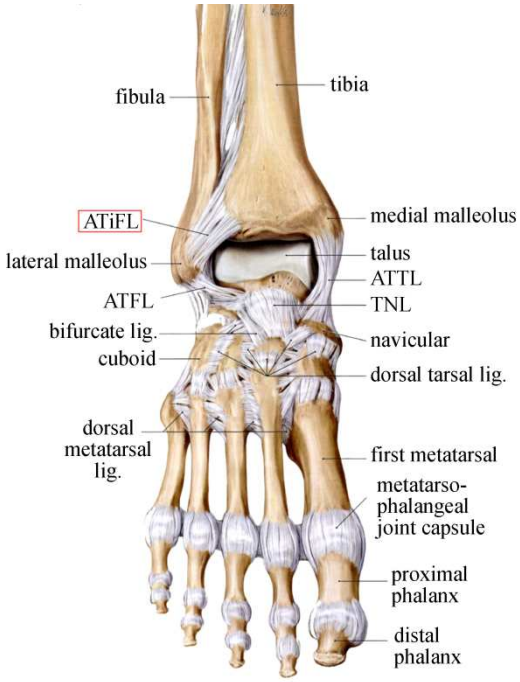

Figure 1. 7. Anterior tibiofibular ligament (ATiFL)

The posterior (or posterior inferior) tibiofibular ligament (Figure 1.8) is basically formed by two independent components, the superficial and deep component. The superficial component originates at the posterior edge of the lateral malleolus and directs proximally and medially to insert in the posterior tibial tubercle. This component would be homologous to the anterior tibiofibular ligament. The term posterior or posteroinferior tibiofibular ligament is normally used to refer to the superficial component.

The deep component (or the transverse ligament) is cone shaped and originates in the proximal area of the malleolar fossa to insert in the posterior edge of the tibia. Its insertion is immediately posterior to the cartilaginous covering of the inferior tibial articular surface; the fibers may reach the medial malleolus. This component provides the stability of the talocrural joint and prevents posterior talar translation.

A detail of the posterior tbiofibular ligament (PTiFL) is reported in Figure 1.8.

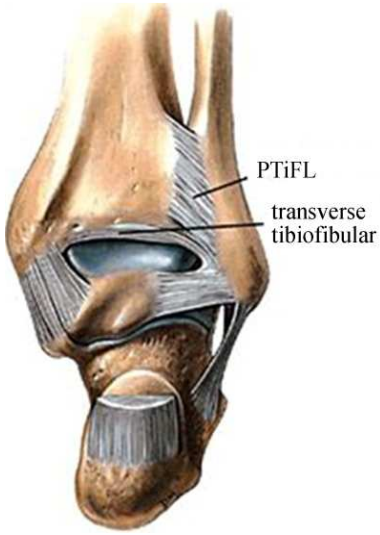

Figure 1. 8. Posterior tibiofibular ligament (PTiFL)

The interosseous tibiofibular ligament is a dense mass of short fibers, which, together with adipose tissues and small branching vessels from the peroneal artery, span the tibia and the fibula. Some investigators have suggested that this ligament is mechanically insignificant, whereas others (Hoefnagels et al. 2007) suggest that the interosseous ligament plays an important role in the stability of the ankle.

1.2.3.2.4 Interosseous talocalcaneal ligament

The interosseous talocalcaneal ligament (ITCL) is a portion of the united capsules of the talocalcaneonavicular and the talocalcaneal joints, and consists of two partially united layers of fibers, one belonging to the former and the other to the latter joint. It is attached, above, to the groove between the articular facets of the under surface of the talus, and below, to a corresponding depression on the upper surface of the calcaneus. It serves to bind the calcaneus and talus firmly together. Moreover, the cervical ligament plays a significant role in the lateral stability of the subtalar joint (Martin et al. 1998).

1.2.3.3 Tendons and muscles of the hindfoot

In order to provide a complete description of the hindfoot, some notes about the tendons and muscles of the hindfoot are reported. The tendons and muscles of the

hindfoot can be subdivided on the basis of their location. In particular, there are five groups: the lateral, medial, anterior and posterior tendons. The lateral group consists primarily of the peroneal tendons (fibularis brevis and longus). These muscles provide active eversion and assist with plantar flexion of the ankle. The muscles originate from broad attachments to the fibula. As shown in Figure 1.9 the tendons of this muscle wrap under the lateral malleolus. The peroneus brevis inserts into the base of the fifth metatarsal, and inversion injuries commonly cause avulsion fractures of this structure. The peroneus longus curves under the midfoot and attaches to the base of the first metatarsal on the plantar aspect of the foot.

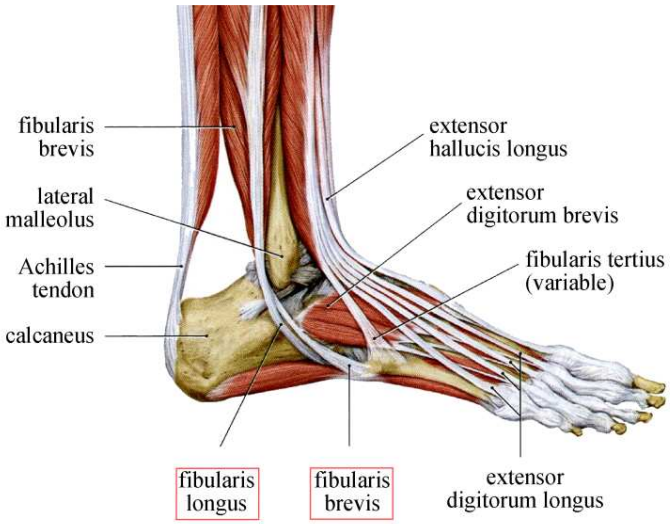

Figure 1.9. The peroneal tendons

The medial group of muscles includes the posterior tibialis, the flexor digitorum longus and the flexor hallucis longus (Figure 1.10). The posterior tibialis muscle is the largest of the three medial tendons and has an oval shape. The main function of the posterior tibialis is to invert the midfoot and lock the transverse tarsal joint. In detail this tendon is the most powerful invertor of the foot. It participates in maintaining the medial longitudinal arch and is one of the main stabilizers of the hindfoot against valgus deformity. Dysfunction in this structure can lead to flat-foot deformity. The tendon wraps just around the medial malleolus and inserts onto the plantar surface of the metatarsals, cuneiforms and navicular. The flexors muscles and tendons are important because flexes toes and helps in plantar flexion of the ankle.

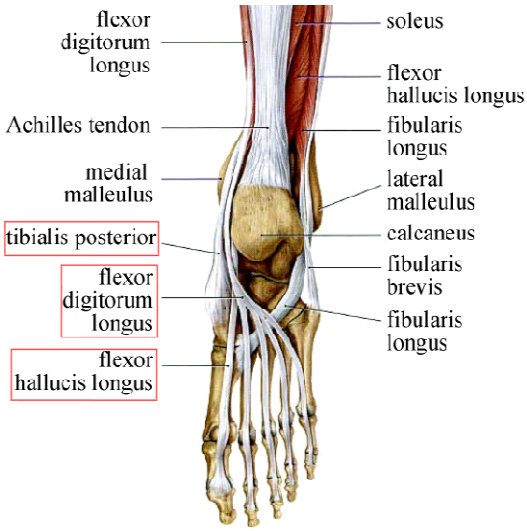

Figure 1.10. The medial group of tendons

The anterior muscles are the anterior tibialis, the extensor digitorum longus and the extensor hallucis longus (Figure 1.11). The anterior tibialis originates broadly along the medial tibia, and then the tendon courses medially, inserting into the plantar surface of the first metatarsal and navicular. Its function is the dorsiflexion of the ankle. The extensor digitorum longus and the extensor hallucis longus takes its attachment from the fibula. The first inserts into the phalanges, providing extension of the toes while the extensor hallucis longus inserts into the phalanges of the first ray and provides the extension of the big toe.

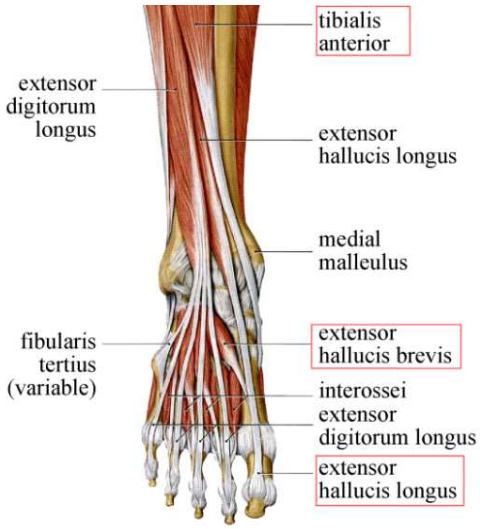

Figure 1.11. The anterior group of tendons

The posterior muscles (Figure 1.12) are the two heads of the gastrocnemius and the soleus, which coalesce to form the Achilles tendon that is the primary plantar flexor of the foot at the ankle joint. The tendon arises from the medial and the lateral heads of the gastrocnemius muscle and the soleus muscle. The medial and lateral heads of the gastrocnemius muscle stem from the posterior femur just above the femoral condyles. The soleus muscle stems from the fibular head, the upper fibula and the interosseous membrane. The musculo-tendinous junction is variable, and the inferior tip of the muscle is often only 5–10 cm above the calcaneal insertion. The tendon has a relatively hypovascular region approximately 4–6 cm above its insertion, where most Achilles tendon injuries occur. The anterior margin may have a focal convexity, representing the separate gastrocnemius and soleus tendons as the tendons intertwine and rotate as they descend to the calcaneal insertion. The posterior margin of the Achilles tendon has a convex contour. The normal tendon measures approximately 7 mm in the anteroposterior dimension, and the anterior and posterior margins are parallel on true sagittal images through the tendon. The Achilles tendon does not have a tendon sheath. There is a paratenon present on the dorsal, medial and lateral aspects that aids in the smooth gliding of the tendon.

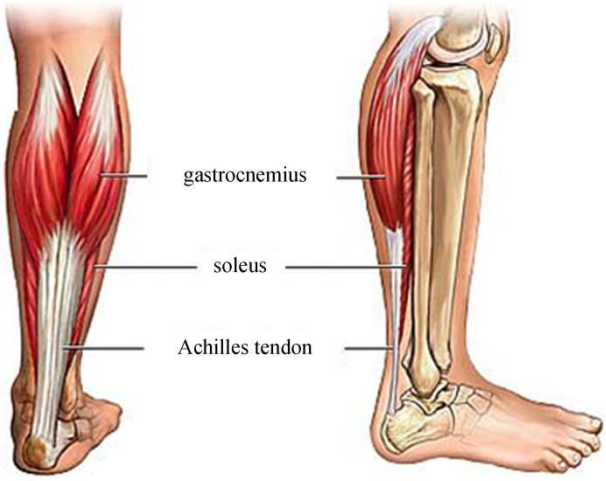

Figure 1.12. The Achille's tendon

1.3 The load on the foot during standing

The foot plays an extremely important role in the biomechanical function of the lower extremity, providing support and balance during standing and stabilizing the

body during gait. For this purpose notes about the load acting on the foot during standing and walking are reported.

In quiet standing the ground reaction force is vertical and constant, being equal and opposite to the body weight. The load on the foot is transmitted by the tibiotalar articulation, but many authors have demonstrated that the fibula carries a part of the body weight (Wang et al. 1996; Takebe 1984; Lambert 1971).

	Lambert	Wang	Takebe
Applied load	68	60	60
Normal position	17%	11%	6.4%
Plantarflexion	/	/	2.3 (15°)
Dorsiflexion	/	23% (15°)	10.4 (15°)
Inversion	/	5% (10°)	2.4 (/)
Eversion	/	17% (10°)	10.4 % (/)

Table 1.1: Weight-bearing of the fibula as a percentage of the total load

The body weight transmitted to the foot through the ankle joint is distributed over three very specific points of the foot (Figure 1.13). In detail, if 6 Kg are applied on the foot, a sixth of the force acts on the fifth metatarsal head, a third on the first metatarsal head and half of the weight force acts on the calcaneus (Kapandji I.A., 1970).

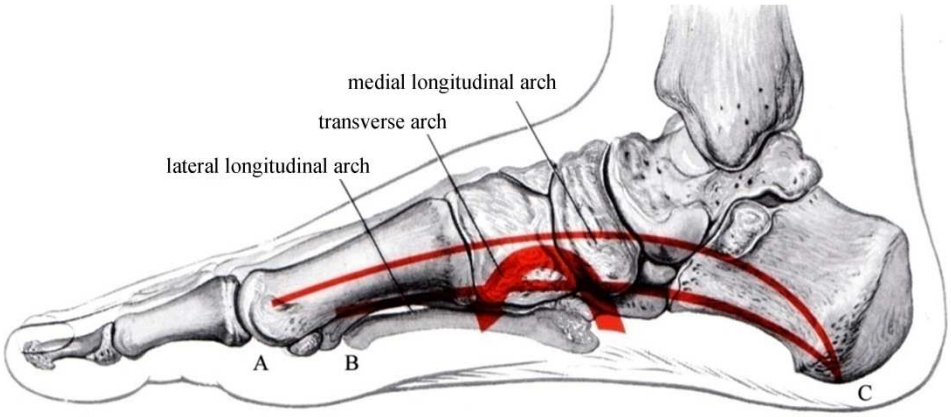

Figure 1.13. Distribution of the body weight on the foot: A) first metatarsal head, B) fifth metatarsal head and C) calcaneus

1.4 The movements of the foot and ankle

To understand the load on the foot during walking it is necessary to describe the movement that the foot can undergo during the gait cycle.

The movement of the body is defined by reference to a plane (Figure 1.14). The sagittal plane is a vertical plane which passes from front to rear dividing the body into right and left sections, and the terms medial and lateral is related to this plane. The frontal or coronal plane passes from side to side at right angles to the sagittal plane which divides the body into an anterior and posterior section. The transverse plane is parallel to the flat surface of the ground. Planes in this direction divide the body into an upper and lower part. The same configuration is used to describe the movement of the foot.

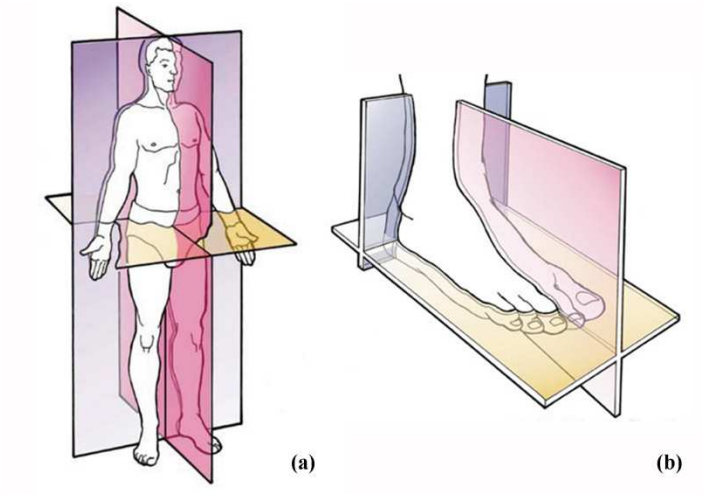

Figure 1.14. Sagittal, frontal and transverse plane of the body (a) and of the foot (b)

Looking closely, a discussion of mechanics of the motion of the ankle joint complex (i.e. talocrural and sub-talar joint) requires consistent terminology. The major motions about an anatomical joint coordinate system are rotations: plantarflexion/dorsiflexion, inversion/eversion, and internal/external rotation (or abduction/adduction).

To define the movements of the ankle complex joint it is useful to define the coordinate system of the joint. The most widely adopted in the literature is represented in Figure 1.15 (Siegler et al. 2005). The points A1, A2, A3 illustated in the figure are the lateral malleolus, medial malleolus, and the centroid of the tibial

cross-section respectively. These three points define an anatomical frame for the tibia as follows: the line A2A1 is the X-axis of the tibia. The perpendicular to the plane containing A1, A2, A3 is the Z-axis of the tibia, and the common perpendicular is the Y-axis. The origin is located at the mid-point between A1 and A2.

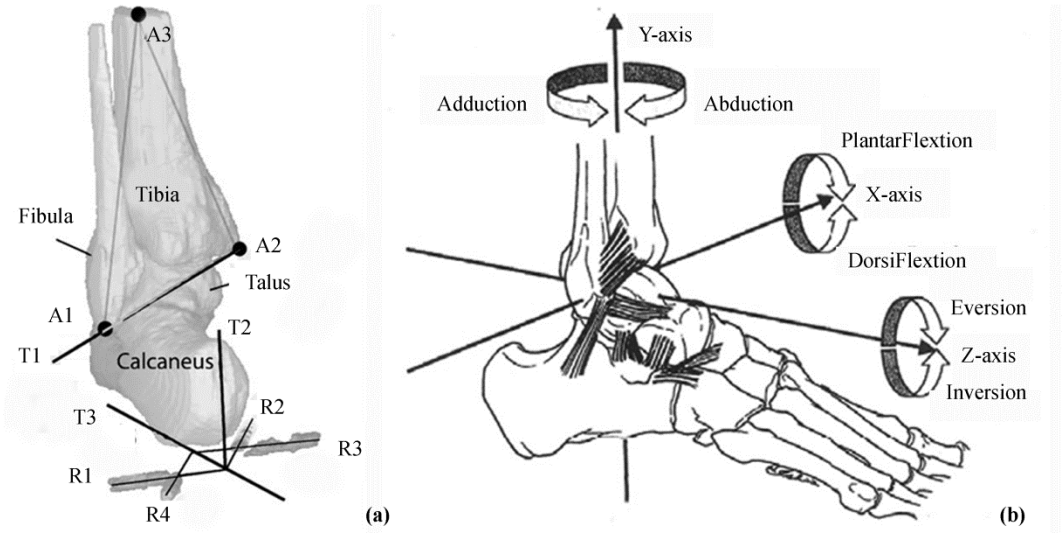

Figure 1.15. Definition of the axis of the join ankle complex(a) and the movements of the foot (b)

Flexion and extension are movements in the sagittal plane. Flexion movements bend the body part away from the anatomical position. Extension is the movement in the opposite direction back to the anatomical position and beyond into a reversed position. In the case of the foot the flexion and extension movements are called plantarflexion and dorsiflexion respectively and represent the rotations around the X-axis (Figure 1.15b).

Plantarflexion and dorsiflexion are the major components of the motion at the ankle joint during gait. The range of motion of the ankle joint varies across the literature but generally is reported to be around 70 degrees of full motion, although this number is dependent on loading conditions and measurement technique. The typical breakdown of total talocrural motion is usually around 30-40 degrees of plantarflexion, and about 20-30 degrees of dorsiflexion. Many authors cite variable ranges of motion for the ankle joint in the plantarflexion/dorsiflexion rotations (Table 1.2).

Range of motion (deg)		Authors
Plantaflexion	Dorsiflexion	
30 -50	20 -30	Kapandji (1970)
25-35	10 - 20	Nordin and Frankel (1989)
37.6 - 45.8	20.3 – 29.8	Siegler et al. (1988)
20 - 50	13 - 33	Allinger and Engsberg,(1993)

Table 1.2. Range of motion with regard to plantarflexion and dorsiflexion movements

The inversion and eversion movement of the foot are movements that raise the medial and the lateral border of the foot, respectively. This kind of motion is developed with rotations along the long axis of the foot, Z-axis (Figure 1.15b). Motion in this direction is thought to be primarily contributed by the subtalar joint.
The movement of inversion is produced by any muscle that is attached to the medial side of the foot. The tibialis anterior and tibialis posterior are responsible, assisted by the extensor and flexor hallucis longus on both occasions. The tibialis anterior dorsiflexes and the tibialis posterior plantarflexes the foot at the ankle joint and these opposite effects cancel each other out when the two muscles combine to produce an inversion of the foot. The movement of eversion is produced by muscles that are attached to the lateral side of the foot. The peroneus longus, brevis and tertius are responsible for this. The former two, whose tendons pass behind the lateral malleolus, are plantarflexors, the latter is a dorsiflexor of the ankle joint. These opposite effects cancel each other out when the three muscles combine to produce a simple eversion of the foot. In the literature there are many works that reported the range of motion of the inversion and eversion movement (Table 1.3).

Range of motion (deg)		Authors
Inversion	Eversion	
20	5	Kapandji (1970)
14.5 – 22	10 - 17	Siegler et al. (1988)
12.5 ± 5.8, in vivo 12.6 ± 5.8, in vitro	N/A	Siegler et al. (2005)
15 – 20	10 – 17	Cass et al. (1984)
30	20	Sarrafian (1993)

Table 1.3. Range of motion with regard to inversion and eversion movements

The abduction and adduction are movements in the frontal plane. Adduction movement carries a body part away from the midline. Abduction is movement in the

opposite direction towards the midline. Rotations about the long axis of the tibia, the Y-axis (Figure 1.15b), are internal and external rotation or adduction and abduction respectively.

These types of rotations usually do not occur by themselves but in combination with plantarflexion, dorsiflexion, inversion and eversion.

The range of motion of the abduction and adduction movement of the foot are reported in the following table.

Range of motion (deg)		Authors
Abduction	Adduction	
22-36	15.4 – 25.9	Siegler et al. (1988)
N/A	24	Kjaersgaard-Andersen al. (1991)

Table 1.4. Range of motion with regard to abduction and adduction movements

Supination and pronation are a combination of the above motions. It is common to use both supination and inversion, and pronation and eversion interchangeably. But, supination is actually a combination of inversion, plantarflexion and adduction. Pronation is a combination of eversion, dorsiflexion and abduction. Supination is a triplanar motion involving the foot moving down and towards the center of the body, while pronation is a triplanar motion of the subtalar joint involving the foot moving up and away from the center of the body.

1.5 The phase of the gait cycle

The gait cycle is defined as the time between the first contact with the ground by the heel of one foot and the next heel-to-ground contact with the same foot.

One single limb cycle is usually composed of two phases: stance and swing. The stance phase begins when the foot first contacts the ground while the swing phase begins as the foot leaves the ground. On average, the gait cycle is about one second in duration with 60 percent in stance and 40 percent in swing.

A schematic representation of the gait cycle is reported in Figure 1.16.

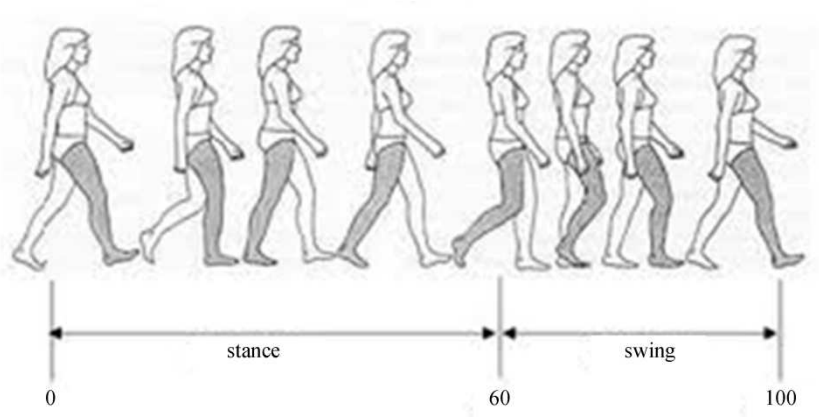

Figure 1.16. The two phases of the gait cycle: stance and swing

The stance and the swing phases of the gait can be divided into different sub-phases. With regard to the stance phase, there are five sub-phases (Figure 1.17): initial contact (heel-contact), loading response (or foot-flat), mid stance, terminal stance and pre-swing (or toe-off).

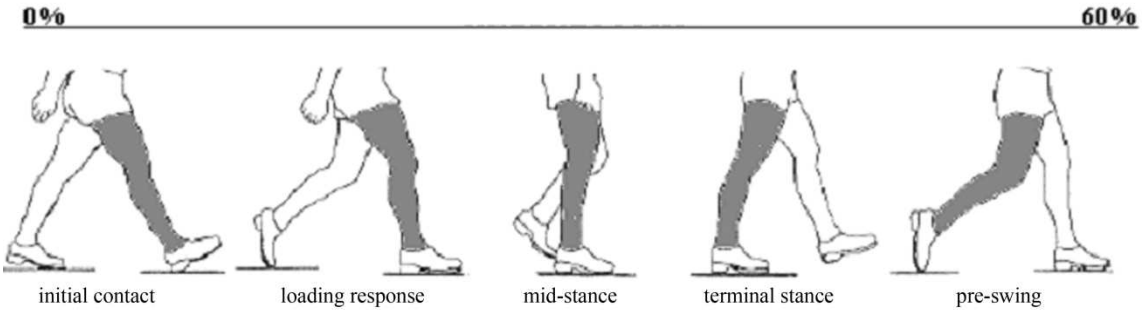

Figure 1.17. The stance phase of the gait cycle

The first phase is the heel contact phase, which is when heel hits the ground. This phase continues until the foot is flat on the ground. This constitutes 20 percent of the total gait cycle. The next phase is the midstance phase. In this part of the gait cycle, which represents 30 percent of the cycle, your body weight passes over your foot as the body comes forward. This is when your foot supports your body weight. This is the part of the gait cycle where an abnormally functioning foot, such as an over pronated foot (flat foot) or an over supinated foot (high arch foot), will manifest its problems. This phase ends as your body weight passes forward, eventually forcing your heel to rise during the terminal stance. During the last phase the foot pushes off

the ground to propel the body forward and to prepare the body for the swing phase of the gait. Most forefoot pain occurs in this phase of the cycle.

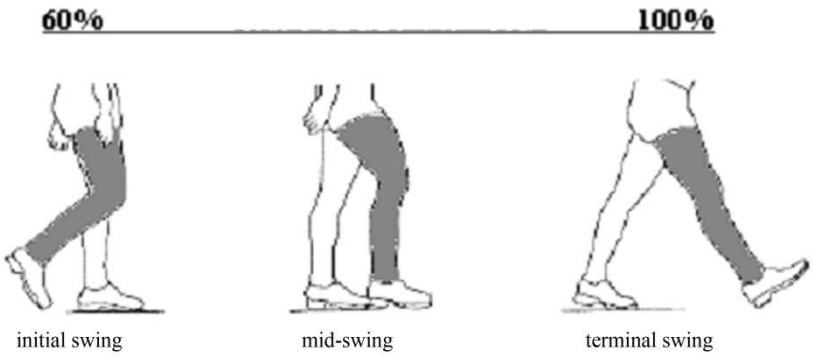

Figure 1.18. The swing phase of the gait cycle

As shown in Figure 1.18 the swing phase of the gait can be divided into three sub-phases: initial swing, mid-swing and terminal swing. The initial swing begins at toe off and continues until maximum knee flexion (60 degrees) occurs, while the mid-swing phase is the period from maximum knee flexion until the tibia is vertical or perpendicular to the ground. The swing phase ends with the terminal swing that begins when the tibia is vertical and ends at the point of initial contact of the other foot.

1.6 Experimental evaluation of the ground reaction force in the gait cycle

Forces transmitted across the ankle joint during the gait cycle are a combination of external and internal forces. The internal forces are produced by muscles and ligaments. These internal forces are not completely understood because the in vivo determination of these forces is very difficult. On the other hand, in literature there are several works on the determination of the internal forces throughout computational methods (Yu et al. 2010; Heintz and Gutierrez-Farewik 2007). The external forces transmitted across the ankle are the forces produced when contacting the ground. These ground reaction forces (GRF) can be measured experimentally during gait using force platforms. To evaluate the ground reaction force and the behaviour of the ankle during the gait cycle, experimental tests are performed in collaboration with the staff of Ospedale San Bassiano, Bassano del Grappa, Italy.

The three dimensional kinematics data are calculated throughout a Vicon MX (Oxford, UK) system with six high-resolution cameras and two AMTI (Advanced Mechanical Technology Inc, Watertown, MA, USA) force-plates (Figure 1.20); each of them is 400 mm in width, 600 mm in length and 82.5 mm in height. The AMTI force platforms are located halfway along a 15-m walkway.

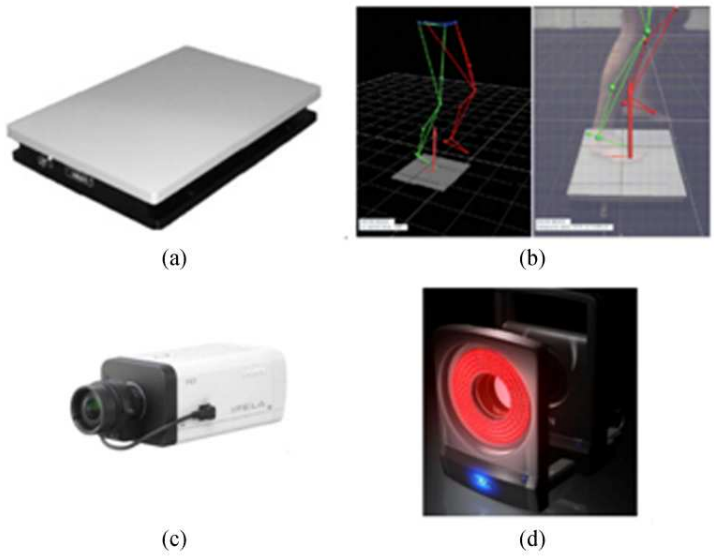

Figure 1.20. Experimental setup: (a) AMTI platform, (b) Software Vicon Nexus, (c) video camera and (d) high resolution infrared cameras

Lightweight retro reflective markers are attached to the skin of the subject over the bony landmarks. To capture the trajectories of those markers the subject walks along a walkway at normal speed in a barefoot condition. Simultaneously, the three components of the ground reaction forces are measured in correspondence to the fifth and the sixth step by two force platforms AMTI BP400600 positioned under a cover floor. During the tests five subjects are considered (Table 1.5).

Gender	Height (cm)	Mass (kg)	Age
M	173	66	71
M	177	72	75
M	180	73	74
F	163	59	60
F	150	53	69

Table 1.5. Description of the subjects

For each subject seven acceptable trials are collected and averaged for further analysis. The three components of the ground reaction force are evaluated by means of the AMTI force platforms. The vertical force (Figure 1.21), with normal gait speed, presents two peaks separated by a valley. The value of the peaks is usually equal to 100-120% of body weight, while the value of the valley of the normal force corresponds to 80% of body weight.

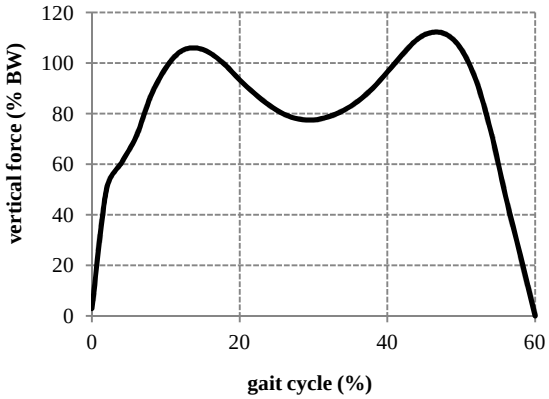

Figure 1.21. Experimental results: the vertical component of the ground reaction force

The amplitude of the horizontal components of the reaction force in comparison to the vertical load is minor.

In the normal subject the anterior-posterior shear force (Figure 1.22) is less than 25% of body weight. During the initial contact phase a momentary shear force equal to 13% of the body weight often occurs. At the mid-stance the anterior-posterior force is minimal until the moment before raising the calcaneus. After this, the force increases in the rear direction and during the terminal stance reaches a new peak.

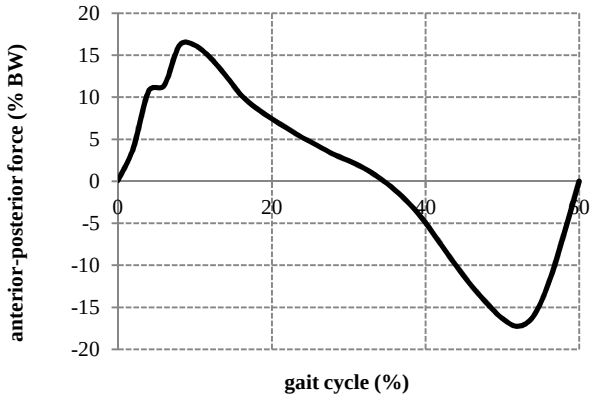

Figure 1.22. Experimental results: the anterior-posterior component of the ground reaction force

As shown in Figure 1.23 the magnitude of the medial-lateral force is smaller and is less than 10% of body weight. The peak of the medial shear force occurs in the loading response phase, while the lateral shear force reaches a peak in the terminal stance.

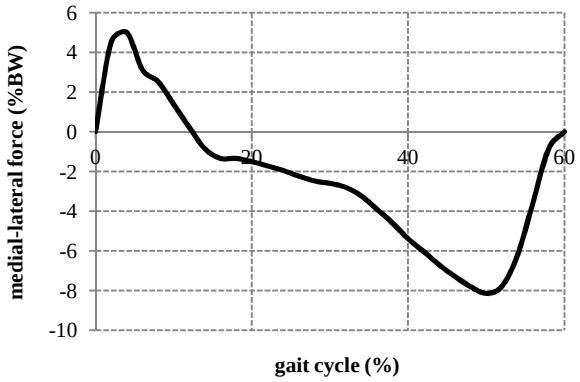

Figure 1.23. Experimental results: the medial-lateral component of the ground reaction force

The values reported are in agreement with the range reported in the literature (Kirtley 2006).

At the same time the optoelectronic system allows the evaluation of the kinematic of the foot. With particular regard to the ankle joint, the plantar/dorsiflexion angle during the gait cycle is reported in Figure 1.24.

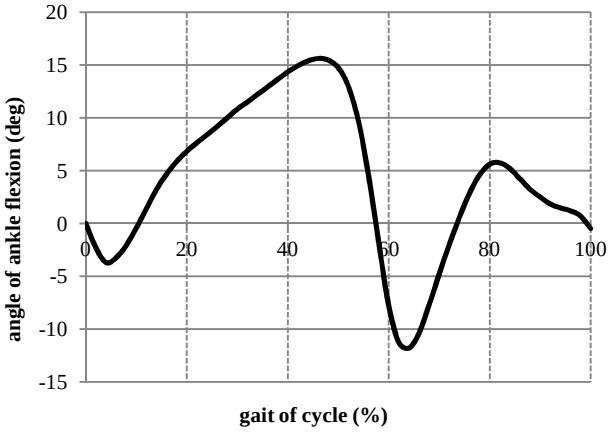

Figure 1.24. Experimental results: the dorsiflexion (positive values) and the plantarflexion (negative values) of the ankle during gait

1.7 References

Allinger T.L. and J.R. Engsberg, 1993. A method to determine the range of motion of the ankle joint complex, in vivo. Journal of Biomechanics, vol. 26(1), pp. 69-76.

Burks R.T., Morgan J., 1994. Anatomy of the lateral ankle ligaments, The American Journal of Sports Medicine, vol. 22, pp. 72-73.

Cass J.R., B.F. Morrey, and E.Y. Chao, 1984. Three-dimensional kinematics of ankle instability following serial sectioning of lateral collateral ligaments. Foot & Ankle, vol. 5(3), pp. 142-9.

Fong D.T.P., Chan Y.Y., Mok K.M., Yung P.S.H., Chan K.M., 2009. Understanding acute ankle ligamentous sprain injury in sports, Sports Medicine, Arthroscopy, Rehabilitation Therapy & Technology, vol. 1(1), pp. 14, doi: 10.1186/1758-2555-1-14.

Heintz S., Gutierrez-Farewik E.M., 2007. Static optimization of muscle forces during gait in comparison to EMG-to-Force processing approach, Gait & Posture, vol. 26, pp. 279-288.

Hoefnagels E.M., Waites M.D., Wing I.D., 2007. Biomechanical comparison of the interosseous tibiofibular ligament and the anterior tibiofibular ligament, Foot & Ankle International, vol. 28, pp. 602-604.

Kapandji I.A., 1970. The physiology of the joints: annotated diagrams of the mechanics of the human joints. 2nd ed., London,: E. & S. Livingstone.

Kirtley C., 2006. Clinical gait analysis. Elsevier, Churchill Livingstone.

Kjaersgaard-Andersen P., Frich L.H., Madsen F., Helmig P., Sogard P., Sojbjerg J.O., 1991. Instability of the hindfoot after lesion of the lateral ankle ligaments: investigations of the anterior drawer and adduction maneuvers in autopsy specimens, Clinical Orthopedics and Related Research, vol. 266, pp. 170-179.

Kumai T., Takakura Y., Rufai A., Milz S., Benjamin M., 2002. The functional anatomy of the human anterior talofibular ligament in relation to ankle sprains, Journal of Anatomy, vol. 200, pp. 457-465.

Lambert K.L, 1971. The weight bearing function of the fibula. Journal of bone joint surgery, vol.53-A, pp. 507-513.

Martin L.P., Wayne J.S., Monshan T.J., Adelaar R.S., 1998. Elongation behaviour of calcaneofibular and cervical ligaments during inversion loads applied in an open kinetic chain. Foot & Ankle International, vol. 19(4), pp. 232-239.

Milner C.E, Soames R.W., 1997. Anatomical variations of the anterior talofibular ligament of the human ankle joint, Journal of Anatomy, vol. 191, pp. 457-458.

Morvan G., Busson J., Wybier M., Mathieu P., 2001. Ultrasound of the ankle, European Journal of Ultrasound, vol. 14, pp. 73-82.

Nordin M. and V.H. Frankel, 1989. Basic biomechanics of the musculoskeletal system. 2nd ed., Philadelphia: Lea & Febiger. xxiii, 323 p.

Ruth CJ., 1961. The surgical treatment of injuries of the fibular collateral ligaments of the ankle, The Journal of Bone and Joint Surgery, vol. 43, pp. 233-236.

Sarrafian S.K., Anatomy of the foot and ankle : Descriptive, Topographic, Functional, 1983, 1st ed; 1993, 2nd ed. , Philadelphia: Lippincott. xvii, p. 616.

Siegler S, Block J, Schneck CD, 1988. The mechanical characteristics of the collateral ligaments of the human ankle joint, Foot & Ankle, vol. 8, pp. 234-242.

Siegler S., Udupa J.K., Ringleb S. I., Imhauser C. W., Hirsch B. E., Odhner D., Saha P. K., Okereke E. , Roach N., 2005. Mechanics of the ankle and subtalar joints revealed through a 3D quasi-static stress MRI technique. Journal of Biomechanics, vol. 38(3), pp. 567-78.

Takebe K., 1984. Role of the fibula in weight bearing. Clinical Orthopedics and Related Research, vol. 189, pp.289-292.

Taser F., Shafiq Q., Ebraheim N.A., 2006. Anatomy of lateral ankle ligaments and their relationship to bony landmarks, Surgical Radiological Anatomy, vol. 28, pp. 391-397.

Van Den Bekerom M.P.J., Oostra R.J., Alvarez P.G., Dijk N.V., 2008. The anatomy in relation to injury of the lateral collateral ligaments of the ankle, Clinical Anatomy, vol. 21, pp. 619-626.

Van Den Bekerom M.P.J., Raven E.E.J., 2007. The distal fascicle of the anterior inferior tibiofibular ligament as a cause of tibiotalar impingment syndrome: a current concept review, Knee Surgery, Sports Traumatology, Arthroscopy, vol. 15, pp. 465-471.

Wang Q., Whittle M., Cunningham J., Kenwright J., 1996. Fibula and its ligaments in load transmission and ankle joint stability. Clinical orthopedics and related research, vol. 330, pp. 261-270.

Wangdo K. and Voloshin A.S, 1995. Role of plantar fascia in the load bearing capacity of the human foot, Journal of Biomechanics, vol. 2(9), pp. 1025-1033.

Yu H., Alaqtash M., Spier E., Sarkodie-Gyan T., 2010. Analysis of muscle activity during gait cycle using fuzzy rule-based reasoning, Journal of Measurement, vol. 43, pp. 1106-1114.

CHAPTER 2

HISTOLOGICAL CONFIGURATION OF SOFT CONNECTIVE TISSUES WITH RELATION TO THE BIOMECHANICAL BEHAVIOUR OF THE LIGAMENTS OF THE HINDFOOT

2.1 Introduction

Detailed information about the structural and micro-structural configuration of the tissue of the hindfoot ligaments, together with data from mechanical tests, are necessary to define the constitutive formulation that better interprets the mechanical behaviour.

The ligaments are an example of soft connective tissue. They are characterised by strongly hierarchical configurations and the overall mechanical behaviour is determined by the mechanical properties of subcomponents and the biological and mechanical interactions developing between them. The ligaments tissue is composed of few cells embedded within an abundant extracellular matrix (ECM). The ECM is a fiber reinforced composite material, composed of collagen fibers embedded in a ground substance matrix. As regards collagen, details describing the configuration of collagen reinforcing elements, the biological interactions and mechanical properties of its subcomponents are discussed.

The histology of hindfoot ligaments tissue is described, including specific details of the mechanical response and their overall mechanical properties. In order to quantify and understand the contribution of individual ligaments to the overall stiffness characteristics of the joint, data on the biomechanical role of each ligament during movement of the foot are reported.

2.2 Soft connective tissues

Soft tissue is composed of cells and ECM, the cell type is dependent on the particular tissue. Its main functions include: the development of the specific function of the tissue, production, regeneration and remodelling of the ECM and defence against external organisms. The composition, structure and functions of the ECM change greatly in different tissues.

Soft tissue can be initially classified based on the relative abundance of cells and ECM. The connective tissue is characterised by few cells embedded within an abundant ECM, responsible for the particular mechanical response of this tissue. Examples of soft connective tissues are tendons, ligaments and cartilage. Cellular tissue is mainly composed of cells and the minimal ECM serves to separate cells or groups of cells. Muscular, nervous and epithelial tissues are typical examples.

Soft connective tissue performs many functions, including load-bearing (tendons and ligaments), and the protection of organs from injury, as well as providing protective capsules around organs (a fibrous sheath around bones, the dermis, etc.), separation of cells or group of cells within organs and cellular tissues, and immune defence against infection (epimysium, perimysium and endomysium within muscles, epinerium, perinerium and endonerium within nerves, etc.), or insulation and a reservoir of energy (adipose tissues).

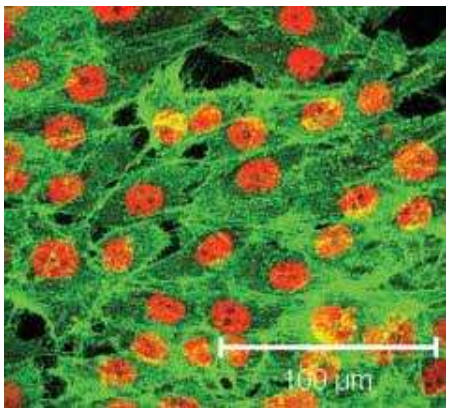

Figure 2.1. Soft connective tissue components: cells and ECM which consists of ground substance and protein fibers

Generally, the cellular material occupies about 20% of the total tissue volume, while the ECM accounts for the remaining 80% (Frank and Shrive 1999). The ECM

consists of two main components: protein fibers and the amorphous matrix. Protein fibers include elastic fibers, which are extremely flexible and behave much in the same way as rubber, and collagen fibers, which are stiff and form the main tensile load bearing components in the tissue. The amorphous matrix or ground substance, in which fibers are embedded, is a viscous gel composed of water, proteoglycans and other glycoproteins (Minns et al. 1973).

Figure 2.2. Photomicrograph of the principal fibers that limit movement and stabilize the body's shape. The blue diagonal line is a single tropocollagen (pre-collagen unit). They combine into the triple helix (three stranded rope) of a collagen molecule (lower middle). The yellow snaky one is elastin. The thin cobweb-like fibers are reticulin - immature collagen found mostly in embryos

As a consequence, soft connective tissue must, therefore, be considered and analysed as a fiber-reinforced composite material (Limbert and Taylor 2002; Minns et al., 1973).

2.2.1. Mechanical behaviour of soft connective tissues

In the context of a fiber-reinforced composite material, fibrous proteins, with particular regard to collagen, represent the reinforcing fibers, while the ground substance is the isotropic matrix (Minns et al. 1973). Consequently, the mechanical behaviour is determined by the properties and abundance of the components and their interactions. Furthermore, the specific orientation of the collagen fibers determines the characteristic anisotropic response.

Because collagen elements are characterised by significantly higher stiffness than ground substance, they are largely responsible for the tensile behaviour of soft

connective tissue. Consequently, the micro-structural phenomena which develop when tensile load increases are mainly associated with collagen elements, with the tensile stress-strain response also qualitatively similar to that of collagen fibers. In contrast, because of the high length-thickness ratio characteristic of collagen elements when compressive loads are applied, micro-buckling of the fibers occurs and the compression behaviour of the tissue is mainly determined by the ground substance and its interaction with the fibrous network.

When compressive loads are applied to the tissue, two main phenomena occur: the ground substance undergoes fluid fluxes within the solid skeleton; and the space between proteoglycans is reduced. Tissue compressive stiffness is consequently determined by the incompressible behaviour of the ground substance, its capacity to move within the fibrous network and the electrostatic interaction between glycosaminoglycans. The ground substance is a non-Newtonian viscous gel and its movement capacity within the solid skeleton strongly depends on the applied strain rate.

As reported in literature (Nishihira et al. 2003) the influence of strain rate on the mechanical response is more evident in compression conditions because the mechanical behaviour is determined by the ground substance.

Very high strain rate conditions prevent ground substance fluxes, resulting in high compression stiffness due to the incompressible nature of the gel. By reducing the strain rate, fluid flux occurs with less resistance and compression stiffness decreases. The microstructural phenomena which develop within soft tissue during loading require time to reach a condition of thermodynamic equilibrium, both for compressive and tensile situations. With regard to the latter case, time-dependence is less evident because micro-structural rearrangements within collagen fibers develop more quickly. As a consequence, the analysis of the mechanical behaviour of the tissue requires consideration of viscosity (Natali et al. 2004a).

2.2.2 Collagen components: configuration and mechanical behaviour

Collagen is the most abundant protein in the human organism. It is primarily responsible for the tensile behaviour of soft connective tissues, and in particular, tendons and ligaments. Collagen is characterised by a strongly hierarchical

organization: small tropocollagen molecules link together to form fibrils, which in turn give rise to fibers and fiber bundles. The primary structure of the tropocollagen molecule consists of an uninterrupted sequence of about 300 Glycine-X-Y triplets, where X and Y are frequently represented by proline. During post-translational modification, hydroxylation, oxidation and glycosylation processes of amino acid residues usually occur (Ottani et al. 2002). The triplets organize themselves into a right-handed α-helix secondary structure and the conformational arrangement is defined by a left-handed helix tertiary structure. The quaternary super-structure of the tropocollagen molecule is obtained by linking three helixes by hydrogen bonds (Figure 2.3).

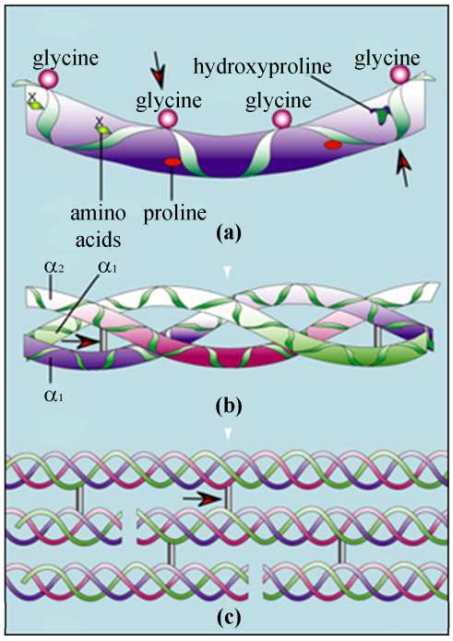

Figure 2.3. Polypeptide chain (a). Possible sites of cleavage by chemomechanical caries removal reagents by degradation of glycine or hydroxyproline are indicated by red arrows. Triple helix (b). Sites of cleavage by degradation of intra-molecular cross links are shown by red arrows (b). With regard to collagen types I, II, III, V and XI, tropocollagen molecules link together to form fibrils. Tropocollagen units assembled to form a collagen fibril. Sites of cleavage by degradation of intermolecular cross links are indicated by red arrows (c)

The molecule is approximately 300 nm in length and 1.5 nm in diameter (Ottani et al. 2002). Tropocollagen molecules are highly reactive and undergo spontaneous fibrillogenesis.

For collagen types I, II, III, V and XI, tropocollagen molecules link together by inter-molecular covalent bonds to form fibrils (Figure 2.3), that are characterised by diameter and length, ranging between 20 to over 280 nm (Silver et al. 2003) and 5 μm to over 1 mm respectively (Kadler et al. 1996). For collagen types I, II, III, V and XI, tropocollagen molecules link together by inter-molecular covalent bonds to form fibrils (Figure 2.3), that are characterised by diameter and length ranging between 20 to over 280 nm (Silver et al. 2003) and 5 μm to over 1 mm respectively (Kadler et al. 1996).

Visualization of collagen fibrils by Transmission Electron Microscopy (TEM) shows that tropocollagen molecules organize themselves in a cross striated structure (Figure 2.5) with a characteristic 67 nm repeat (Silver et al 2003), known as the *D*-period.

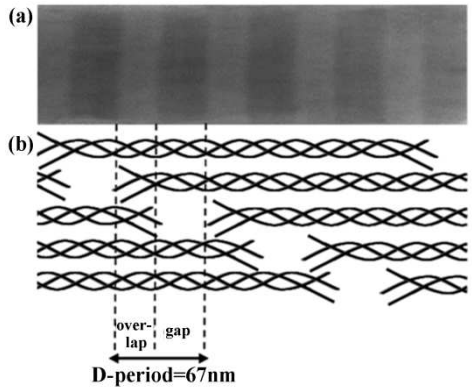

Figure 2.4. Transmission electron microscopy (TEM) image of single fibrils with the 67 nm D-period visible(a). Schematic representation of the two-dimensional axial arrangement of collagen molecules in a microfibril (b). The D-period originates from the staggered aggregation of the collagen molecules in microfibrils

Adjacent repeat elements are separated by a "gap" zone (Ottani et al. 2002). Each repeat element is composed of parallel tropocollagen molecules linked together by covalent bonds. Repeat elements are joined by further covalent bonds passing through the "gap" zone (Figure 2.4). This organization is known as the "*D*-period structure" or the "Hodge-Petruska" model (Petruska and Hodge 1963).

Proteoglycans, most often decorin (Redaelli et al. 2003; Raspanti et al. 1997) and FACIT (fibril associated collagen) filaments (Eyre et al. 2004), serve to form inter-

fibrillar bonds that tie adjoining fibrils together to form fibers (Figure 2.5) and seem to have a definite role in guaranteeing the mechanical coupling of fibrils.

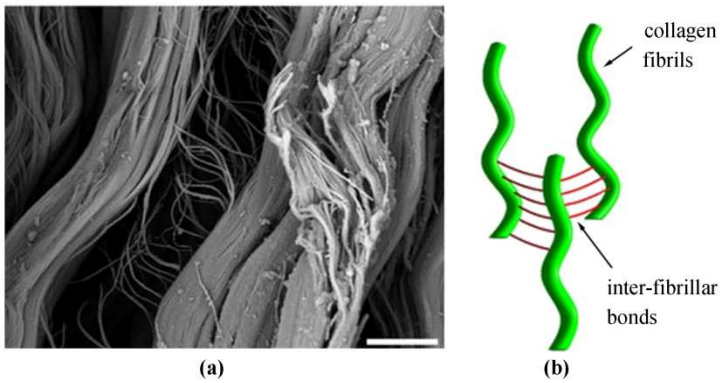

Figure 2.5. Proteoglycans and collagen filaments enable bonds between collagen fibrils. (a) SEM (the horizontal field of view spans 20 μm), from Price et al., 2009, and (b) schematic representation

As mentioned, collagen reinforcing elements can assume different arrangements, such as fibrils, fibers or fiber bundles (Figure 2.6).

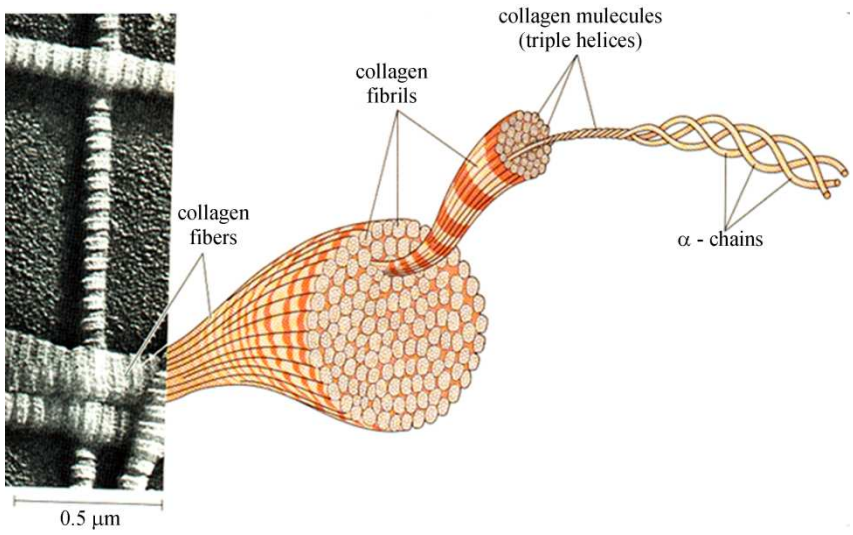

Figure 2.6. The organization of collagen in fibers bundles

Within soft tissue, collagen fibrils show a typical wavy configuration in the unstrained state, referred to as crimped, that is characterised by a helical nature with a periodicity of between 10 and 100 μm (Figure 2.7), depending on the particular tissue type (Freed and Doehring 2005).

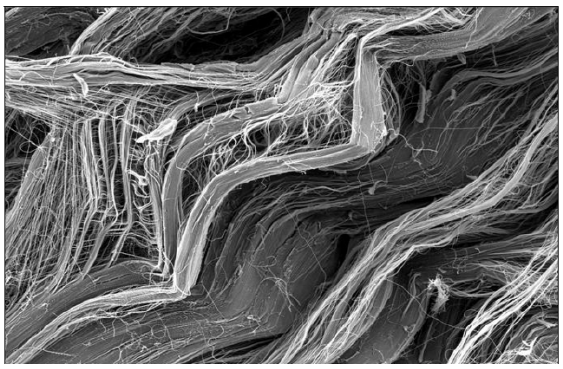

Figure 2.7. Typical wavy configuration of collagen fibrils in the unstrained state. The photographs are acquired by Scanning Electron Microscopy (SEM)

Because of its hierarchical organization, collagen reinforcing elements usually show a complex mechanical response that can be evaluated by analysing the mechanical behaviour of the components and the interactions which occur when tensile loads are applied.

Experimental studies performed by Sasaki and Odajima (1996) on specimens from bovine Achilles Tendon have made it possible to evaluate the stress-strain behaviour of tropocollagen molecules. Linear elastic behaviour was assessed using a 3 GPa elastic modulus. The elastic modulus of the tropocollagen molecule has been investigated by other researchers (Hofmann et al. 1983; Nestler et al. 1983; Cusack and Miller 1979), in samples from different animal species and anatomical sites, demonstrating similar results (ranging between 3 and 5 GPa).

The stress-strain behaviour of an uncrimped collagen fibril was investigated by Sasaki N. and Odajima S. (1996). A linear relationship in accordance with a 400 MPa elastic modulus was obtained (Freed and Doehring 2005; Redaelli et al. 2003).

The difference between the stiffness of tropocollagen molecules and collagen fibrils is determined by the larger number of deformation mechanisms acting within fibrils (Gautieri et al. 2011). In contrast to tropocollagen molecules and collagen fibrils, the tensile behaviour of collagen fibers and collagenous tissue is non-linear. At this purpose a schematic representation of the mechanical response of a collagen fiber is reported in Figure 2.8.

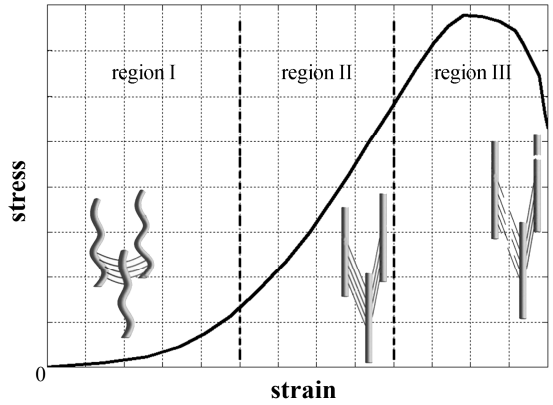

Figure 2.8. Representation of the mechanical behaviour of a collagen fiber

The situation can be explained by considering the crimped configuration of collagen fibrils and the orientation of inter-fibrillar bonds in the unstrained state. The stress-strain curve can be subdivided into three main regions. In the first region (the toe-region), collagen fibers extend, carrying load as an uncoiling spring. The material undergoes a progressive increase in stiffness due to the uncrimping of fibrils and the re-alignment of inter-fibrillar bonds in the direction of loading. In region II (the quasi-linear region), collagen fibrils are completely uncrimped and inter-fibrillar bonds are predominantly aligned along the direction of loading (Reese et al., 2010; Redaelli et al 2003). The material stiffness value is almost constant and reaches its peak.

When strain exceeds a specific limit, damage phenomena develop (region III or damage region). Collagen fibrils and inter-fibrillar bonds progressively breakdown and the material stiffness value decreases until the tissue fails (Natali et al.2004b, 2005). Because of the many deformation mechanisms taking place in collagen fibers, their stiffness is not constant and the value is lower than that of collagen fibrils. In the toe-region and the quasi-linear region, the elastic modulus of collagenous tissue falls in the range of 10 and 100 MPa respectively (Freed and Doehring 2005).

2.2.3 Elastic components: configuration and mechanical behaviour

To limit the deformation and to prevent tearing of the tissues elastic fibers are intermingled with the collagen fibers.

Elastic fibers (Figure 2.9) are fibrous proteins found in large amounts in tissues, such as the elastic walls of the aorta, skin and ligaments.

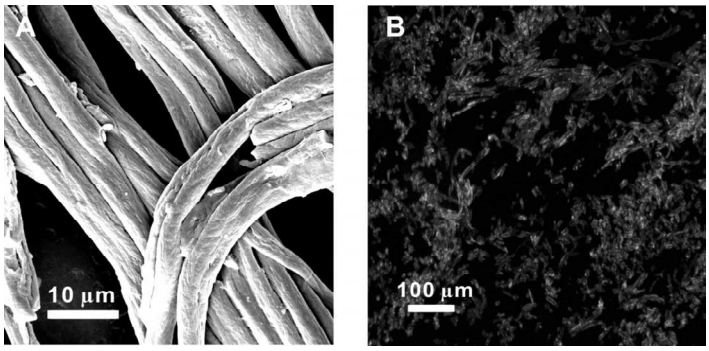

Figure 2.9. SEM image of elastic fibers with diameters in the range of 3 to 5 µm (a). Fluorescence microscope image of immunostained fibrillin-microfibrils in elastic fibers (b). From Yang 2008

The elastic components are thinner than the collagen components. They are branched and unite with one another, forming an irregular network (Figure 2.10). Elastic fibers consist of an amorphous central region containing elastin surrounded by a sheath of 14 nm tubular microfibrils (Yang 2008). The amino acid composition of elastin resembles that of collagen in so far as elastin is rich in glycine (Gly) and proline (Pro). Differences include greater quantities of valine (Val) and alanine (Ala), along with small amounts of hydroxyproline and no hidroxylysine.

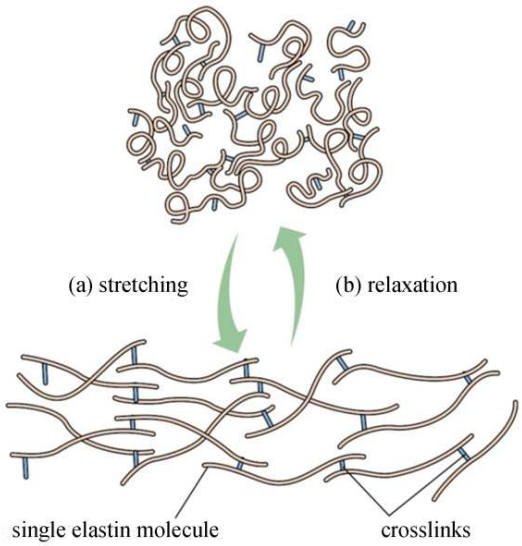

Figure 2.10. Elastin molecules are joined together by covalent bonds to generate an extensive cross-linked network. Because each elastin molecule in the network can expand and contracts as a random coil, the entire network can stretch and recoil like a rubber

Through this structure (Figure 2.10) and its numerous links, elastic fibers are capable of stretching to one and one-half times their length, yielding easily to very small traction forces, but returning to their original shape when these forces are relaxed.
Fung et al. 1993 reported the elastin tensile stress-strain response. Loading and unloading form two different curves, showing the existence of an energy dissipation mechanism in the material, even if the difference is small.

2.2.4 Ground substance: configuration and mechanical behaviour

The amorphous intercellular ground substance is colorness, transparent and homogeneous. It fills the space between cells and fibers of the connective tissue. The ground substance is a viscous gel mainly composed of an electrolytic water solution and highly negatively charged proteoglycans (PGs). The water solution behaves as a pore fluid within the solid skeleton of the extracellular matrix, and dissolved ionic species are mainly sodium Na^+ cations and chloride Cl^- anions. Proteoglycans are long molecular structures developing along an axis made of hyaluronic acid (Figure 2.11).

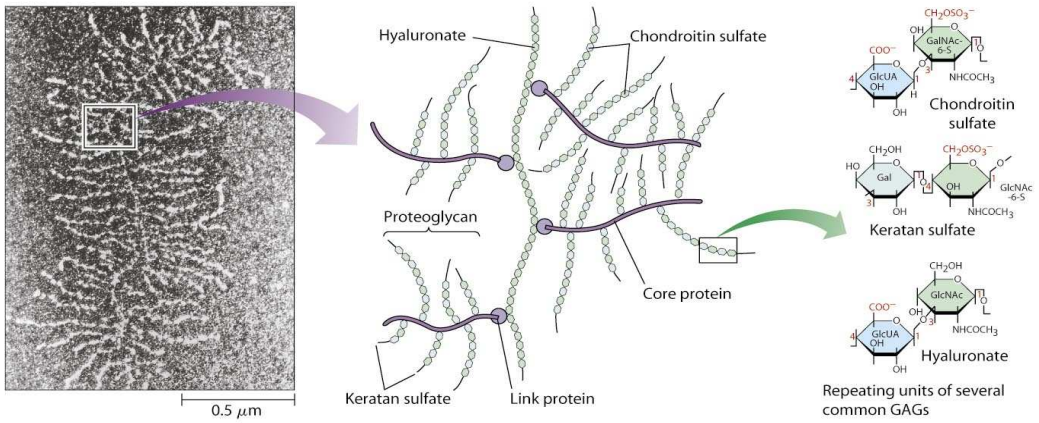

Figure 2.11. SEM micrograph and the schematic representation of the structure of proteoglycans

On that axis other proteins (aggregans) are attached laterally and structured around their own axis. Along this axis, threads of amino-acids, called glycosaminoglycans (GAGs) are attached. The basic structure of GAGs is made by disaccharide units containing a uronic acid and an amino-glycan. The uronic acid displays a negatively charged carboxyl COO^- and the amino-glycan displays at least one sulphate SO_3^-.

The two main GAGs that compose proteoglycans are chondroitin-sulphate with valence -2 and keratin-sulphate with valence -1. Because of the high water content of the ground substance, proteoglycans are hydrated and electroneutrality is ensured by sodium cations (Loret and Simoes 2004).

The compressive properties of soft connective tissues are partly provided by the proteoglycans that resist compression because GAGs repulse each other due to their negative charges (Figure 2.12a). The presence of cations Na^+ shields the negative charges of the PG, and the mutual repulsive forces decrease with increasing sodium concentration (Loret and Simoes 2004). Shielding results in decreasing macroscopic compressive moduli when the salt content increases (Figure 2.12b) (Dean et al. 2006; Eisenberg and Grodzinsky 1985).

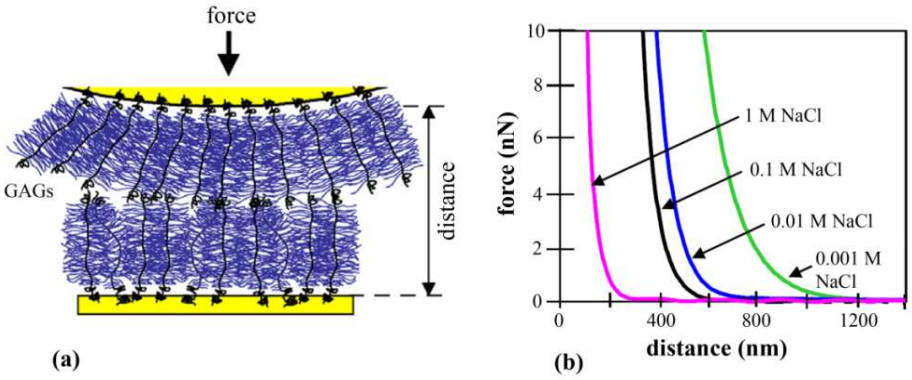

Figure 2.12. Compressive mechanical behaviour of glycosamminoglycans in NaCl solutions. (a) Schematic representation of the experimental setup and (b) experimental results for different concentrations of NaCl. From Dean D. et al., 2006

Time-dependent mechanical properties of soft biological tissue are strongly influenced by the fluid fluxes that the ground substance undergoes when external loads are applied. Fluid flux phenomena depend on the rheological behaviour of the ground substance itself. It has been suggested (Szwajczak 2004) that solutions of biopolymers, such as proteoglycans, are able to organize themselves as liquid crystal polymers (LCPs). LCPs behave as non-Newtonian fluids and their viscosity (Figure 2.13) depends on the strain rate (Szwajczak 2004). In the case of the ground substance of the soft tissue, this behaviour is determined by the combined action of GAGs and hyaluronic acid (Nishimura et al. 1998).

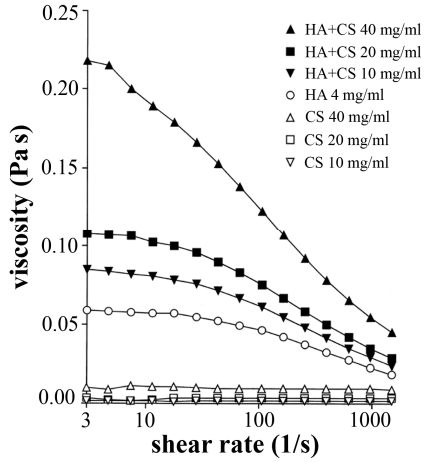

Figure 2.13. Effects of concentration of chondroitin sulphate (CS) and hyaluronic acid (HA) on the viscosity of the water solution at various shear rates. From Nishimura et al. 1998

2.3 Histological configuration of the ankle ligaments

With regard to the soft connective tissues, particular attention is placed on the study of the ligaments. Ligaments are anatomic structures interposed between bones, permitting locomotion and enhancing joint stability. Because of their predominant role in stabilizing the foot during movement, the ankle ligaments have been studied in detail.

Ligaments are soft collagenous tissues with a hierarchical structure (Figure 2.14) that affects their mechanical behaviour. In addition, they can adapt to changes in their mechanical environment due to injury, disease or exercise.

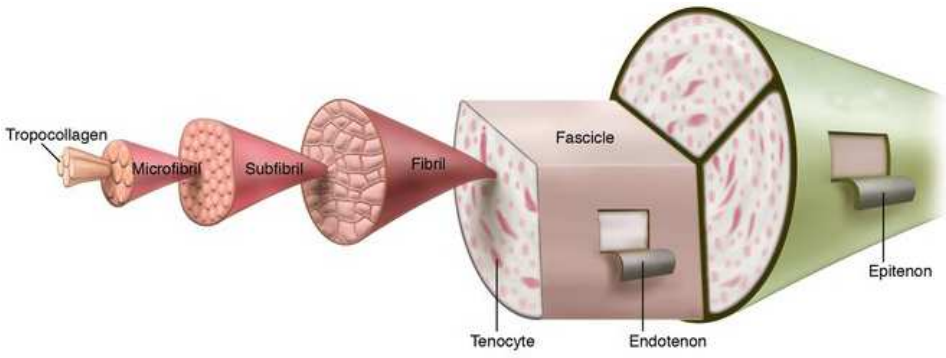

Figure 2.14. Hierarchical structure of ligaments

As reported by Weiss and Gardiner (2001) ligaments are composed by a ground substance matrix reinforced by collagen and elastin. The ground substance matrix is

composed of proteoglicans, glycolipids, fibroblasts and large amounts of water. Ligaments are relatively hypocellular with interconnected, elongated fibroblastic cells in their mid-substance and more rounded cells found near their insertion to the bone. The primary function of the cells is to maintain the collagen scaffold. Water makes up about two thirds of the weight of normal ligaments, 70 to 80 % of the remaining weight being made up of fibrillar protein collagen. Ligaments consist of closely packed, parallel collagen fibers (Figure 2.15) which appear to have various degrees of undulation forming along the axis of each fiber at a resting length. The helical shape of various wave sizes of each fiber or group of fibers (bundles) gives rise to a process called “recruitment” (Solomonow 2009).

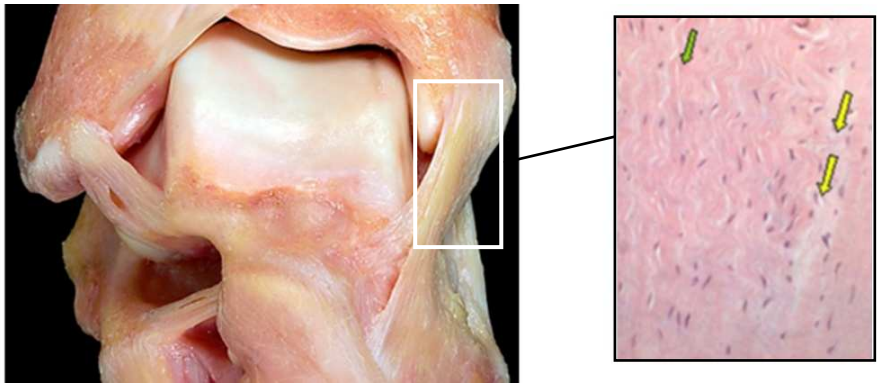

Figure 2.15. Anterior tibio talar ligament (ATTL). Green arrow: parallel and waveform collagen fibers. Yellow arrows: poor vascularization (Keller et al. 2010)

In detail, the anterior talofibular ligament (ATFL) consisted of typical dense fibrous connective tissue with fibroblasts lying between bundles of collagen fibers. Fibroblasts are responsible for the production of connective tissue components, namely fibers and amorphous substance. When they become inactive they are called fibrocytes by some authors, whereas others prefer to use the term fibroblasts, as they can still take action in any moment of their synthesis. They are generally arranged along the collagen fiber bundles and appear in histological sections with an elongated form.

As reported in the following table, in the central part of the ligament collagen types I, III and VI are presented, while in the enthesis of the fibula and talus there is also collagen type II.

	enthesis		wrap around region		
antigen (antibody)	fibula	talus	sesamoid fibrocartilage	talar articular cartilage	rest of ligament
collagens					
I	+	+	+	–	+
II	+	+	+	+	–
III	+	+	+	–	+
VI	+	+	+	+	+
glycosaminoglycans					
DS (2b6+ChABC)	+	+	+	±	+
KS (5D4)	+	+	+	±	+
C4S (2B6+ChAC)	+	+	+	+	±
C6S (3B3+ChAC)	+	+	+	+	±
proteoglycans					
versican (12C5)	+	+	+	±	+
aggrecan (1C6)	+	+	+	+	±

Table 2.1. Histology of the anterior talofibular ligament (Kumai et al. 2002). + present, - absent, ± detected weakly. C4S chondroitin 4 sulphate, C6S chondroitin 6 sulphate, ChABC chondroitinase ABC, Ch AC chondroitinase AC, DS dermatan sulphate, KS keratin sulphate

Occasional blood vessels are present in the endotenon and epitenon and a highly vascular synovial membrane lines its deep surface. In the region where the ligament wraps around the lateral articular surface of the talus there are the fibrocartilage cells which constitute a sesamoid fibrocartilage (Figure 2.16).

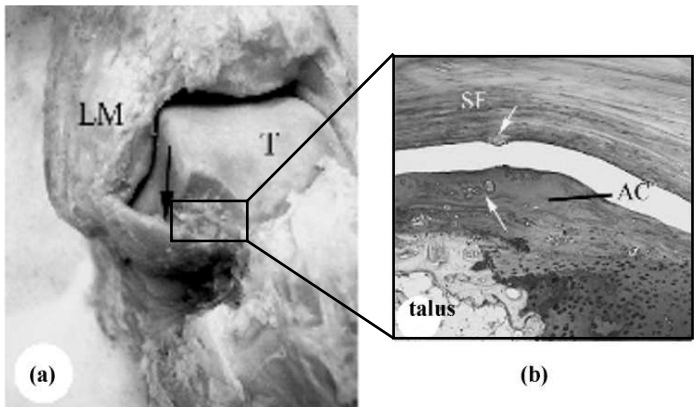

Figure 2.16. A dissection of the ATFL ligament (a) showing the region where it wraps around the lateral articular facets of the talus. Enlargement view (b) of the talar end of the ATFL. The articular cartilage is indicated as AC while the sesamoid cartilage is indicated as SF

2.3.1 Bone-ligament insertion sites

Ligament insertion sites transfer loads between components of the skeleton. They are designed to reduce the stress concentrations that naturally occur as forces are transferred along the ligament bone interface. The junction between the soft tissues of ligaments and the hard tissue of bone is complex and can vary greatly from ligament to ligament, as well as between the two ends of the same ligament. Ligaments insertion sites have been classified into two groups: indirect and direct.

The attachment of the superficial fibers to bone occurs mainly through fibers that blend with the periostium (i.e. a membrane of dense connective tissues that lines the outer surface of all bones). The deep fibers of direct insertions (Figure 2.17) have been shown to attach directly to the bone at acute angles without the fibrocartilagineous transitional zone observed in indirect insertions.

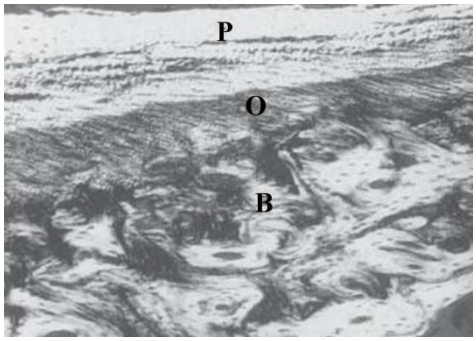

Figure 2.17. A direct type of ligament insertion. There is a broad zone of fibrous tissue (O) connecting the periosteum (P) with the underlying bone (B)

Indirect insertion sites (Figure 2.18) are generally well defined areas with a sharp boundary between the bone and the attached ligament occurring over a distance of less than 1 mm. The collagen fibrils quickly pass out of the normal ground substance matrix and continue through zones of fibrocartilage, mineralized fibrocartilage and finally into the bone. Most of the fibrils at indirect insertion sites are deep fibrils that meet the bone at approximately right angles. Indirect insertion sites attach to the bone over a broader area than indirect insertion sites and have a more gradual transition between a hard and soft tissue.

The talar and fibular entheses of the ATFL are an example of indirect insertions. Fibrocartilage is present at both entheses. Therefore, at each attachment site, four

zones of tissue could usually be identified: pure dense fibrous connective tissue, uncalcified fibrocartilage, calcified fibrocartilage and bone (Figure 2.18).

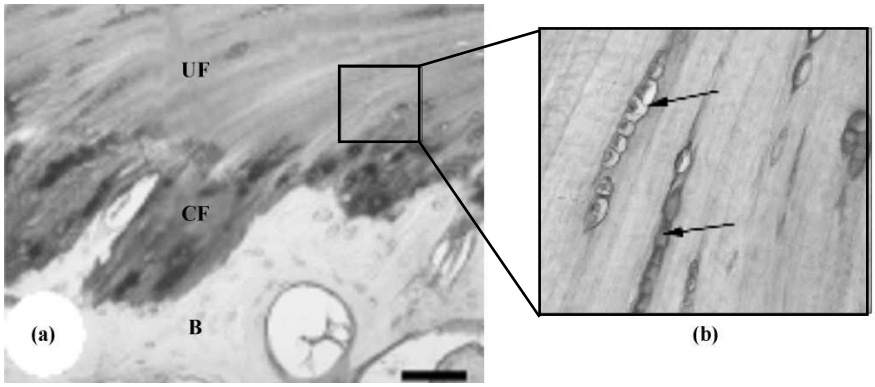

Figure 2.18. Example of an indirect insertion: fibular entheses of the ATFL. (a) It shows the typical zones of uncalcified fibrocartilage (UF), calcified cartilage (CF) and bone. (b) It shows details of uncalcified fibrocartilage at the fibular entheses: the arrows indicate rows of fibrocartilage cells

The two zones of fibrocartilage are separated by one or more tidemarks and the cells in the uncalcified region are generally arranged in longitudinal rows (Figure 2.18b). The quantity of uncalcified fibrocartilage is significantly greater at the fibular than the talar end of the ligament. The different bone density is reported in the Figure 2.19.

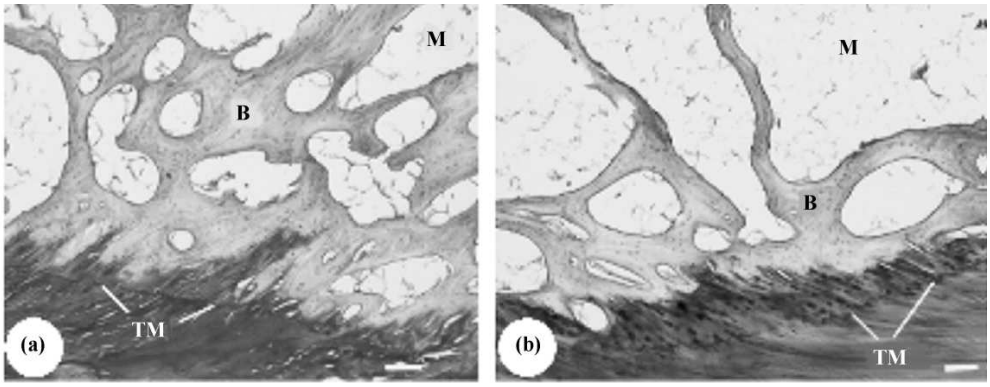

Figure 2.19. Differences in bone density between the talar (a) and fibular (b) entheses of the ATFL. TM indicate the tidemark between the uncalcified fibrocartilage and calcified cartilage

Despite the gradual change from soft to hard tissues, insertion sites are often the location of injuries.

In response to immobilization or injury insertion sites have been shown to heal more slowly than ligament midsubstance tissues. This may be due to the lack of a significant blood supply in the ligament substance near the insertion site.

2.4 Biomechanical behaviour of the ligament tissue

Ligaments are functional (effective) under tension, or when stretched and completely non-functional in compression or when shortened below their resting length. The general response of ligaments to stretch or tension is rather complex and non-linear, and subject to several time-dependent phenomena, such as creep, tension–relaxation, strain rate and hysteresis.

Tensile test. The general stress-strain behaviour of a ligament is non-linear. Figure 2.20 reports the tensile response of the anterior talo-fibular ligaments of the ankle.

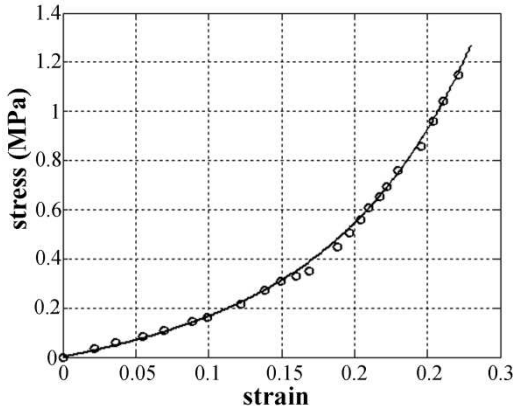

Figure 2.20. Stress-strain behaviour of the anterior talo-fibular (ATFL) ligament (5 cm/sec). (Attarian et al. 1985a)

When axial stretching of a ligament is applied, fibers or bundles with a small helical wave appearance straighten first and begin to offer resistance (increased stiffness) to stretching. As the ligament is further elongated, fibers or fiber bundles of progressively larger helical wave straighten and contribute to the overall stiffness. Once all the fibers are straightened, a sharp increase in stiffness is observed. Over all, the recruitment process gives rise to a non-linear length–tension relationship of a ligament. The initial segments of the curve demonstrate a rather large strain for a very small increase in load. Once all the waves in the collagen fibers of the ligament

have been straightened out, and all of the fibers recruited, additional increase in strain is accompanied by a rapid increase in tension. The resting length of ligaments is a difficult issue to establish due to the complexity of measurements in vivo.

Creep test. When a constant load is applied to a ligament, it first elongates to a given length. If left at the same constant load, it will continue to elongate over time in an exponential fashion up to a finite maximum. This elongation over time is termed "creep", and is expressed as the percent elongation relative to the length it arrived to immediately after the load was applied. Figure 2.21 depicts the response of a ligament to a constant load over time, as well as the creep. The recovery of the creep with rest, after the load is removed, is also shown (Solomonow et al. 2003).

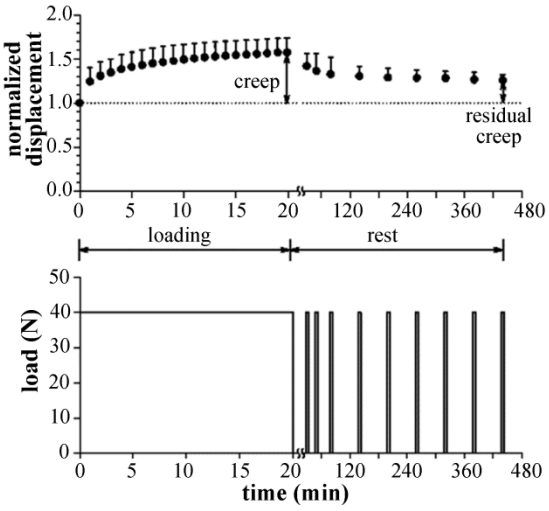

Figure 2.21. The response of the supraspinous ligament to a constant load (40 N) applied for a 20 min period exhibits the development of creep. The recovery during 7 h rest was not complete. In the rest period, short (6 s) loading tests were applied to determine the residual creep (Solomonow et al. 2003)

Stress–relaxation test. When ligaments are subjected to a stretch (or constant elongation) over time the tension–relaxation phenomena is observed. The tension in the ligament increases immediately upon elongation to a given value. As time elapses, the tension decreases exponentially to a finite minimum while the length does not change. In the literature there are several works that report the stress relaxation test on human ligaments (Pavan et al. 2011; Bonifasi-Lista 2005). Figure

2.22 depicts the stress–relaxation phenomena of the plantar aponeurosis (Pavan et al. 2011) for different strain rate condition.

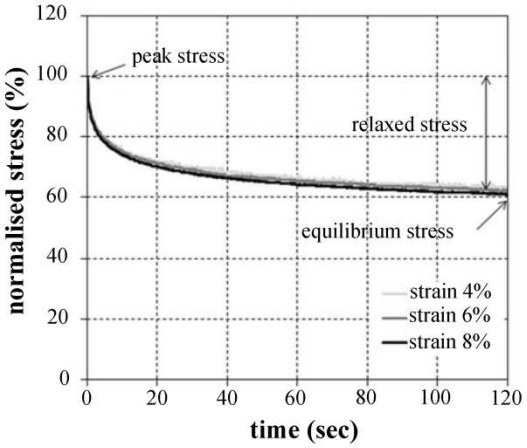

Figure 2.22. Stress-time response of the plantar aponeurosis (Pavan et al. 2011)

Hysteresis and the influence of the strain rate in the mechanical response. Another important behavioural property of ligaments is its inability to track the same length–tension curve when subjected to a single stretch–release or load–unload cycle, namely hysteresis. This phenomenon is also associated with repetitive motion when a series of stretch–release cycles are performed over time. In Figure 2.23 hysteresis loops for an anterior tibiofibular (ATiFL) ligament specimen for a different strain rate is reported. The stiffness of the specimen is seen to increase at higher strain levels.

The tension developed in a ligament also depends on the rate of elongation or strain rate. In general, slow rates of elongation are associated with the development of relatively low tension, whereas higher rates of elongation result in the development of high tension. Fast stretching of ligaments, such as in high-frequency repetitive motion or in sports activities, is known to result in high incidents of ligamentous damage or rupture. Fast rates of stretch, therefore, may exceed the physiological loads that could be sustained by a ligament safely, yet it may still be well within the physiological length range. Development of high tension in the ligaments may result in rupture and permanent sensory–motor deficit to the joint, in addition to deficit in its structural functions

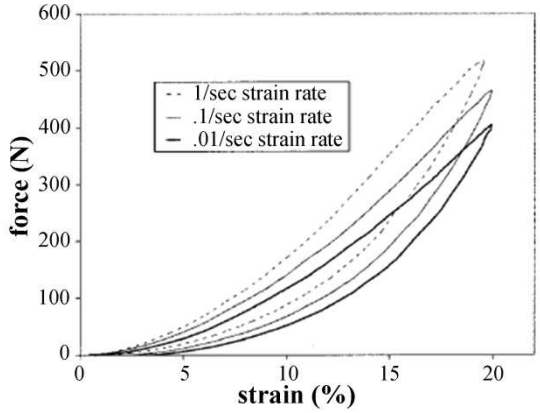

Figure 2.23. Hysteresis loops for an anterior tibiofibular (ATiFL) ligament (Funk et al. 2000)

In similar activities, minimizing the speed of motion for a given task can contribute towards safer working conditions, especially when such tasks are repetitive. In sports activities, however, the high velocity of motion is favored and necessary for success, yet it poses a high-risk of injury or damage. The impact of progressive hysteresis, therefore, is manifested by gradually decreasing tension in the ligament, development of joint laxity, reduced joint stability and an increased risk of injury. Repetitive sports and occupational tasks should be limited in duration and allow sufficient rest periods to facilitate the recovery of normal ligament function.

2.4.1 Biomechanical behaviour of the ankle ligaments

To understand the mechanical behaviour of the ankle tissues specific experimental tests are studied. Further to quantifying and understanding the contribution of individual ligaments to the overall stiffness characteristics of the joint, data on the biomechanical role of the ligament in the kinematics of the foot are reported in these paragraphs.

2.4.1.1 Tensile tests on the ankle ligaments

In literature there are several works that consider the mechanical behaviour of the ankle ligaments (Funk et al. 2000; Siegler et al. 1988; Attarian et al. 1985a, 1985b).
With the aim of characterizing the elongation behaviour of a specific ankle ligament, experimental specimens were prepared from fresh cadaveric human ankles to achieve the specific bone-ligament-bone structure. Ankles were dissected and soft tissues

removed to leave only the tibia, fibula, talus and calcaneus and their ligamentous attachments intact. Ligament dimensions were measured with caliper while the mechanical tests were performed on a Minneapolis Testing System servocontrolled hydraulic testing machine. The anatomical data of the ligaments are reported in Table 2.2.

	Length (cm)	Cross sectional area (cm^2)
ATFL	1.05	0.129
CFL	1.75	0.097
PTFL	1.53	0.400
ATTL	1.200	0.135
PTTL	1.07	0.226
TCL	3.17	0.432
ATiFL	0.72	0.400
PTiFL	0.98	0.380

Table 2.2. Anatomical data of the ankle ligaments (Funk et al. 2000; Siegler et al. 1988; Attarian et al. 1985a)

Each bone-ligament-bone preparation were tested as an isolated structure to avoid the effect of the other ligaments. Specifically, the calcaneo-fibular ligament was tested by bolting the fibula and calcaneus to the upper and lower MTS deflection brackets, while the anterior and posterior tibiotalar ligament was tested by bolting the tibia and talus to the two deflection brackets. The experimental set up is reported in Figure 2.24. The ligament not being tested was transected to prevent mechanical interference. All ligaments were subjected to tension in line with their fibers. With regard to the experimental tests reported by Attarian et al. 1985, the testing protocol consisted of an initial preconditioning of each specimen to establish a mechanically stabilized state. Several load deflection tests at constant velocity, varying from 0.01 to 10 cm/sec, were performed at physiologic deflections. Finally, constant velocity load to failure test was carried out at deflection rates of 80 to 100 cm/sec.

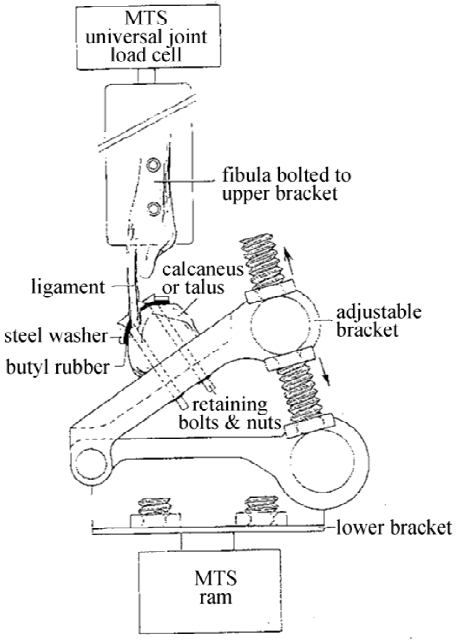

Figure 2.24. Mounting configuration for lateral ankle ligaments. Attarian et al. 1985a, 1985b

The authors reported the experimental results of the ATFL and CFL ligaments under different loading rates. In Figure 2.25 the experimental results at 0.01 cm/sec and 5 cm/sec are illustrated.

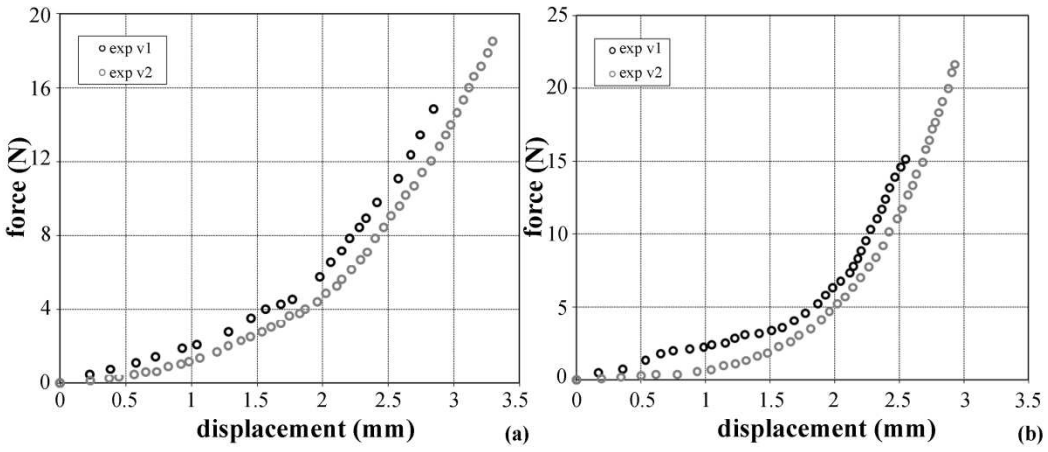

Figure 2.25. Force-displacement response for anterior talofibular (a) and calcaneofibular ligament (b) at different loading rates: v1=5cm/sec, and v2=0.01 cm/sec (Attarian et al. 1985)

The ligaments demonstrate non-linearity in their force-displacement curves and direct strain rate dependence. The biomechanical characteristics of the ankle ligaments studied by Attarian et al. are reported in Table 2.3.

	ATFL	CFL	PTFL	ATTL
Maximum load (N)	138.9 ± 23.5	345.7 ± 55.2	261.2 ± 32.4	713.8 ± 69.3
Deflection to failure (cm)	0.51 ± 0.05	0.63 ±0.05	1.31 ± 0.16	1.05 ±0.11
Strain to failure	0.53 ±0.06	0.38±0.03	1.00 ± 0.15	2.10 ± 0.23
Linear modulus of elasticity (N/cm)	399.9 ± 85.4	705.1 ± 69.0	397.5 ± 137.9	1288.2 ± 250.4
Rate of deflection (cm/s)	101 ± 7	106 ± 4	82 ± 13	80 ± 13

Table 2.3. Biomechanical characteristics of the ankle ligaments (Attarian et al. 1985)

To understand the mechanical behaviour of the other ligaments of the ankle, additional experimental tests have been investigated. In particular, the work of Funk et al. 2000 has been considered (Figure 2.26).

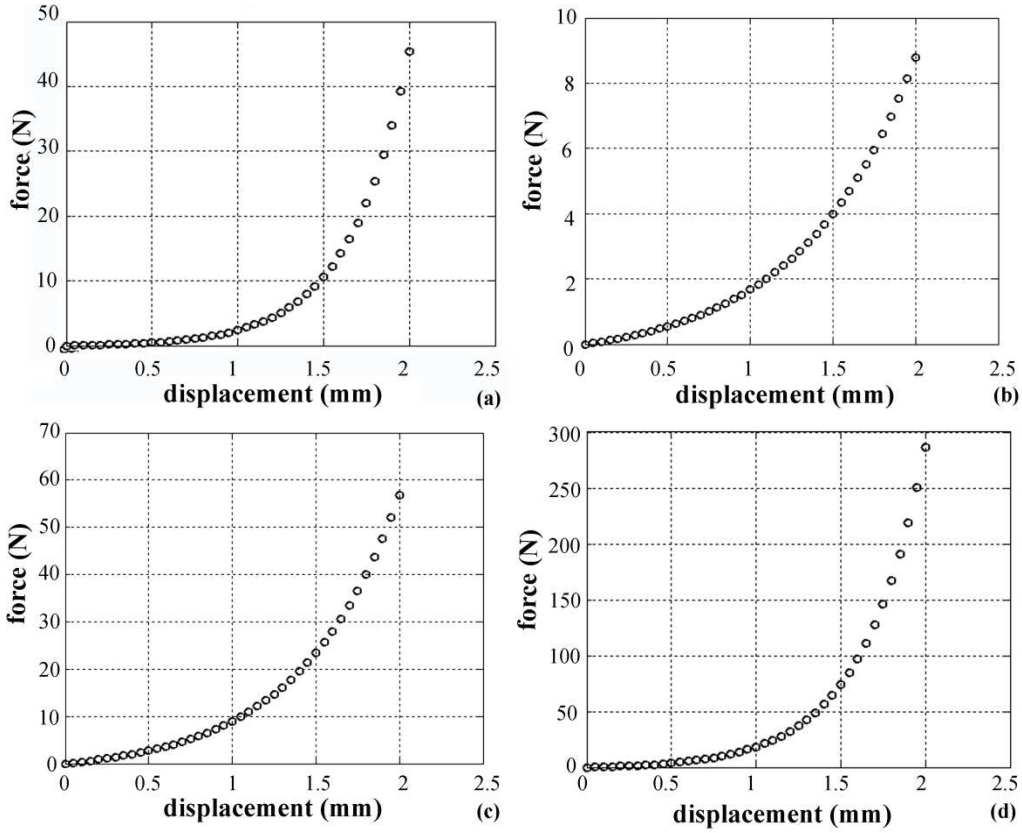

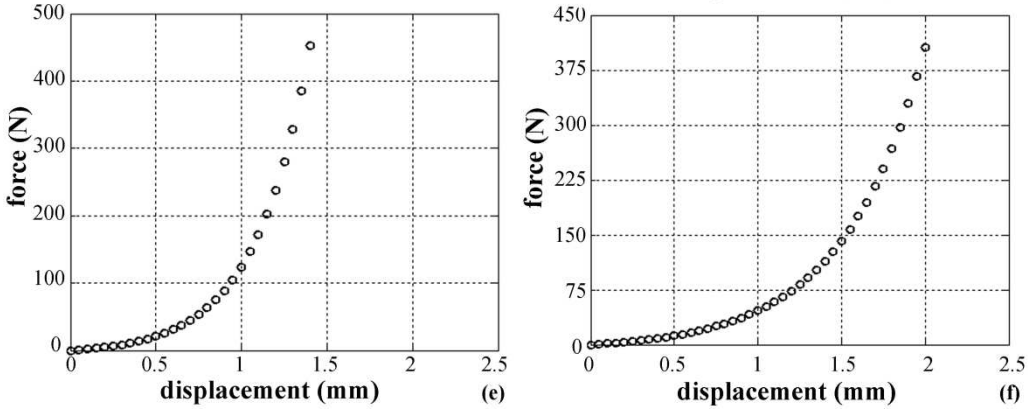

Figure 2.26. Force-displacement response for the PTFL (a), TCL (b), ATTL (c), PTTL (d), ATiFL (e) and PTiFL (f) at 28 cm/sec (Funk et al. 2000)

The authors performed elongation tests on the PTFL, ATTL, PTTL, TCL, ATiFL and PTiFL ligaments. The bone-ligament-bone specimens were tested at high strain rate (28 cm/sec) to characterize the instantaneous response of the structure. The force-displacement response are reported in the Figure 2.26.

On observing experimental evidence, the biomechanical behaviour of the ankle ligaments is characterized by large displacements and strains, almost incompressible behaviour, a non linear stress strain relationship and time dependent effects.

2.4.1.2 Evaluation of the strain in the central part of the ankle ligaments during joint motion

Some authors (Ozeki et al. 2002) performed tensile tests on the ankle ligaments to evaluate the value of the strain at which each ligament began to load resistance ("zero strain reference length (L_0)"). In detail bone-ligament-bone samples were prepared and elongated at a speed of 45 mm/min. The L_0 of the ATFL, CFL, PTFL and TCL is equal to 20.44 mm, 30.84 mm, 24.37 mm and 27.42 mm, respectively.

Nevertheless, to improve or develop ligament reconstruction procedures for the ankle ligaments, it is necessary to know the strain change pattern of each ligament during a range ankle motion. To this purpose in literature there are several works that report the strain changes of the central part of the ankle ligaments (Ozeki et al. 2002; Bahr et al. 1998; Colville et al. 1990; Nigg et al. 1990; Renstrom et al. 1988). Ozeky et al., performed experimental tests on twelve fresh frozen distal lower limb specimens. All muscles, tendons and vessels were removed from the specimen, keeping intact the

ligaments and the capsular structures of the joint. Strain gauge transducers were used in order to measure changes of the whole length ligament. To implant the transducer along each ligament, drill holes were made in the tibia, the fibula, the calcaneus and the talus, so that the center of the hole was located at the center of the attachment site of each ligament. Through each drill hole, the transducer was implanted in the center of each ligament, in alignment with the orientation of the fibers.

To measure the angle a modified TRIAX Electrogoniometer was attached to the tibia and calcaneus in order to continuously monitor the ankle flexion angle. This work reports the relation between the strain of 12 specimens and the flexion angle from 40° plantarflexion to 30° dorsiflexion. The experimental results are reported in Figure 2.27.

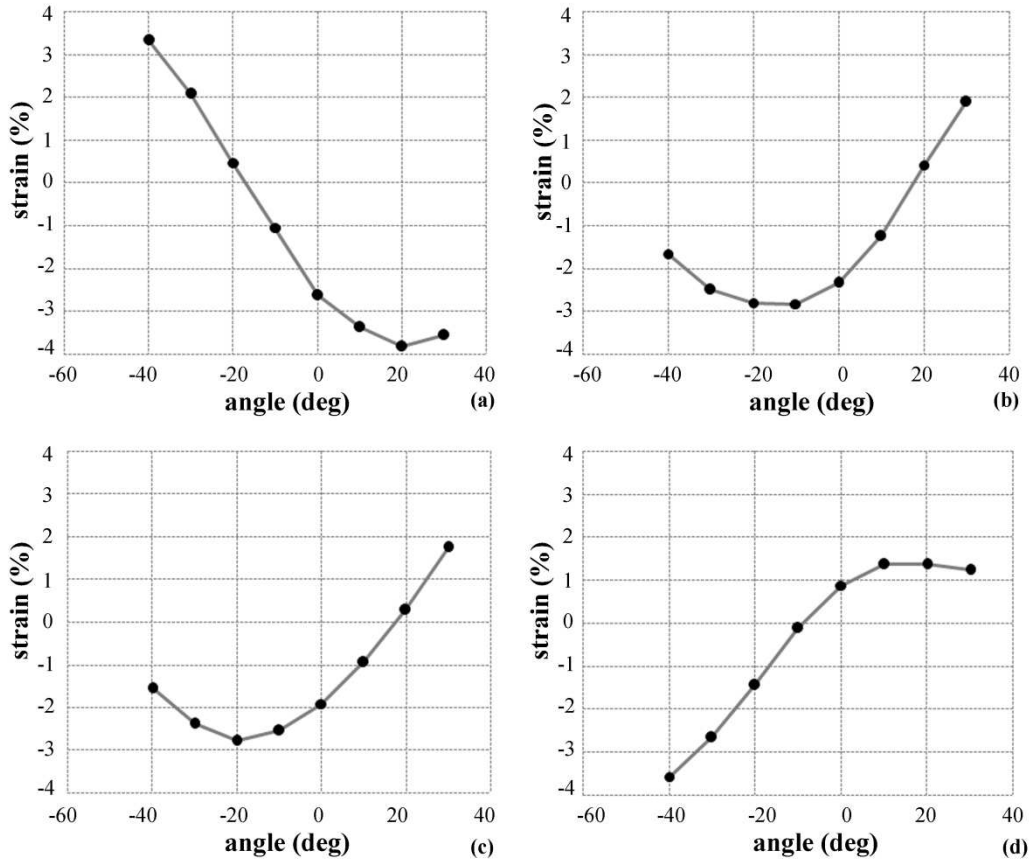

Figure 2.27. The flexion angle-strain curve of several ligaments of the ankle: (a) ATFL,(b) PTFL, (c) CFL and (d) TCL. The Y axis indicated the strain and the X-axis indicated the dorsi/plantarflexion angle. The dorsiflexion and the plantarflexion angle are reported as plus and minus on the X-axis, respectively (Ozeki et al. 2002)

The strain of the ligament (%) reported in the previous graphs was evaluated as $(L_q - L_0)/(L_0)$ where Lq indicates the ligament length at q° of ankle dorsi-plantar flexion.

In order to understand the ligament function of the ankle, it is necessary to know the length changes of each ligament. The ATFL become longer in plantarflexion and become shorter in dorsiflexion: from 40° of plantarflexion to 10° of dorsiflexion significant strain decrease is observed. The flexion angle-strain curves of the PTFL has an opposite pattern to the ATFL. The PTFL become longer in dorsiflexion: from 10° of plantar flexion to 30° dorsiflexion significant strain increase is observed. A similar pattern is observed for the CFL. The TCL become longer around the neutral position and become shorter, both in plantarflexion and dorsiflexion. From 40° plantarflexion to 10° dorsiflexion, significant strain increase is observed.

These results show that the ATFL is elongated during plantarflexion and that the averaged zero strain reference of the central fibers of the ATFL is located at approximately 16° of plantarflexion. This means that the central ATFL functions only in plantar flexion greater than 16°. The PTFL and the CFL are elongated during dorsiflexion. For both of them the zero strain reference is located at 18°, so it is possible to assume that they function in dorsiflexion greater than 18°. These three ligaments are relaxed at the neutral position of the ankle while the TCL is elongated around the neutral position. It is important underline that this study is limited regarding the central part of the each ligament without a loading condition.

2.4.1.3 The role of the ankle ligaments during the movements of the foot

Because the clinically used diagnostic techniques yield inconsistent results, several experimental techniques have been developed to examine the mechanical response of the ankle to load in vivo and in vitro. In the first case the devices are designed to measure in vivo ankle laxity to mimic the clinically anterior drawer test and talar tilt test. In the second case it is possible to study the effects of ligament damage by sectioning the lateral collateral ankle ligaments and loading the ankle minimally in an anterior drawer test and in eversion or inversion. To this purpose two main devices have been used: the ankle flexibility tester (AFT) and the MR compatible ankle loading device (ALD).

The AFT (Figure 2.28) is a manually-operated six degrees of freedom instrumented linkage that quantifies the load displacement characteristics of the hindfoot. Forces and moment are applied along clinically relevant axes (e_1, e_2, e_3) and the subsequent load displacement data are recorded using a data acquisition system.

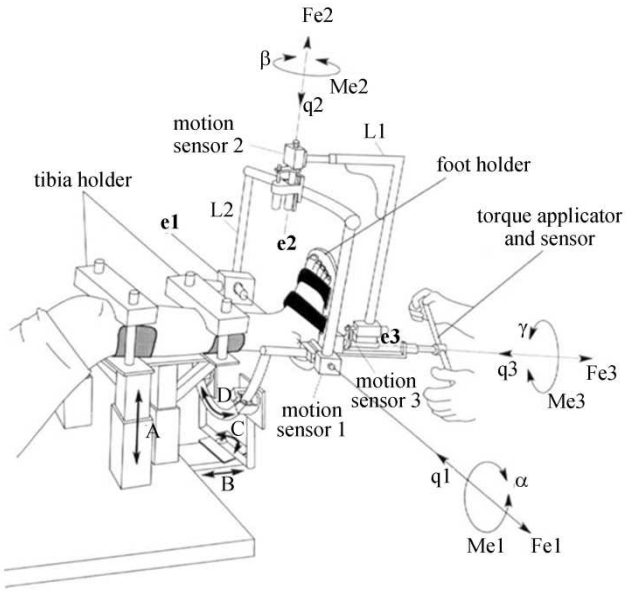

Figure 2.28. The ankle flexibility tester (AFT)

The definition of the six degrees of freedom of both the AFT and the ALD are based on the Grood and Suntay anatomical coordinates.

In detail, axis e_1 is fixed to the tibia and is aligned with the intermalleolar axis. The rotation around it (α) corresponds to dorsi/plantarflexion. Translation along it (q_1) corresponds to lateral/medial shift. Axis e_2 is a floating axis which remains mutually perpendicular to e_1 and e_3. Rotation around it (β) corresponds to inversion/eversion, while translation along it (q_2) corresponds to anterior/posterior drawer. Finally, axis e_3 is fixed to the calcaneus and is aligned perpendicular to the plantar aspect of the foot. Rotation around it (γ) corresponds to internal/external rotation, and translation along it (q_3) corresponds to compression or distraction.

The ALD (Figure 2.29) is an MR-compatible, non-metallic loading device. This six degrees of freedom linkage allows unconstrained hindfoot motion and locks the joint in any position.

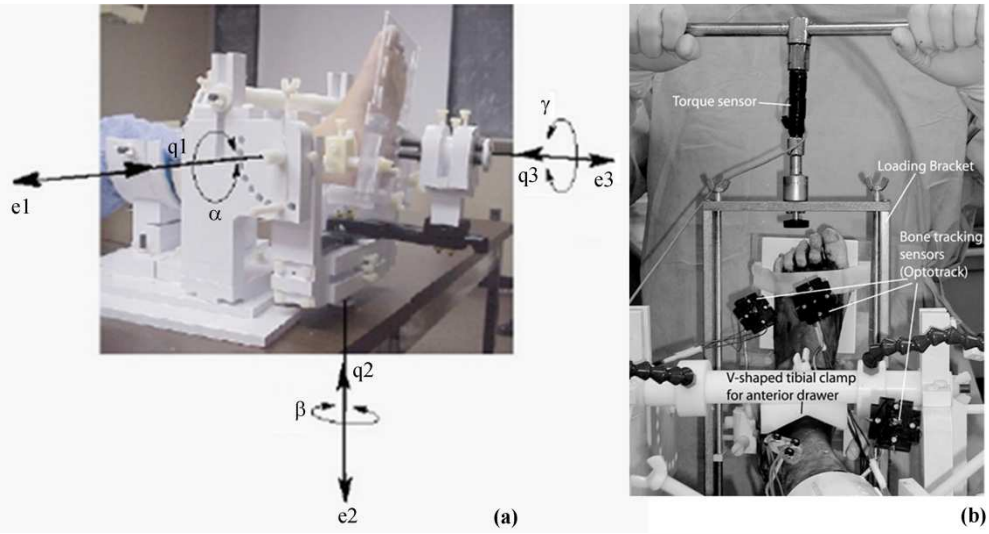

Figure 2.29. The MR compatible ankle loading device (a) and a detail of the MR compatible ankle loading device (b)

For in vivo testing, the patient lays prone on the MR gurney and the tester secured his/her shank to the linkage. The foot is then placed on the footplate and the heel is secured with medial, lateral and posterior clamps. For in vitro testing the distal tibia and fibula are cemented into a plastic PVC cylinder and secured to one end of the ALD. The calcaneus is rigidly fixed to the footplate with a threaded road. As reported in Figure 2.29b a v-shaped clamp immobilizes the tibia for the anterior drawer test. A detachable u-shaped aluminum bracket enables the application of the inversion moment and the anterior drawer force. The loads are applied outside the scanning room so that the electrical strain gauge torque and force sensors can be used to make the measurements without being influenced by the magnetic field. The external movement of the hindfoot is measured between the footplate and the base through linear and angular scales attached to the ALD.

The damage of the lateral collateral ligaments of the ankle causes specific and detectable changes in flexibility and range of motion of the joint. In literature there are several studies that determine if the damage to the collateral ankle ligaments has a significant effect on the flexibility characteristics of the ankle in vitro; if so, differences in flexibility could be used to distinguish between various ligament injuries in vitro.

The AFT device is used to measure the three dimensional flexibility characteristics of the ankle. The systems measure the relative motion between the calcaneus and the

tibia-fibula in response to moments and forces applied manually across the ankle joint. In the study reported by Lapointe et al. 1997, six lower limbs from embalmed cadavers were tested intact after serial sectioning of the anterior talofibular and calcaneofibular ligaments. The limbs were disarticulated at the knee, and all the soft tissues and skin are left intact.

Each test, including anterior drawer, inversion-eversion, and internal external rotation, consisted of the application of a moment or force for six continuous cycles. The results obtained from one specimen of the in vitro tests are reported in Figure 2.30.

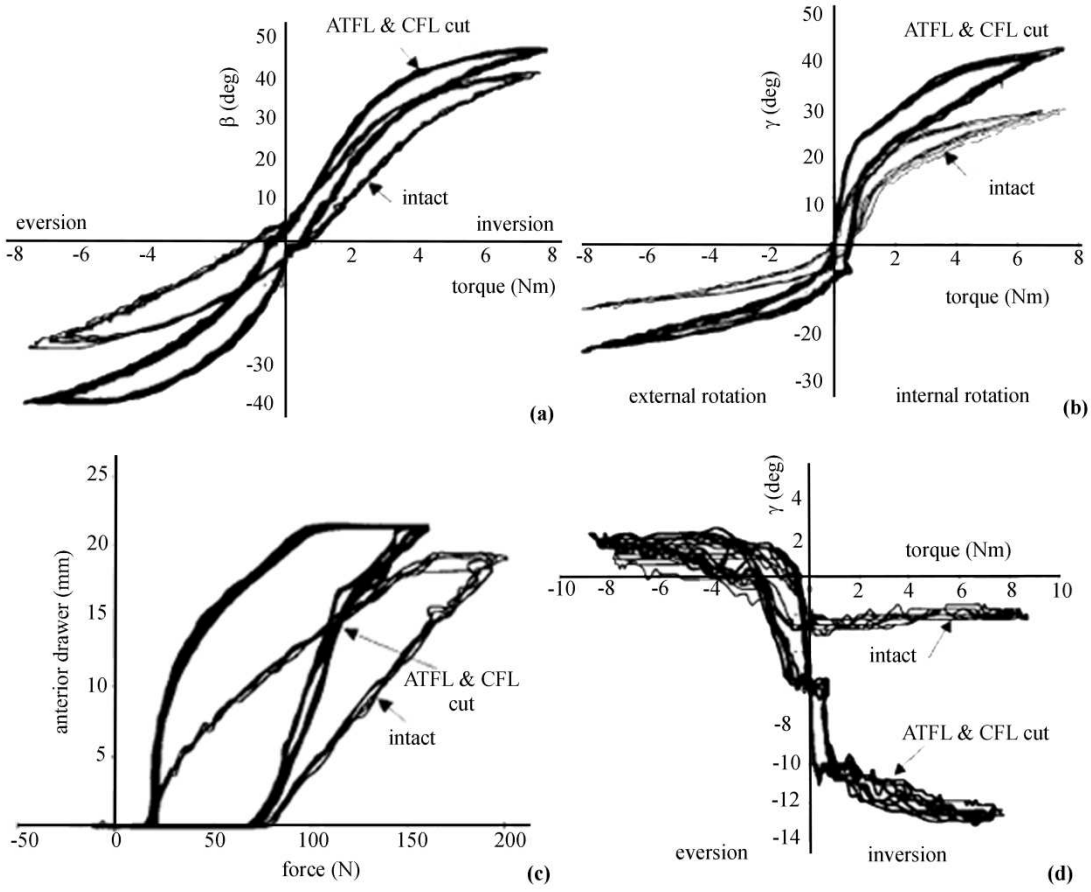

Figure 2.30. The flexibility characteristics of the ankle sectioning both the anterior talofibular ligament (ATFL) and the calcaneofibular ligament (CFL) during inversion/eversion (a), internal/external rotation (b), anterior drawer test (c) and coupling between internal rotation and inversion and between external rotation and eversion (d)

For example, during testing in inversion-eversion, the ankle was loaded by applying a moment in inversion, unloading, loading in eversion, and unloading once again to complete one cycle. An instrumented torque wrench was used to apply a moment in inversion-eversion and internal external rotation. Force wass applied in the direction of the anterior drawer with a load cell.

To compare the mechanical behaviour of the ankle joint with intact ligaments and after sectioning the ATFL and CFL ligament, the authors evaluated the early, the late and the total flexibility of the joint during the different experimental conditions.

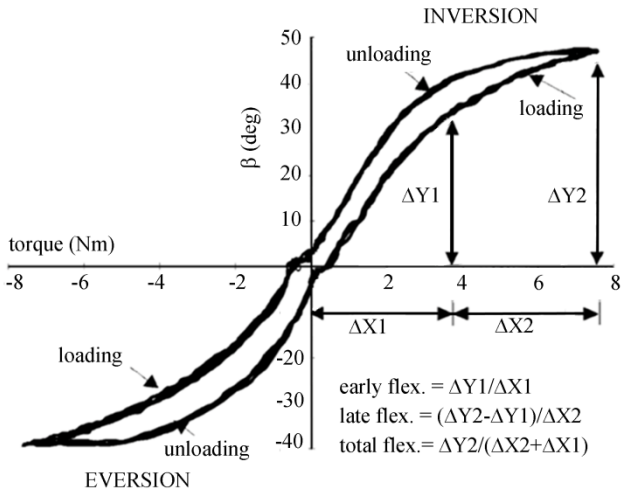

Figure 2.31. Representation of the evaluation of the early, late and total flexibility (Laiponte et al. 1997)

As reported in Figure 2.31, the early flexibility was calculated as the ratio between the displacement and the change in load for the 0-50% region. Late flexibility was defined as the ratio between the displacement and the applied load for the 50-100% region, while total flexibility was evaluated as the ratio between the displacement and the applied load for the entire 0-100% loading range. These experimental results are reported in table 2.5.

The experimental data allow us to evaluate the influence of the anterior talofibular and calcaneofibular ligament on the flexibility of the ankle joint.

	ATFL ligament cut vs intact limb		double cut vs intact limb		double cut vs ATFL ligament cut	
	% difference	P value	% difference	P value	% difference	P value
anterior drawer						
early flexibility	109	0.006	141	0.0014	15	n/s
total flexibility	60	0.0003	74	0.0001	9	n/s
inversion						
early flexibility	13	n/s	86	0.003	64	0.001
total flexibility	7	n/s	57	0.0001	47	0.0001
eversion						
early flexibility	11	n/s	5	0.003	13	n/s
total flexibility	6	n/s	15	0.0122	8	n/s
coupling						
early flexibility	59	n/s	190	0.000	83	0.0074
total flexibility	21	n/s	93	0.0153	89	0.0473
internal rotation						
early flexibility	12	n/s	8	n/s	19	n/s
total flexibility	2	n/s	6	n/s	4	n/s
external rotation						
early flexibility	14	n/s	24	0.0127	9	0.0398
total flexibility	8	n/s	29	0.0015		0.0015

Table 2.5. Average percentage difference in flexibility between the three different testing conditions (Laiponte et al. 1997)

As shown in Figure 2.30 and table 2.5 isolated sectioning of the anterior talofibular ligament produced a large increase in anterior drawer flexibility (greater than 60%), without a significant increase in inversion flexibility. Subsequent sectioning of the calcaneofibular ligament, resulting in damage to both ligaments, produced large significant changes in inversion flexibility (57% increase), as well as a further increase in anterior drawer flexibility. Isolated damage to the anterior talofibular ligament did not significantly affect coupling between internal rotation and inversion and between external rotation and eversion. However, when both ligaments were sectioned, coupling significantly increased relative to both the intact condition and the condition in which only the anterior talofibular ligament is ruptured.

2.5 References

Attarian D.E, McCrackin H.J., DeVito D.P., McElhaney J.H., Garrett W.E., 1985a. Biomechanical characteristis of human ankle ligaments, Foot & Ankle, vol. 6(2), pp. 54-58.

Attarian D.E, McCrackin H.J., DeVito D.P., McElhaney J.H., Garrett W.E., 1985b. A biomechanical study of human lateral ankle ligaments and autogenous reconstructive grafts, The American Journal of Sports and Medicine, vol. 13(6), pp. 377-381.

Bahr R., pena F., Shine J., Lew WD., Engebretaen L., 1998. Ligament force and joint motion in the intact ankle: a cadaveric study. Knee Surgery, Sports Traumatology, Arthroscopy, vol. 8(2), pp. 115-121.

Bonifasi-Lista C., Lake S.P., Small M.S., Weiss J.A., 2005. Viscoelastic properties of the human medial collateral ligament under longitudinal, transverse and shear loading, Journal of Orthopaedic Research, vol. 23, pp. 67–76.

Colville MR., Marder RA., Boyle JJ., Zarins B., 1990. Strain measurement in lateral ankle ligaments, American Journal of Sports and Medicine, vol. 12(2), pp. 196-200.

Cusack S. and Miller A., 1979. Determination of the elastic constants of collagen by Brillouin light scattering, Journal of Molecular Biology, vol. 135, pp. 39-51.

Dean D., Han L., Grodzinsky A.J., Ortiz C., 2006. Compressive nanomechanics of opposing aggrecan macromolecules, Journal of Biomechanics, vol. 39, pp. 2555-2565.

Eisenberg S.R., Grodzinsky A.J., 1985. Swelling of articular cartilage and other connective tissues: electromechanical forces, Journal of Orthopaedic Research, vol. 3, pp. 148-159.

Eyre D.R., Pietka T., Weis M.A., Wu J.J., 2004. Covalent cross-linking of the NC1 domain of collagen type IX to collagen type II in cartilage, The Journal of Biological Chemistry, vol. 279, pp. 2568-2574.

Frank C.B., Shrive N.G., 1999. Biological materials, In Biomechanics of the musculo-skeletal system, Chichester, New York, pp. 107-126.

Freed A.D., Doehring T.C., 2005. Elastic model for crimped collagen fibrils, Journal of Biomechanical Engineering, vol. 127, pp. 587-593.

Fung Y.C., 1993. Biomechanics: mechanical properties of living tissues (second edition), Springer-Verlag, New York.

Funk J.R., Hall G.W., Crandall J.R., Pilkey W.D, 2000. Linear and quasi linear viscoelastic characterization of ankle ligaments, Journal of Biomechanical Engineering, vol. 122, pp. 15-22.

Gautieri A., Vesentini S., Redaelli A., Buehler M.J., 2011. Hierarchical structure and nanomechanics of collagen microfibrils from the atomistic scale up, Nano Letters, vol. 11 (2), pp 757–766.

Hofmann H., Voss T., Kuhn K., Engel J., 1983. Localization of flexible sites in thread-like molecules from electron micrograph – Comparison of interstitial, basement and intima collagen, Journal of Molecular Biology, vol. 172, pp. 325-343.

Kadler K.E., Holmes D.F., Trotter J.A., Chapman J.A., 1996. Collagen fibril formation, Biochemical Journal, vol. 316, pp. 1-11.

Keller K., Nasrilari M., Filler T., Jerosch J., 2010. The anterior tibio-talar ligament: one reason for anterior ankle impingement, Knee Surgery, Sports Traumatology, Arthroscopy, vol. 18, pp. 225–232.

Kumai T., Takakura Y., Rufai A., Milz S., Benjamin M., 2002. The functional anatomy of the human anterior talofibular ligament in relation to ankle sprains, Journal of Anatomy, vol. 200, pp. 457-465.

Lapointe S.J., Siegler S., Hillstrom H., Nobilini R.R., Mlodzienski A., Techner L., 1997. Changes in the flexibility characteristics of the ankle complex due to damage to the lateral collateral ligaments: an in vitro and in vivo study, Journal of Orthopedic Research, vol. 15, pp. 331-341.

Limbert G., Taylor M., 2002. On the constitutive modelling of biological soft connective tissues. A general theoretical framework and explicit forms of the tensors of elasticity for strongly anisotropic continuum fiber-reinforced composites at finite strain, International Journal of Solids and Structures, vol. 39, pp. 2343-2358.

Loret B., Simoes F.M.F., 2004. Articular cartilage with intra- and extrafibrillar waters : a chemo-mechanical model, Mechanics of Materials, vol. 36, pp. 515-541.

Minns R.J., Soden P.D., Jackson D.S., 1973. The role of the fibrous components and ground substance in the mechanical properties of biological tissues: a preliminary investigation, Journal of Biomechanics, vol. 6, pp. 153-165.

Natali A.N., Pavan P.G., Carniel E.L., 2004b. Damage phenomena in anisotropic soft biological tissues: a constitutive formulation, Russian Journal of Biomechanics, vol. 8, pp. 43-60.

Natali A.N., Pavan P.G., Carniel E.L., Dorow C., 2004a. Visco-elastic response of the periodontal ligament: an experimental-numerical approach, Journal of Connective Tissue Research, vol. 45, pp. 222-230.

Natali A.N., Pavan P.G., Carniel E.L., Lucisano M.E., Taglialavoro G., 2005. Anisotropic elasto-damage constitutive model for the biomechanical analysis of tendons, Medical Engineering and Physics, vol. 27, pp. 209-214.

Nestler F.H.M., Hvidt S., Ferry J.D., 1983. Flexibility of collagen determined from dilute solution viscoelastic measurements, Biopolymers, vol. 22, pp. 1747-1758.

Nigg BM., Skarvan G., Frank CB., Yeadon MR., 1990. Elongation and forces of ankle ligaments in a physiological range of motion, Foot & Ankle, vol. 11, pp. 30-40.

Nishihira M., Yamamoto K., Sato Y., Ishikawa H. Natali A.N., 2003. Mechanics of periodontal ligament. In Natali A.N. (editor), Dental biomechanics, Taylor & Francis, London, pp. 20-34.

Nishimura M., Yan W., Mukudai Y., Nakamura S., Nakamasu K., Kawata M., Kawamoto T., Noshiro M., Hamada T., Kato Y., 1998. Role of chondroitin sulphate-hyluronan interactions in the viscoelastic properties of extracellular matrices and fluids, Biochimica et Biophysica Acta, vol. 1380, pp. 1-9.

Ottani V., Martini D., Franchi M., Ruggeri A., Raspanti M., 2002. Hierarchical structures in fibrillar collagens, Micron, vol. 33, pp. 587-596.

Ozeki S., Yasuda K., Kaneda K., Yamakoshi K., Takahiro Y., 2002. Simultaneous strain measurement with determination of a zero strain reference for the medial and lateral ligaments of the ankle, Foot & Ankle International, vol. 23(9), pp. 825-832.

Pavan P.G., Stecco C., Darwish S., Natali A.N., De Caro R., 2011. Investigation of the mechanical properties of the plantar aponeurosis, Surgical and Radiologic Anatomy , vol. 33, pp. 905–911.

Petruska J.A., Hodge A.J., 1963. Recent studies with the electron microscope on ordered aggregates of the tropocollagen molecule. In Ramachandran G.N. (editor), Aspects of protein structure, Academic Press, New York, pp. 289-300.

Price P.A., Toroian D., Lim J.E., 2009. Mineralization by inhibitor exclusion: the calcification of collagen with fetuin. The Journal of Biological Chemistry, vol. 284 (25), pp 17092–17101.

Raspanti M., Alessandrini A., Ottani V., Ruggeri A., 1997. Direct visualization of collagen-bound proteoglycans by tapping-mode atomic force microscopy, Journal of Structural Biology, vol. 119, pp. 118-122.

Redaelli A., Vesentini S., Soncini M., Vena P., Mantero S., Montevecchi F.M., 2003. Possible role of decorin glycosaminoglycans in fibril to fibril force transfer in relative mature tendons – a computational study from molecular to microstructural level, Journal of Biomechanics, vol. 36, pp. 1555-1569.

Reese S.P., Maas S.A., Weiss J.A., 2010. Micromechanical models of helical superstructures in ligament and tendon fibers predict large Poisson's ratios, Journal of Biomechanics, vol. 43(7), pp.1396-1400.

Renstrom P., Wertz M., Incavo S., Pope M., Ostgaard HC., Arms S., Haugh L., 1988. Strain in the lateral ligaments of the ankle, Foot & Ankle, vol. 9, pp. 59-63.

Sasaki N., Odajima S., 1996. Stress-strain curve and Young's modulus of a collagen molecule as determined by the X-ray diffraction technique, Journal of Biomechanics, vol. 29, pp. 655-658.

Siegler S., Block J., Schneck C.D., 1988. The mechanical characteristics of the collateral ligaments of the human ankle joint, Foot & Ankle, vol. 8(5), pp. 234-242.

Silver F.H., Freeman J.W., Seehra G.P., 2003. Collagen self-assembly and the development of tendon mechanical properties, Journal of Biomechanics, vol. 36, pp. 1529-1553.

Solomonow M., 2009. Ligaments: A source of musculoskeletal disorders, Journal of Bodywork and Movement Therapiee, vol. 13, pp. 136–154.

Solomonow M., Baratta R.V., Zhou B., Burger E., ZieskeA., Gedalia A., 2003. Muscular dysfunction elicited by creep of lumbar viscoelastic tissues, Journal of Electromyography and Kinesiology vol. 13, pp.381–396.

Szwajczak E., 2004. Dependence of hyaluronan aqueous solution viscosity on external fields. Part II, Russian Journal of Biomechanics, vol. 8, pp. 89-94.

Weiss J.A., Gardiner J.C., 2001. Computational modeling of ligament mechanics, Critical reviews in Biomedical Engineering, vol. 29(4), pp.1-70.

Yang L., 2008. Mechanical properties of collagen fibrils and elastic fibers explored by AFM, PhD Thesis, University of Twente, Enschede, The Netherlands.

CHAPTER 3

DEFINITION OF THE NUMERICAL MODEL OF THE FOOT: VIRTUAL SOLID MODEL AND CONSTITUTIVE FORMULATIONS

3.1 Introduction

Numerical modelling approach based on the finite element method is a robust tool to improve the knowledge of foot biomechanics for integration and reciprocal validation of the experimental data, also evaluating the mechanical behaviour of the foot tissues.

The complex mechanical behaviour of the foot implies an adequate modelling in terms of 3D morphometric characteristics and constitutive modelling.

To this purpose a solid model of the foot is developed. The model consists of 30 bony segments, including the distal segments of the tibia and fibula and the 28 foot bones. The model of the bones and of the skin of the foot is obtained starting from the elaboration of computer tomography and magnetic resonance images, respectively. The ligaments of the hindfoot are, instead, developed starting from the anatomical data present in literature. To define the solid models of the ligaments morphometric aspects have to be considered: length, width, thickness, cross sectional area within the full extension of the ligament and geometry of the entheses. These features are fundamental to understand the biomechanical response of the ligaments.

The numerical model of the foot is obtained from the solid model through a specific software. With regard to the constitutive modelling, for the analysis of the mechanical behaviour of the ligaments of the hindfoot a fiber-reinforced visco-hyperelastic constitutive model is proposed.

3.2 Investigation of the numerical models of the foot reported in literature

A numerical modeling approach based on the finite element method is a robust tool to deepen the knowledge of foot biomechanics for the integration and reciprocal validation of the experimental data, also evaluating the local interaction phenomena between the foot and insole and, more in detail, the mechanical behaviour of the foot tissues. The purpose of obtaining refined models of the foot is recognized as a mandatory aspect and can be found in several works already present in the literature. Computational modeling, such as the finite element method, has been used increasingly in many biomechanical investigations with great success. This is due to its capacity to model structures with irregular geometry and complex material properties, and also to the ease of simulating complicated boundary and loading conditions in both static and dynamic analyses.

The numerical models of the foot present in the literature have been developed under certain simplifications and assumptions concerning morphological configuration, the mechanical properties of tissues, and loading and boundary conditions.

Regarding the morphological configuration the phalanges are often fused together (Gefen et al. 2000), the ligaments and plantar fascia are modelled with tension only truss element (Wang et al. 2009; Yu et al. 2008; Cheung et al. 2007; 2005) without considering the real geometry of the foot ligaments. Nonetheless, a fundamental problem arises in connection with the definition of the constitutive formulation of the foot tissues. There are many works that have reported numerical models of the foot, even if none of them describe the actual mechanical properties of the foot tissues. Several works, for example, described the ligaments such as tension only truss element with linearly elastic properties (Wang et al. 2009; Yu et al. 2008; Cheung et al. 2007; 2005) even if the experimental tests show a non-linearity and time dependent mechanical behaviour.

To this purpose, the aim of this chapter is describe a procedure that leads to a definition of a numerical model of the foot, and specifically of the hindfoot. The model respects the actual geometry of each component of the structure and describes the property of the tissues with a specific constitutive formulation.

3.3 Development of virtual solid model of the foot

The definition of a finite element model of the foot starting with the elaboration of the DICOM images generated by x-ray computed tomography (CT) and magnetic resonance imaging (MRI). The DICOM images are processed with a medical imaging and editing software that is used to obtain the primary 3D models (triangulate model) using a density segmentation technique. The generated primary 3D models are exported as geometrical files for a CAD system (UGS NX3, UGS Corporate, Plano, TX) that allows the assembly and some 3D geometrical operations. Finally, the virtual solid models described above are exported in parasolid format to be discretized in finite element models by a specific software (Patran, MSC.Software Corporation, Santa Ana, CA). The procedure adopted is a guideline that does not impose standards or processing parameters set for all cases. Each model is defined by subjective evaluations and reaches a good compromise between an acceptable level of accuracy and regular surfaces (De Souza, 2007; Korioth and Versluis, 1997; Vannier et al. 1997).

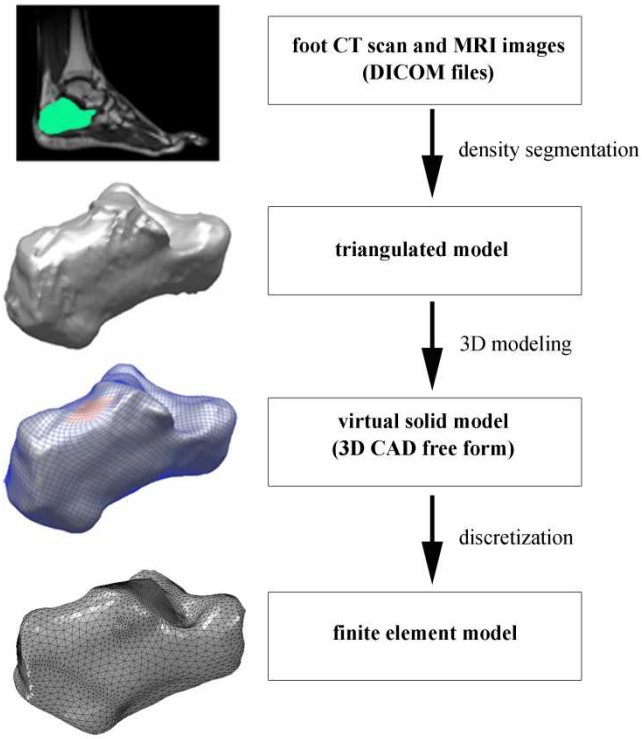

Figure 3.1. Modelling methodology

3.3.1. Selection and analysis of biomedical images

Medical imaging is a branch of the medical field which involves the use of technology to take images of the inside of the human body in a way that is as non-invasive as possible. These images are used in diagnostics and in routine healthcare for a variety of conditions. There are a number of different types of technology used in medical imaging, however some of the most famous types are the x-ray, the CT and the MRI (Ayache 1995; Stytz et al. 1991).

The reconstruction of the virtual solid models of the foot requires the acquisition of images from CT or MRI. Specifically, the reconstruction of the skeletal structure of the foot is obtained by acquiring and processing CT images (Figure 3.2 a), in which the bone tissues are highly distinct from other tissues. While the reconstruction of the soft tissues requires the elaboration of MRI images (Figure 3.2 b), that make it possible to distinguish the different soft tissues of the foot with different grey levels (Matteoli et al. 2010; Reach et al. 2007; Rosenberg et al., 2000).

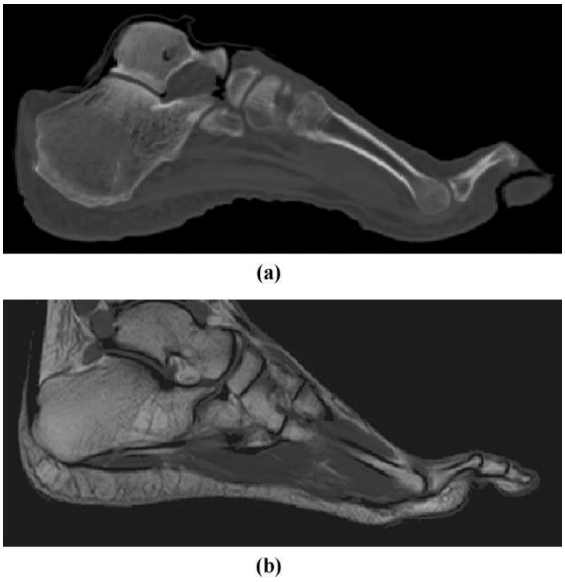

Figure 3.2. CT (a) and MRI (b) image of the foot

The sequence of collecting tomography scans and the magnetic resonance imaging of the patient is available in files sorted by type DICOM (Digital Imaging and Communications in Medicine), a standard communication protocol created by the National Electrical Manufacturers Association (NEMA). The DICOM standard has

been introduced to define a mode of communication, storage and management of medical information, with particular regard to biomedical images.

The reconstruction of the primary 3D anatomical structures is obtained by the use of a medical imaging density segmentation software. The DICOM image files generated in the CT and MRI are constituted by pixels with different grey intensities. The different intensity fields correspond to different material densities presented in the anatomical structures (Antunes et al. 2010).

The reconstruction of the virtual solid model of the bones of the foot is obtained from the direct analysis of tomographic slices generated by the lower limb. Initially, it is necessary to impose the proper axial orientation to imported images. Then the main screen appears (Figure 3.3), which is divided into two parts. The left side has four panels, representing the frontal, transverse and sagittal plane and one additional space for the subsequent viewing of the 3D solid model of the selected structure in 3D. The right side is the Project Management where a list of all the objects created is reported, which can be viewed or modified (Figure 3.3).

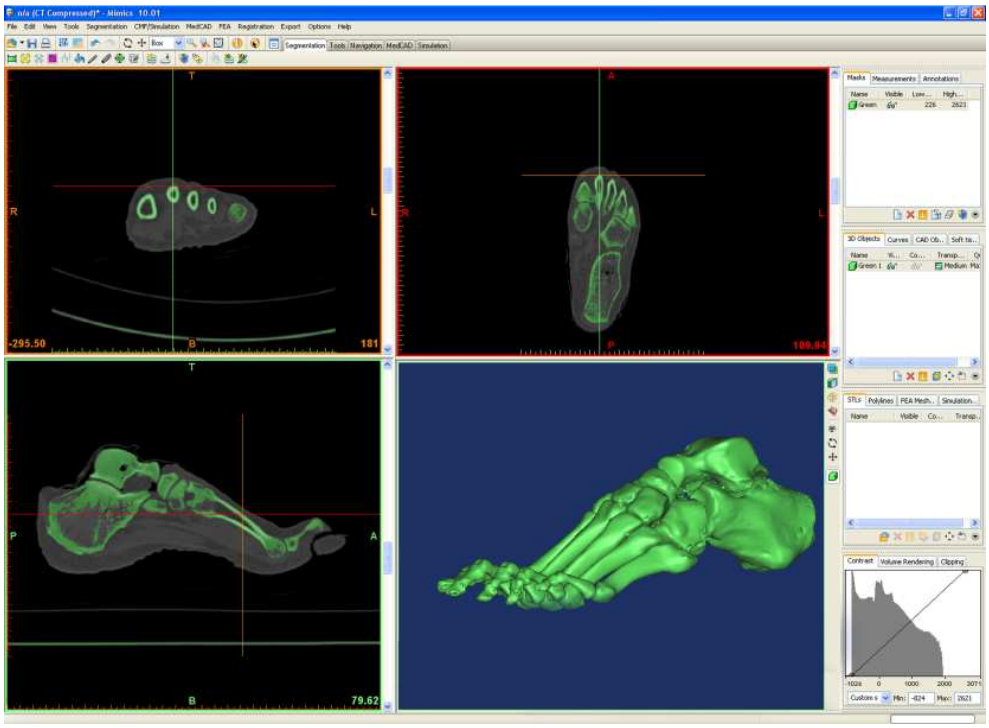

Figure 3.3. Reconstruction of the bones from TAC images

To distinguish and highlight the bone tissues, the procedure used a threshold method. The program sets the default interval of grey levels in the Hounsfield scale for the selection of different tissues from CT images. In particular, the bone tissue of an adult has grey levels between 226 and 3071 of the Hounsfield scale. In order to obtain a reliable selection of bone components, subsequent operations are necessary. The Project Management enables us to create the virtual solid model of the selected tissue, as an enclosed volume delimited by a 2D triangular mesh (De Souza 2007). During this operation, it is possible to choose the accuracy and the level of image quality to be implemented.

With regard to the soft tissue the same procedure is adopted on the MRI image. The adipose tissue, the skin and the Achilles tendon is the soft tissue that is possible to obtain by means of MRI images. An example is reported for the Achilles tendon (Figure 3.4).

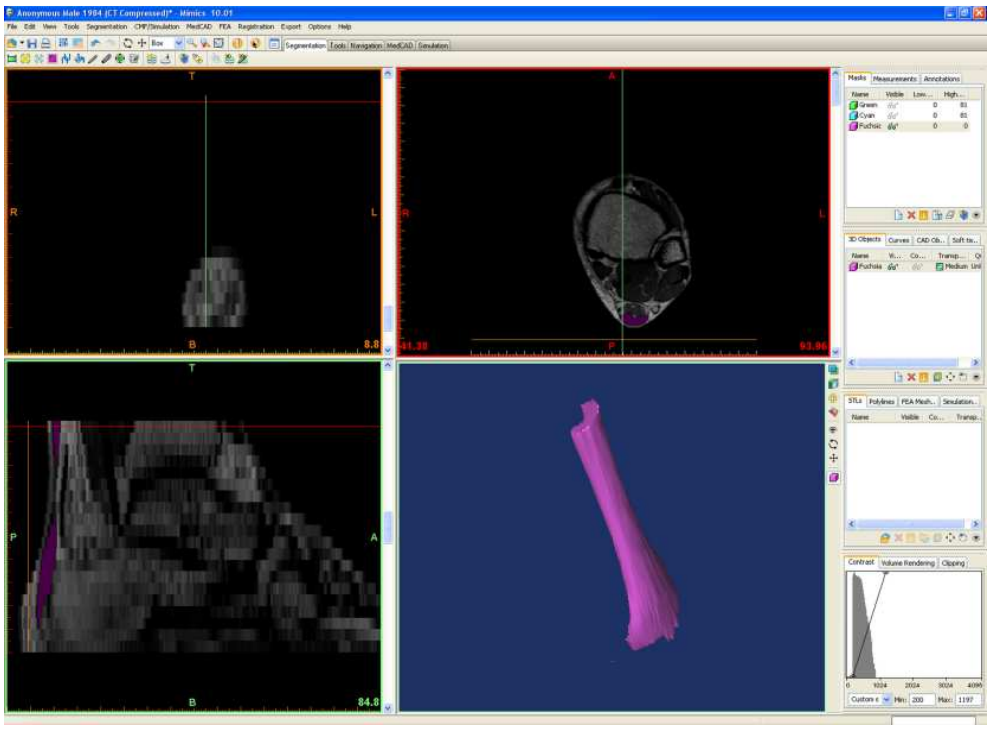

Figure 3.4. Reconstruction of the Achilles tendon from MRI images

To elaborate the virtual solid models obtained with Mimics, they must be saved in .STL format to guarantee the subsequent importation into the processing software.

3.3.2. Elaboration of triangulated models

The files in .STL format are imported by the modelling software, where a shell is registered in the project window (Figure 3.5). The shell is defined as an enclosed volume delimited by 2D triangular elements, usually related to each other, which form a polygon mesh. Working with a mesh is advantageous because of the speed of processing and the multiple control functions. The disadvantages are related to the approximation with which the surfaces are represented, which are formed by small triangles.

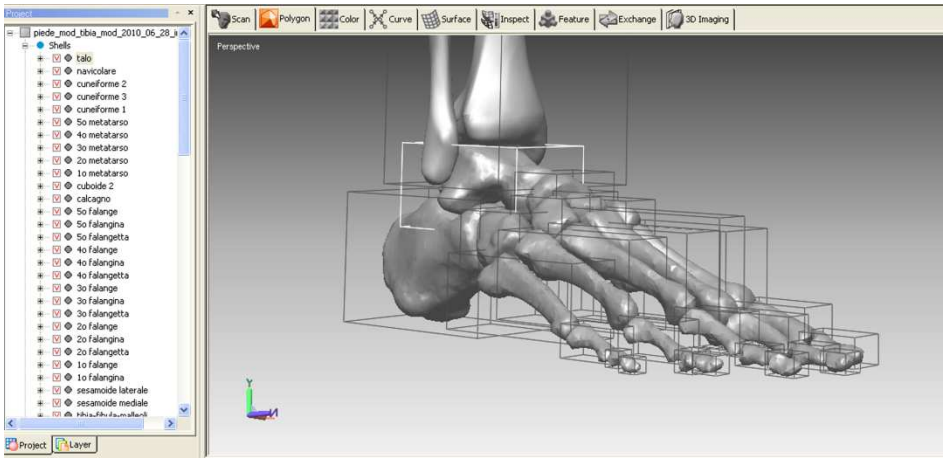

Figure 3.5. Representation of bones conformation

In order to obtain a virtual solid model which describes the real configuration of the biological structures, the elaboration of the primitive model are intended to define the shape of the structure as smoothly and clean-cut as possible. At the same time, the purpose is to identify the actual geometry of the structure without omitting details, even if some approximations during the procedure are inevitable.

With the process of segmentation previously described, the virtual solid model obtained is characterized by an irregular surface, with gaps, scattering and in some cases a constant trend in steps due to the stratification of the medical images. The software makes it possible to select, by specific commands, the regions of the entire shell which present the major defects and must be corrected.

For this purpose, the first step involves the regularization of the surface, starting from the operation of smoothing that solves the most minor defects, while maintaining the overall shape. This operation can be divided in global and local smooth and it is

possible to set the method of intervention (laplacian, loops or bends), the weight and the number of passes. The defects of the surface often cannot be resolved completely, taking into account only smoothing. The software offers several tools that are used in these cases, usually applied to small regions with the aim of not deforming the overall surface. The surfaces that present error and discontinuity can be selected, deleted and replaced with a regular shape which follows the trend of the surrounding region. For this purpose it is possible to reconstruct and close the cavities created during the segmentation procedure. This operation can be done with one hole or with all holes together and enable closing with a flat, smooth or curved shape. It is also possible to create links between the contours of a large cavity, so as to reduce the extension to two smaller gaps and allow the next stage of closing to follow a precise pattern of the form.

When is necessary deform an area, the software allows to deform and transform the shell obtained. For example it is possible to create a reticule around the selected section of the shell and to execute the deformation by moving the balls placed at the top and along the sides of the reticule.

An example of surface elaboration is reported for the calcaneus bone (Figure 3.6).

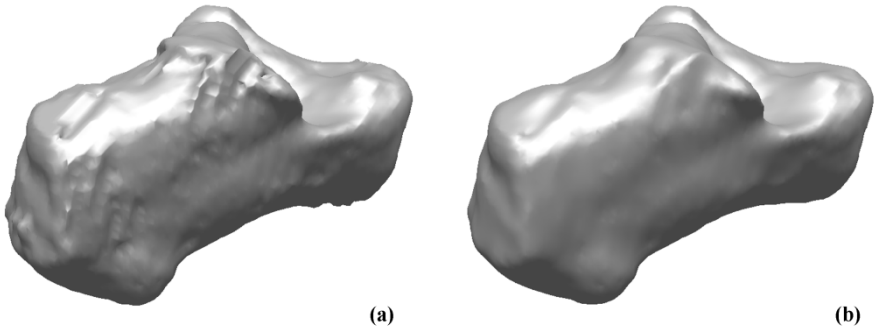

Figure 3.6. Triangulated model of calcaneus before (a) and after (b) the operation of modelling

The software offers also the possibility to re-triangulate the overall surface, transforming all triangles into equilateral triangles.

3.3.3. Definition of virtual solid models of the bones and skin

From the description of rough tessellated geometry an exact mathematical model is then obtained (Antunes et al. 2010).

The mathematical representation is called NURBS (Non-Uniform Rational B-Splines). The NURBS curves are polynomial curves that come close to the boundaries of free-form. The NURBS curves have the advantage of representing arbitrary shapes with mathematical precision, while maintaining control over the shape of the curves through their nodes and control points, which can be directly manipulated. The procedure uses a fitting algorithm, which consists of a series of patches that fit the discrete data, such as point cloud formed by the vertices of all triangles. The patches are usually of the same mathematical nature and are linked together by the conditions of tangency or curvature.

The software allows to obtain a mathematical surface directly from the tessellated surface (Figure 3.7). Before starting the automatic surfacing, it is possible to set some parameters such as the total number of surfaces that you want to create and the number of control points of the surface. Finally, it is useful to enforce certain conditions of the process: the generation of a uniform surface, the adhesion of the created patches to the original surface, removal of the roughness and the possibility of changing the boundaries of the patch after the execution. With a higher number of chosen areas, the resulting model is clearly more accurate. This operation is limited only by the computational capacity of computers, which can take a long time to achieve.

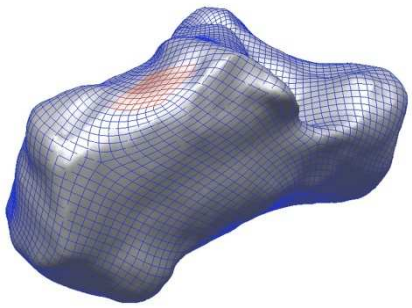

Figure 3.7. Triangulated model (grey solid) and CAD model free form (blue and red lines) of calcaneus

To share the geometries with the software Unigraphics (UGS NX3, UGS Corporate, Plano, TX) all the surfaces must be exported as an IGES (Initial Graphics Exchange Specification) file. This operation increases the degree of approximation of mathematical models of the surfaces. In reference to solid models developed, it is

necessary to make changes to portions of the surface that the previous methods has not been able to achieve correctly. With the modelling package, the freeform surfaces created can be modified and corrected.

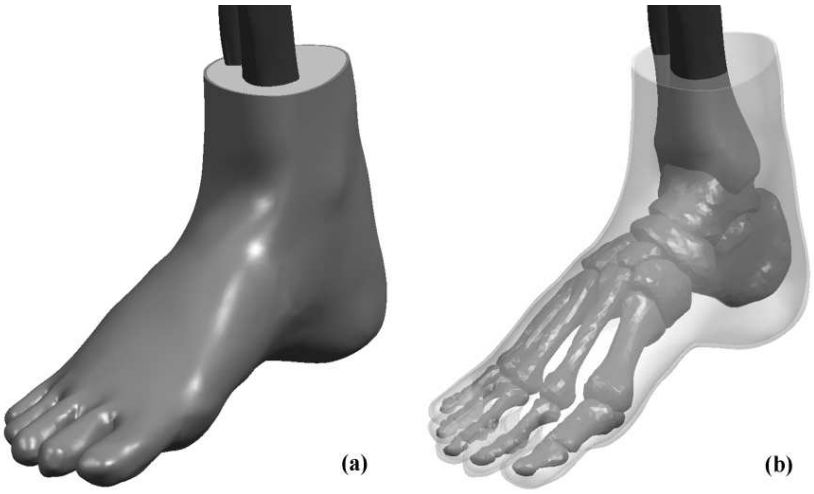

Figure 3.8. CAD model free form of the foot: soft tissues and bone structures

3.3.4. Definition of virtual solid models of the ankle ligaments

The MRI or TAC images processing does not allow the reconstruction of the ligaments geometry. To overcome this problem a careful analysis of the morphometric data present in the literature is performed. On the basis of morphometric information, ligaments are defined through the Unigraphics software. In detail, first, it is necessary to understand the point of insertion of each ligament and the dimension of their entheses. Second, to define a solid model, it is important to have the dimension of the ligament such as length, width, thickness and cross sectional area within the full extension of the ligament itself.

The lateral collateral ligaments (as reported in Chapter 1) are composed of three ligaments: the anterior talofibular ligament (ATFL), the calcaneofibular ligament (CFL) and the posterior talofibular ligaments (PTFL). The ATFL originates at the anterior margin of the lateral malleolus and ends in the talar attachment, anterior to the fibular articular surface (Muhle et al. 1999). The average area of attachment is 8.2 mm in the sagittal dimension and 5.4 mm in the coronal plane (Van Den Bekeron et al. 2008). The CFL is located just below the lower band of the ATFL and it runs downwards and backwards to be attached to the lateral posterior surface of the

calcaneus on a small tubercle. The insertion averages 8.2 mm in the sagittal direction and 6.2 in the coronal direction. With regard to the PTFL, the fibular attachment is centred an average 9-7 mm proximal to the distal tip in the malleolar fossa. The PTFL has a long attachment on the posterior portion of the talus measuring 24.1 mm by 6 mm. The other morphometric characteristics of the collateral lateral ligaments of the ankle are reported in the following table.

	Length (mm)	**Width (mm)**	**Thickness (mm)**	**Cross Sectional Area (mm^2)**	**Author**
ATFL	18.89 ± 2.97			62.85 ± 21.92	Mkandawire et al.
	15-20	6-8	2		Mangwani et al.
	17.81 ± 3.05			12.9 ±7.7	Siegler et al.
	13.0 ± 3.9	11.0 ± 3.3			Milner and Soames
	24.8	7.2			Burks and Morgan
		11.1 ± 2.0	1.8 ± 0.6		Butler et al.
	15-20	6-10	2		Van Den Bekerom et al.
	10.5 ± 0.6	7.6 ± 0.4			Attarian et al.
CFL	35.44 ± 6.31			21.36 ± 7.06	Mkandawire et al.
	20-30	4-8	3-5		Mangwani et al.
	27.69 ± 3.3			9.7 ±6.5	Siegler et al.
	19.5 ± 3.9	5.5 ± 1.6			Milner and Soames
	35.8	5.3			Burks and Morgan
		10.5 ± 2.3	1.5 ± 0.2		Butler et al.
	20	4-5.5	4-8		Van Den Bekerom et al.
	17.5 ± 0.7	6.8 ± 0.4			Attarian et al.
PTFL	27.74 ± 3.41			46.43 ± 21.33	Mkandawire et al.
	30	5	5-8		Mangwani et al.
	21.16 ± 3.86			21.9 ± 18.1	Siegler et al.
	23.0 ± 7.0	5.5 ± 2.5			Milner and Soames
	24.1				Burks and Morgan
		13.0 ± 3.1	2.3 ± 0.6		Butler et al.
	30	5	5-8		Van Den Bekerom et al.
	15.3 ± 0.9	7.8 ± 0.4			Attarian et al.

Table 3.1. Morphometric characteristics of collateral lateral ankle ligaments

With regard to the deltoid ligament three components are considered: the anterior tibiotalar ligament (ATTL), the tibio calcaneal ligament (TCL) and the posterior tibiotalar ligament (PTTL). The insertions of the deltoid ligaments have a very complicated shape. Boss et al. (2002) reported the approximated value of the

insertion area: the proximal and distal insertion area of the ATTL are equal to 14.8 ± 14.5 mm^2 and 25 ± 25.8 mm^2, respectively while the TCL has a proximal insertion area of 17.1 ± 9.4 mm^2 and a distal insertion area of 19.8 ± 10.9 mm^2. The last of the deltoid ligament group present the major insertion area: 24.3 ± 21.9 mm^2 is the value of the proximal insertion while 38.8 ± 38.7 mm^2 is the distal area.

	Length (mm)	Width (mm)	Thickness (mm)	Cross Sectional Area (mm^2)	Author
PTTL	26.68 ± 4.49			78.43 ± 39.59	Mkandawire et al.
	16.6 ± 3.7		2.9 ± 1.1		Butler et al.
	11.86 ± 3.96			45.20 ± 31.60	Siegler et al.
	16.8 ± 5.6		1.6 ± 0.6		Boss et al.
TCL	37.45 ± 2.74			43.20 ± 28.57	Mkandawire et al.
	19.7 ± 3.2		2.8 ± 0.6		Butler et al.
	25.6 ± 4.5		1.8 ± 1.5		Boss et al.
ATTL	24.09 ± 8.03			43.49 ± 19.92	Mkandawire et al.
	16.7 ± 3.7		2.5 ± 0.8		Butler et al.
	5.1 ± 0.1	23.5 ± 0.8			Attarian et al.
	16.1 ± 6.8		1.2 ± 0.7		Boss et al.

Table 3.2. Morphometric characteristics of the medial ankle ligaments

The properties of the tibio fibular and subtalar ligaments have received less attention than the ligament described above. The morphometric information that are presented in literature are reported in the following two tables.

	Length (mm)	Width (mm)	Thickness (mm)	Cross Sectional Area (mm^2)	Author
ATiFL		16.3 ± 5.9	1.8 ± 0.4		Butler et al.
PTiFL		18.3 ± 2.	2.7 ± 0.8		Butler et al.

Table 3.3. Morphometric characteristics of the tibio-fibular ligaments

	Length (mm)	Width (mm)	Thickness (mm)	Cross Sectional Area (mm^2)	Author
ITCL	4.06 - 9.55 (in vivo)			54.92 (in vivo)	Imhauser
	5.51 – 19-39 (in vitro)			90.69 (in vitro)	

Table 3.4. Morphometric characteristics of the interosseous talocalcaneal ligament

The geometry of each ligament is defined in order to respect the range of measure reported in literature, additional information are defined by means of the collaboration with the Department of Anatomy and Physiology of Padua.

Starting from morphometric information the soild model of each ligament is defined through Unigraphics. The geometry of the ligament is obtained by means of splines drawn considering the measure of insertion area, length, width and thickness of the central region of ligament itself. The software allows to build the surfaces of the structure starting from splines that are previously defined. In order to create a solid model of each ligament all the surfaces are joined with a specific procedure.

In Figure 3.9 is reported a schematic representation of the steps required by the procedure adopted to define the ligament geometry.

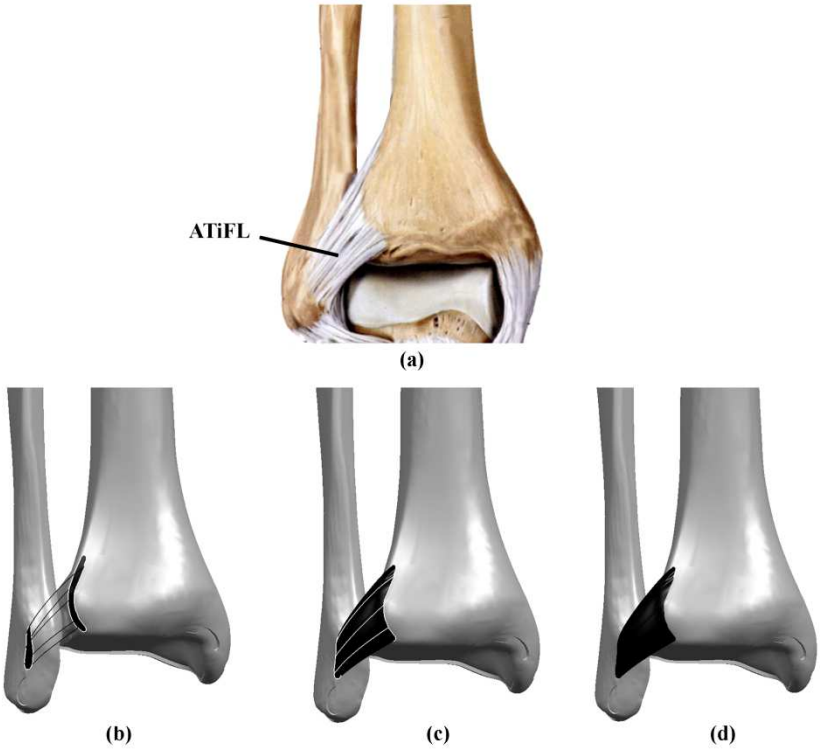

Figure 3.9. Definition of the ATiFL geometry: actual geometry (a), definition of the insertion area and of the splines that delimit the central region of the ligament (b), definition of the surface (c) and creation of the solid body that represents the ATiFL ligament (d)

The solid model of the ankle ligaments is reported in Figure 3.10 while the solid model of the subtalar joint is reported in Figure 3.11.

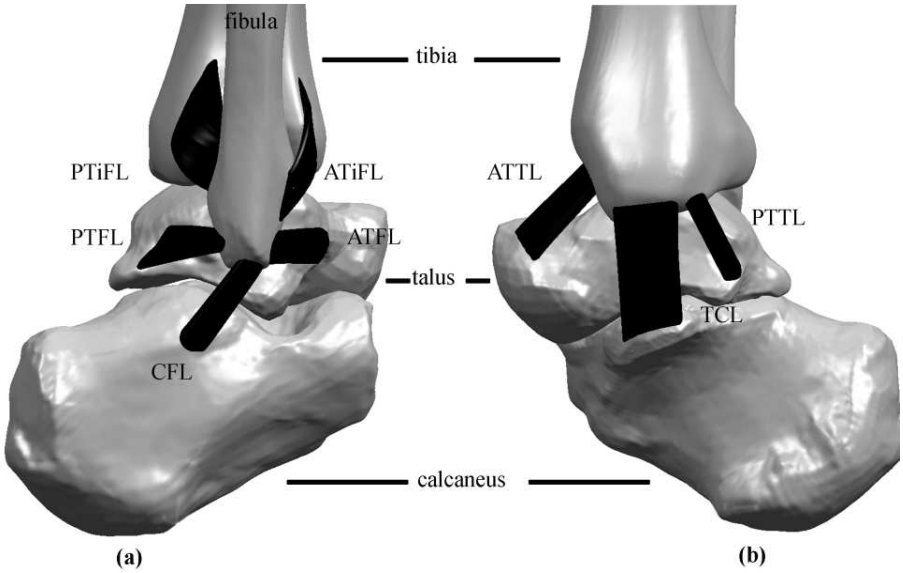

Figure 3.10. Virtual solid model of the ankle ligaments: lateral (a) and medial (b) view

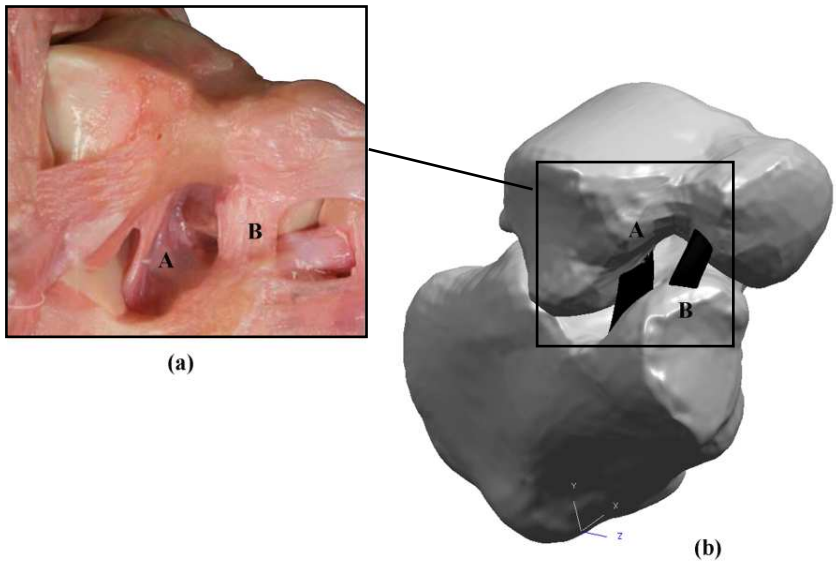

Figure 3.11. The ligament of the subtalar joint: actual morphometry (a) and solid model (b) of the talocalcaneal interosseus ligament (A) and cervical ligament (B)

Solid models of the different components (bones, skin, soft tissue, ligaments and tendon) are exported in parasolid format to be discretized in finite element models.

3.4 Definition of the numerical model of the foot from virtual solid model

The definition of the numerical model of the foot is performed by the finite element discretization of the virtual solid models described previously. The discretization of

the solid model is done using a specific software (Patran, MSC.Software Corporation, Santa Ana, CA).

In order to obtain a numerical model with a proper and accurate discretization, it is necessary, first of all, to proceed with the discretization of the surfaces of the virtual solid models with triangular elements.

These elements are defined by three nodes, with side length of about 2 mm. With this procedure the 2D mesh of all solid models is obtained. After this operation, the area of interaction between the models is modified to make them congruent. This operation is achieved by removing some triangular finite elements and defining new ones.

On obtaining the different numerical models which are consistent with each others, it is necessary to define the 3D (Figure 3.12) mesh using tetrahedral elements.

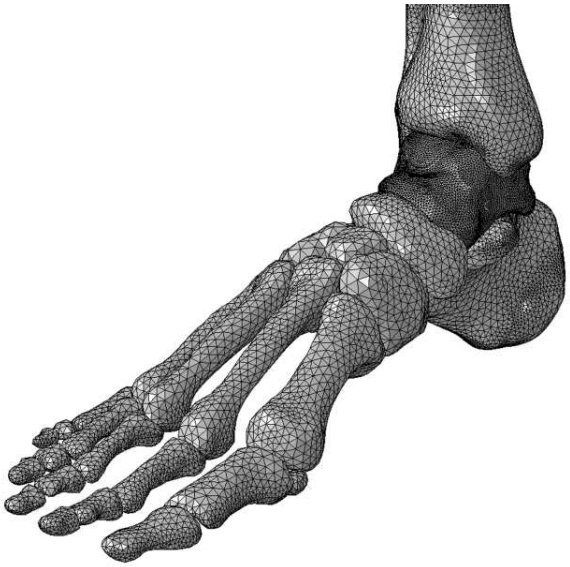

Figure 3.12. Finite element model of the bone structures

It is important to notice that in relation to the presence of ligaments entheses and cartilage layers, the mesh density of bone components differs. The different mesh density is necessary to ensure a good approximation of the elements in contact and to observe the morphometry of each element.

A detail of the numerical model of the hindfoot ligaments is reported in Figure 3.13.

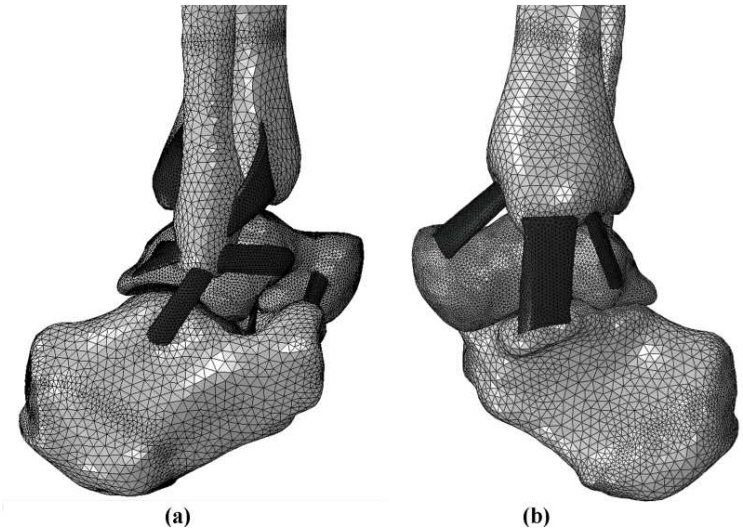

Figure 3.13. Finite element model of the ankle joint: (a) lateral and (b) medial view

3.5 Constitutive modelling of ankle ligaments

Soft biological tissues are usually composed of fibrous elements (such as collagen or muscle fibers) embedded in an isotropic and almost incompressible ground matrix and, from a mechanical point of view, can be considered as composite materials. The local distribution of fibers determines the material symmetry characteristics (Spencer 1992). The structural conformation rearrangements developing within the material when external loads are applied demonstrate a strongly non-linear behaviour (Natali et al. 2005). In a first approach to the problem, non-linear behaviour can be analysed by hyperelastic models. Structural rearrangements, with particular regard to liquid fluxes, require time to reach equilibrium. It follows that the typical time-dependence of mechanical behaviour can be phenomenologically interpreted by visco-hyperelastic models (Limbert and Middleton 2004; Natali et al. 2004; Fung 1981).

As regards the ankle ligaments tissue, this is characterized by a composite configuration, as collagen fibers bundles embedded within an isotropic ground substance. Transversally isotropic behaviour is assumed because fibers are locally distributed along one main preferential direction. In Figure 3.14 the main direction of collagen fibers of the ankle ligaments is reported. The crimped conformation of collagen fibers and interaction phenomena with ground substance entail non-linear elasticity and time-dependent phenomena, as reported in Chapter 2. Based on these assumptions the overall mechanical behaviour of ankle ligaments is interpreted by a fiber-reinforced visco-hyperelastic constitutive model.

Figure 3.14. Direction of the fibers of the CFL ligaments

3.5.1 Formulation of constitutive model

In the field of continuum mechanics, the second principle of thermodynamics states that, during a generic mechanical process, the work of internal stresses must be higher or at least equal to the energy reversibly stored within the material. In other words, mechanical work developed on the material must be higher or at least equal to the mechanical energy that the material can give back. In the latter situation, the material is conservative or hyperelastic, while in the former case the material has dissipative behaviour and a portion of the mechanical work is either used to irreversibly change the structural conformation of the material itself or it is transformed to heat. Typical examples of dissipative phenomena are damage, viscous and plastic effects.

The mathematical formulation of the second principle of thermodynamics is stated by the Clausius-Duhem dissipative inequality (Holzapfel 2000):

$$D_{\text{int}} = \frac{1}{2}\mathbf{S} : \dot{\mathbf{C}} - \dot{\psi} \geq 0 \tag{3.1}$$

where **S** is the second Piola-Kirchhoff stress tensor, **C** is the right Cauchy-Green strain tensor (Gurtin 1981), ψ is the Helmholtz free energy function and D_{int} is the rate of internal dissipation. The Helmholtz free energy defines the portion of the work of internal stresses that is reversibly stored within the material point during the

generic stress-strain path and specifies the current mechanical state of the material point itself.

According to the principles of determinism the mechanical state of the material point is determined by its strain history. It follows that the Helmholtz free energy depends on the current strain state and dissipation phenomena that eventually develop during the strain history:

$$\psi = \psi\left(\mathbf{C}, \mathbf{x}^i\right) \tag{3.2}$$

where $\mathbf{x}^i$ are internal variables that are associated with the development of dissipation phenomena. By equations (3.1), (3.2) and the chain rule, the following formulation of the rate of internal dissipation can be achieved:

$$D_{\text{int}} = \left(\frac{1}{2}\mathbf{S} - \frac{\partial \psi}{\partial \mathbf{C}}\right) : \dot{\mathbf{C}} - \frac{\partial \psi}{\partial \mathbf{x}^i} : \dot{\mathbf{x}}^i \geq 0 \tag{3.3}$$

According to the principle of universal dissipation, the previous inequality must be satisfied for any process the material can undergo (such as $\forall\, \mathbf{C}, \dot{\mathbf{C}}, \mathbf{x}^i, \dot{\mathbf{x}}^i$), entailing the following expressions for the stress and the rate of internal dissipation:

$$\mathbf{S}\left(\mathbf{C}, \boldsymbol{\omega}^i\right) = 2\frac{\partial \psi\left(\mathbf{C}, \mathbf{x}^i\right)}{\partial \mathbf{C}} \tag{3.4}$$

$$D_{\text{int}} = -\frac{\partial \psi}{\partial \mathbf{x}^i} : \dot{\mathbf{x}}^i \geq 0 \tag{3.5}$$

The definition of the constitutive model consequently requires to specify the dependence of the Helmholtz free energy on the current strain state and the internal variables. Furthermore evolution laws of the internal variables during the generic stress-strain history must be defined in accordance with the condition (3.5). The principle of frame indifference is automatically satisfied if the constitutive model is developed describing the strain state by the right Cauchy-Green strain tensor, because **C** does not depend on rigid body motions (Gurtin 1981).

3.5.2 Material symmetry

Any symmetry in the structural conformation of the material point is reflected by symmetry in its mechanical properties.

Material symmetry is mathematically characterised by a symmetry group $\mathcal{G}_{\mathbf{Q}}$ that includes orthogonal transformations that leave the Helmholtz free energy function unchanged when applied to the material point before any deformation process (Limbert and Taylor 2002). If the sub-components of the material point are equally distributed along all the directions, the material is said to have isotropic behaviour. In this event, mechanical properties do not depend on the specific direction and the symmetry group is composed by all the orthogonal transformations.

The Helmholtz free energy function is said to have isotropic behaviour (Gurtin 1981) and its dependence on the current strain state can be specified by the three principal invariants of the right Cauchy-Green strain tensor (Holzapfel 2000):

$$I_1 = tr\left(\mathbf{C}\right),\ I_2 = 1/2\left[I_1^{\,2} - tr\left(\mathbf{C}^2\right)\right],\ I_3 = J^2 = det\left(\mathbf{C}\right) \tag{3.6}$$

where $J = det\ (\mathbf{F})$ is the deformation Jacobian and $\mathbf{F}$ the deformation gradient.

The correct evaluation of both contributions from first and second invariants I_1, I_2 requires a large set of experimental data from tests developed according to different strain states, such as un-iaxial, biaxial and shear. The I_1, I_2 response terms are highly co-linear for uni-axial deformations and consequently the contribution of the second invariant is usually neglected when data from uniaxial tests only are available.

When sub-components of the material point are distributed according to preferential directions, the material is characterised by anisotropic behaviour and mechanical properties change with the direction considered.

Soft tissue is usually composed of fibrous elements embedded within an isotropic ground matrix. The distribution of fibers along preferential directions is responsible for its typical anisotropic behaviour (Spencer 1992).

With regard to biological elements, such as tendons and ligaments, it is often possible to assume fibrous elements locally aligned along only one direction (Figure 3.15a). The distribution of fibers in the undeformed configuration is usually

described by a unit vector field $\mathbf{a}_0$ that is locally tangent to fibrous components (Figure 3.15b).

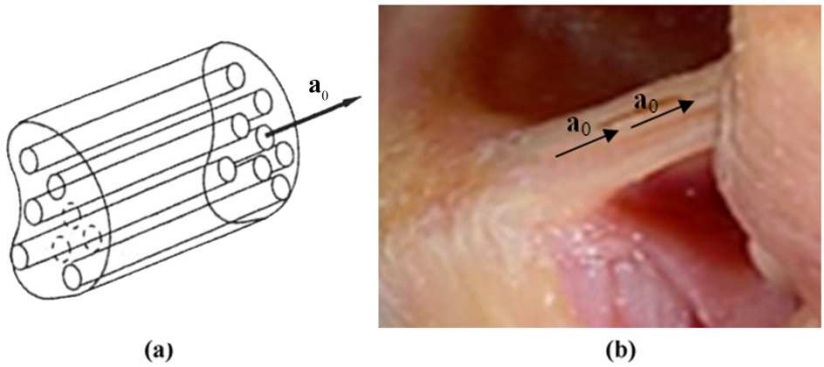

Figure 3.15: (a) Schematic representation of a transversally isotropic fiber-reinforced composite material. (b) Mathematical description of the distribution of collagen fibers by the unit vector field a_0 into a talo-calcaneal ligaments (histology from Keller et al. 2010).

The local vector $\mathbf{a}_0$ defines the preferential direction of the material point, while in the plane normal to $\mathbf{a}_0$ (the isotropic plane) mechanical properties are the same along all directions. The group of symmetry is composed by the orthogonal transformations around the axis $\mathbf{a}_0$ and the material point is said to have a transversally isotropic behaviour:

$$\mathcal{G}_{\mathbf{Q}} = \left\{ \mathbf{Q} \in Orth^{+} \mid \mathbf{Q}\mathbf{a}_0 = \mathbf{a}_0 \right\} \tag{3.7}$$

The dependence of the Helmholtz free energy function on the current strain state can be specified by the three principal invariants of the right Cauchy-Green strain tensor ($\mathbf{C}$) plus two further invariants (Spencer 1992):

$$I_4 = \mathbf{a}_0 \cdot \mathbf{C}\,\mathbf{a}_0 = \lambda^2,\ I_5 = \mathbf{a}_0 \cdot \mathbf{C}^2\,\mathbf{a}_0 \tag{3.8}$$

The fourth invariant equals the square of the stretch λ along the preferential direction $\mathbf{a}_0$. The fifth invariant specifies the influence of shear conditions on the behaviour of the fibers. The concept is explained in Figure 3.16, whereby a simple shear deformation is considered for two different spatial orientations of the fibers: either

aligned in the shear plane or aligned perpendicularly to the shear plane. It is clear that the fourth invariant is constant in both the cases, while the fifth invariant assumes different values.

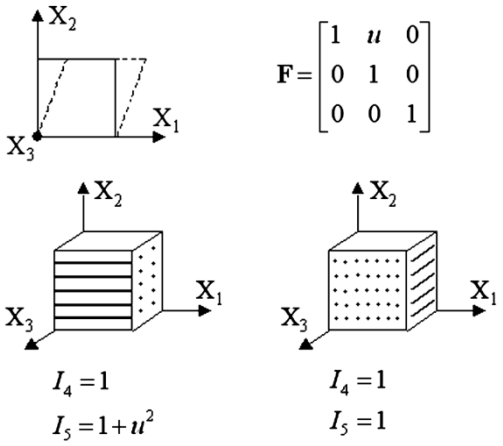

Figure 3.16: Effects of a pure shear deformation in the plane (X_1, X_2) on the I_4 and I_5 in the case of two different alignments of the fibers. The fourth invariant is constant, both for the case of fibers in the shear plane (along direction X_1) and in the case of fibers normal to the shear plane (along direction X_3). I_5 depends on the shear deformation in the case of fibers lying in the shear plane

Referring to the soft biological tissues, as in the case of the ankle ligaments, the weakness of the fiber-matrix interface suggests the removal of the fifth invariant within the definition of the constitutive model (Natali et al. 2004).

In the case of materials with isotropic matrix reinforced by two or more groups of fibers with different orientation, the use of further invariants is required. A more general dissertation on this topic can be found in the literature (Limbert and Taylor, 2002; Spencer 1992).

3.5.3 Hyperelastic constitutive models

A material is said to have hyperelastic behaviour if the internal dissipation equals zero for every stress-strain path (Truesdell and Noll 1992). This means that the rate of internal dissipation (D_{int}) equals zero for any process the material undergoes:

$$D_{\text{int}} = -\frac{\partial \psi}{\partial \mathbf{x}_i} : \dot{\mathbf{x}}_i = 0 \qquad \forall\, \mathbf{C}, \dot{\mathbf{C}}, \mathbf{x}_i, \dot{\mathbf{x}}_i \tag{3.9}$$

where ψ is the Helmholtz free energy function and $\mathbf{x}^i$ are internal variables that are associated with the development of dissipation phenomena. It follows that the Helmholtz free energy function depends only on the current strain state and the work of internal stresses is independent on the stress-strain path (Belytschko et al. 2001). The Helmholtz free energy function is consequently a potential of the strain state and is usually called strain energy function $\psi = W(\mathbf{C})$. The stress-strain relationship can be calculated according to the equation:

$$\mathbf{S}(\mathbf{C}) = 2\frac{\partial W(\mathbf{C})}{\partial \mathbf{C}} \tag{3.10}$$

The formulation of a hyperelastic model only needs to specify the dependence of the strain energy function on the strain state, carefully accounting for inequalities which define the material stability requirements (Schroder et al. 2005; Marsden and Hughes 1983). The strain energy function is usually formulated by analyzing the inner conformation of the material and experimental data that characterise its mechanical behaviour.

3.5.3.1 Isotropic hyperelastic model

The strain energy function of an isotropic material is an isotropic function of the current strain state (Gurtin 1981). It can be expressed in terms of the three principal invariants of the right Cauchy-Green strain tensor:

$$W(\mathbf{C}) = W(I_1, I_2, I_3) \tag{3.11}$$

According to equations (3.10) and (3.11), the stress-strain relationship can be reformulated by applying the chain rule:

$$\mathbf{S} = 2\frac{\partial W}{\partial \mathbf{C}} = 2\sum_{i=1}^{3}\frac{\partial W}{\partial I_i}\frac{\partial I_i}{\partial \mathbf{C}} \tag{3.12}$$

the derivatives of the principal invariants can be computed from (3.6):

$$\frac{\partial I_1}{\partial \mathbf{C}} = \mathbf{1},\ \frac{\partial I_2}{\partial \mathbf{C}} = I_1\mathbf{1} - \mathbf{C},\ \frac{\partial I_3}{\partial \mathbf{C}} = I_3\mathbf{C}^{-1} \tag{3.13}$$

where **1** is the rank two unit tensor. Soft biological tissues usually contain a large liquid content, composed predominantly of water. Part of this water is chemically bound to the solid matrix and, therefore, cannot move through the tissue. In addition, the quantity of water that is free to move within the tissue can be considered to be bound if the tissue is strained with high rates of loading. Indeed, in such cases, low permeability values represent an effective obstacle to fluid motion. A direct consequence of this structural conformation is the fact that the tissue can behave like an almost-incompressible material. Therefore, a suitable numerical framework for the analysis of the mechanical behaviour of soft tissues requires us to split the strain energy function and the stress response of the isotropic matrix in volumetric and volume-preserving (or iso-volumetric) parts (Flory 1961). The strain energy function is then defined by the following form:

$$W_m\left(I_1, I_2, I_3\right) = W_{mv}\left(I_3\right) + W_{mi}\left(\tilde{I}_1, \tilde{I}_2\right) \tag{3.14}$$

where $\tilde{I}_1, \tilde{I}_2$ are the two principal invariants of the volume-preserving part of the right Cauchy-Green tensor $\tilde{\mathbf{C}} = I_3^{-1/3}\mathbf{C}$. W_{mv} is related to the volumetric part of strain and W_{mi} to the volume-preserving part.

3.5.3.2 Fiber-reinforced hyperelastic model

In the case of transversally isotropic materials, it can be demonstrated (Spencer 1992) that the strain energy function depends on five invariants, including the three principal invariants of the right Cauchy-Green tensor plus two further invariants:

$$W(\mathbf{C}) = W\left(I_1, I_2, I_3, I_4, I_5\right) \tag{3.15}$$

The invariants I_4 and I_5 arise directly from the anisotropy introduced by the fibers and specifies the contributions to the strain energy function from the properties of the fibers and their interaction with the other material constituents (Weiss et al. 1996). The stress response is then given by:

$$\mathbf{S} = 2\frac{\partial W}{\partial \mathbf{C}} = 2\sum_{i=1}^{5}\frac{\partial W}{\partial I_i}\frac{\partial I_i}{\partial \mathbf{C}} \tag{3.16}$$

where the derivatives of the fourth and fifth invariants are defined as follows:

$$\frac{\partial I_4}{\partial \mathbf{C}} = \mathbf{a}_0 \otimes \mathbf{a}_0, \quad \frac{\partial I_5}{\partial \mathbf{C}} = \mathbf{a}_0 \otimes \mathbf{C}\mathbf{a}_0 + \mathbf{C}\mathbf{a}_0 \otimes \mathbf{a}_0 \tag{3.17}$$

The hyperelastic behaviour of soft biological tissues arises from the resistance of the ground matrix, the fibers and their interaction.
Consequently, the strain energy function can be additively decomposed:

$$W\left(I_1, I_2, I_3, I_4, I_5\right) = W_m\left(\tilde{I}_1, \tilde{I}_2, I_3\right) + W_f\left(I_4, I_5\right) + W_{mf}\left(I_1, I_2, I_3, I_4, I_5\right) \tag{3.18}$$

where W_m represents the material response of the isotropic ground matrix, W_f represents the contribution from fibers and W_{mf} is the contribution from interactions between fibers and the matrix.
In the general framework of fiber-reinforced composite materials, the function W_{mf} specifies the effects that are determined by the varying stiffness that characterises fibers and the matrix. These effects are particularly relevant when strong bonds effectively take place between the two phases. With regard to soft biological tissues, such as hindfoot ligaments, the bonds between fibers and ground substance are usually very weak or totally absent. It follows then, that the term W_{mf} can be neglected (Limbert and Middleton 2006; Natali et al. 2003). As previously reported, the almost incompressible behaviour of the ground matrix suggests that its contribution can be split into volumetric (W_{mv}) and iso-volumetric (W_{mi}) parts, leading to the following formulation of the strain energy function:

$$W\left(I_1, I_2, I_3, I_4, I_5\right) = W_{mv}\left(I_3\right) + W_{mi}\left(\tilde{I}_1, \tilde{I}_2\right) + W_f\left(I_4, I_5\right) \tag{3.19}$$

The volumetric contribution to strain energy is mainly due to the mechanical response of liquid components and the electrostatic interaction phenomena taking place inside the ground substance. In fact, proteoglycans are characterised by a distribution of negative charges that interact with water positive sodium ions. Compressive loads determine a tendency towards squeezing water out of the network and bringing the proteoglycans closer. These phenomena are counteracted respectively by electrostatic interactions of proteoglycans and sodium ions (Loret and Simoes, 2004).

The application of tensile load determinates a lower water squeezing tendency and proteoglycans tend to get further, leading to a different tensile response from the compressive condition. The following formulation of the volumetric term is able to account for previous characteristics:

$$W_{mv}\left(I_3\right) = \frac{K_v}{2 + r\left(r+1\right)}\left[\left(I_3^{1/2} - 1\right)^2 + I_3^{-r/2} + rI_3^{1/2} - \left(r+1\right)\right] \tag{3.20}$$

where K_v and r characterise the material compressibility and can be related to the tangent bulk modulus:

$$K^T = \frac{K_v}{2 + r\left(r+1\right)}\left[2 + r\left(r+1\right) I_3^{-(r+2)/2}\right] \tag{3.21}$$

It is possible to assume that K_v is the tangent bulk modulus in the unstrained configuration. With particular regard to compressive conditions, the characteristic non-linear response of the ground matrix, as outlined by experimental data (Nishihira et al. 2003), suggests the assumption of an exponential formulation for the volume-preserving term (Fung 1981):

$$W_{mi}\left(\tilde{I}_1\right) = \frac{C_1}{\alpha_1}\left\{\exp\left[\alpha_1\left(\tilde{I}_1 - 3\right)\right] - 1\right\} \tag{3.22}$$

where C_1 characterises the shear stiffness of the tissue, as $G=2C_1$, while α_1 is a parameter that regulates the non linearity of the material response, with reference to experimental results.

The mechanical contribution of fibers can be described by considering their microstructural organization (Redaelli et al. 2003; Ottani et al. 2001). In the unstrained configuration, fibers are usually characterised by a typical wavy conformation. When tensile load is applied along the direction of the fibers, they first uncrimp and then get stretched. This mechanism determines a strongly non-linear mechanical response that can be described by an exponential formulation of the fibers strain energy contribution (Natali et al. 2003; Weiss et al. 1996):

$$W_f\left(I_4\right)=\frac{C_4}{\left(\alpha_4\right)^2}\left\{\exp\left[\alpha_4\left(I_4-1\right)\right]-\alpha_4\left(I_4-1\right)-1\right\} \tag{3.23}$$

where C_4 is a constant that defines the initial stiffness of the fibers, as $E_f=4C_4$, while α_4 depends on the initial wavy conformation of fibers (Natali et al. 2004, 2005). The influence of the fifth invariant is omitted in this formulation, because the contribution of the fibers to the tissue shear behaviour is often really poor (Weiss et al. 1996). When compressive loads are applied to soft biological tissues, fibers undergo a micro-buckling phenomena. Consequently, contribution of fibers to overall mechanical response of the tissue is really lower for a compressive situation than a tensile one. Exponential formulations as (3.23) are able to account for this peculiar aspect.

The specific stress-strain relationship can be calculated according to equations 3.16, 3.20, 3.22 and 3.23:

$$\mathbf{S}_{mv}=\frac{K_v}{2+r\left(r+1\right)}\left[2I_3^{1/2}\left(I_3^{1/2}-1\right)-rI_3^{-r/2}+rI_3^{1/2}\right]\mathbf{C}^{-1} \tag{3.24}$$

$$\mathbf{S}_{mi}=C_1\exp\left[\alpha_1\left(\tilde{I}_1-3\right)\right]\left[2I_3^{-1/3}\mathbf{1}-2/3\tilde{I}_1\mathbf{C}^{-1}\right] \tag{3.25}$$

$$\mathbf{S}_f=2\frac{C_4}{\alpha_4}\left\{\exp\left[\alpha_4\left(I_4-1\right)\right]-1\right\}\mathbf{a_0}\otimes\mathbf{a_0} \tag{3.26}$$

3.5.4 Fiber-reinforced visco-hyperelastic model

The time-dependent behaviour of the ankle ligaments (Attarian et al. 1985) is due to the development of structural conformation rearrangements (such as fluid fluxes through the solid skeleton, the sliding of macromolecules, etc.) that develop during the loading of the material. From a phenomenological point of view, typical examples of viscous effects in the ligaments are creep, stress-relaxation and hysteresis (as reported in Chapter 2). Rearrangement phenomena are usually defined as viscoelastic processes and can be associated with internal variables $\mathbf{q}^i$, which express material evolution during the stress-strain history from a phenomenological point of view. The mechanical state of the material is described by a specific configuration of the Helmholtz free energy function that is specified by contributions from the ground matrix and fibers:

$$\psi\left(\mathbf{C},\mathbf{q}_m^i,\mathbf{q}_f^i\right)=\psi_m\left(\mathbf{C},\mathbf{q}_m^i\right)+\psi_f\left(\mathbf{C},\mathbf{q}_f^i\right) \tag{3.27}$$

The specific formulation of the Helmholtz free energy can be developed by accounting for mechanical models that are capable of describing the behaviour of the material phenomenologically. Within visco-elastic theories the Zener model (Figure 3.17) is frequently adopted. This model is made up of an equilibrium spring and viscoelastic branches connected in parallel (Natali et al. 2004; McCrum et al. 1997).

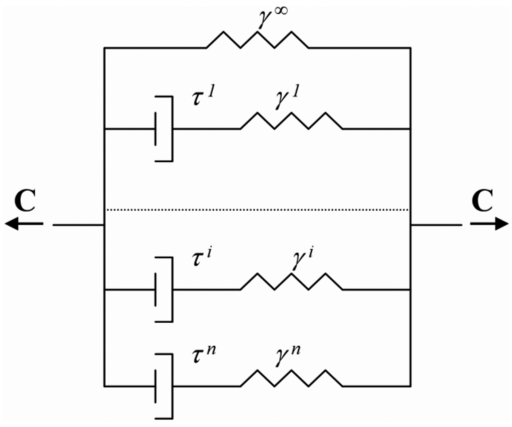

Figure 3.17. Zener rheological model.

Every viscoelastic branch phenomenologically represents a viscoelastic process, which is characterised by a relative elastic stiffness γ_j^i and a relaxation time τ_j^i with j=*m,f*. The relative stiffness describes the contributions of the viscous process to the whole instantaneous stiffness of the material, which is the stiffness during a straining process characterised by an infinite strain rate. The relative stiffness have to satisfy the following relationship (Simo and Hughes 1998):

$$\gamma_j^{\infty} + \sum_{i=1}^{n} \gamma_j^i = 1 \tag{3.28}$$

where γ_j^{∞} is the relative stiffness of the equilibrium spring, which defines the material behaviour during an equilibrium strain process (i.e. a process that is characterised by a strain rate approaching zero). The analysis of the Zener model suggests the formulation of a Helmholtz free energy capable of interpreting the visco-hyperelastic behaviour:

$$\psi_j\left(\mathbf{C}, \mathbf{q}_j^i\right) = W_j^{\infty}\left(\mathbf{C}\right) + \sum_{i=1}^{n} \psi_j^i\left(\mathbf{C}, \mathbf{q}_j^i\right) \tag{3.29}$$

where W_j^{∞} is an hyperelastic potential that defines the behaviour of the equilibrium spring, while ψ_j^i is the Helmholtz free energy related to the i^{th} viscous branch. In the present approach the variables $\mathbf{q}^{\text{i}}_{\text{j}}$ describe the non-equilibrium stresses associated with the viscous processes and the following formulation of ψ_j^i is assumed (Natali et al. 2006):

$$\psi_j^i\left(\mathbf{C}, \mathbf{q}_j^i\right) = W_j^i\left(\mathbf{C}\right) - \frac{1}{2}\mathbf{q}_j^i : \mathbf{C} \tag{3.30}$$

where W_j^i is an hyperelastic potential associated with the i^{th} spring, while the second term is the energy dissipated because of the viscous process.

The evolution law for viscous variables $\mathbf{q}^{i}_{j}$ can be obtained by means of the Zener model. The imposition of a strain compatibility condition on the whole Zener model and a stress equilibrium condition on every single viscoelastic branch makes it possible to achieve the following equations:

$$\dot{\mathbf{q}}^{i}_{j} + \frac{1}{\tau^{i}_{j}}\mathbf{q}^{i}_{j} = 2\frac{\gamma^{i}_{j}}{\tau^{i}_{j}\gamma^{\infty}_{j}}\frac{\partial W^{\infty}_{j}}{\partial \mathbf{C}} \tag{3.31}$$

The above expression is a system of first-order ordinary differential equations that, with the introduction of the condition of null initial non-equilibrium stresses, as $\lim_{t\to 0}\mathbf{q}_{i} = \mathbf{0}$, can be solved in the following convolution integrals:

$$\mathbf{q}^{i}_{j}(t) = \frac{\gamma^{i}_{j}}{\gamma^{\infty}_{j}\tau^{i}_{j}}\int_{0}^{t}\exp\left(-\frac{t-s}{\tau^{i}_{j}}\right)\mathbf{S}^{\infty}_{j}(s)\,ds \tag{3.32}$$

The specific stress-strain relationship can be calculated according to equations 3.29:

$$\mathbf{S}\left(\mathbf{C},\mathbf{q}^{i}\right) = 2\frac{\partial W^{\infty}_{j}}{\partial \mathbf{C}} + \sum_{i=1}^{n}\left[2\frac{\partial W^{i}_{j}}{\partial \mathbf{C}} - \mathbf{q}^{i}_{j}\right] = \mathbf{S}^{\infty}_{j}(\mathbf{C}) + \sum_{i=1}^{n}\mathbf{S}^{i}_{j}\left(\mathbf{C},\mathbf{q}^{i}_{j}\right) \tag{3.33}$$

where W^{∞}_{j} and W^{i}_{j} can be related to an instantaneous hyperelastic strain energy W^{0}_{j}, as $W^{\infty}_{j} = \gamma^{\infty}_{j}W^{0}_{j}$ and $W^{i}_{j} = \gamma^{i}_{j}W^{0}_{j}$.

3.6. References

Antunes P.J., Dias G.R., Coelho A.T., Rebelo F., Pereira T., 2010. Non-linear finite element modelling of anatomically detailed 3D foot model, http://www.materialise.com.

Attarian D.E, McCrackin H.J., DeVito D.P., McElhaney J.H., Garrett W.E., 1985a. Biomechanical characteristis of human ankle ligaments, Foot & Ankle, vol. 6(2), pp. 54-58.

Ayache N., 1995. Medical computer vision, virtual reality and robotics, Image and Vision Computing, vol. 13(4), pp. 295-313.

Belytschko T., Liu W. K., Moran B., 2001. Nonlinear finite elements for continua and structures, John Wiley & Sons LTD, New York

Boss A.P., Hintermann B., 2002. Anatomical study of the medial ankle ligament complex, Foot & Ankle International, vol.23 (6), pp. 547-553.

Burks R.T., Morgan J., 1994. Anatomy of the lateral ankle ligaments. The American Journal of Sports Medicine, vol.22, pp.72-73.

Butler A.M., Walsh W.R., 2004. Mechanical Response of Ankle Ligaments at Low Loads, Foot & Ankle International, vol.25 (1), pp. 8-12.

Cheung J.T.M, Nigg B.M., 2007. Clinical Applications of Computational Simulation of Foot and Ankle, Sport Orthopadie Traumatologie, vol. 23, pp. 264-271.

Cheung JTM, Zhang M, Kam Lun Leung A, Fan YB, 2005. Three-dimensional finite element analysis of the foot during standing—a material sensitivity study, Journal of Biomechanics, vol. 38, pp. 1045-1054.

De Souza V.A., 2007. Design of insole using image base analysis, PhD Thesis, The University of Tokyo, Graduate School of Frontier Sciences.

Flory P.J., 1961. Thermodynamic relations for high elastic materials, Transactions of Faraday Society, vol. 57, pp. 829-838.

Fung Y.C., 1981. Biomechanics: mechanical properties of living tissues, Springer-Verlag, New York.

Gefen A., 2002. Biomechanical analysis of fatigue-related foot injury mechanism in athletes and recruits during intensive marching. Medical & Biological Engineering & Computing, vol. 40(3), pp.302-310.

Gurtin, M.E., 1981. An introduction to continuum mechanics, Academic Press, San Diego.

Hahn T., 1987. Space-group symmetry (second edition), Dreidel D, Dordrecht.

Holzapfel G.A., 2000. Nonlinear solid mechanics, John Wiley & Sons LTD, New York.

Imhauser C.W., 2004. The development and evaluation of a 3 dimensional, image-based, patient-specific, dynamic model of the hindfoot, Doctoral thesis of Drexel University.

Keller K., Nasrilari M., Filler T., Jerosch J., 2010. The anterior tibio-talar ligament: one reason for anterior ankle impingement, Knee Surgery, Sports Traumatology, Arthroscopy, vol.18, pp. 225–232.

Korioth T.W.P., Versluis A., 1997. Modelling the mechanical behaviour of the jaws and their related structures by finite element (FE) analysis, Critical review in Oral Biology & Medicine, vol. 8(1), pp. 90-104.

Limbert G., Middleton J., 2004. A transversally isotropic viscohyperelastic material: Application to the modeling of biological soft connective tissues, International Journal of Solids and Structures, vol. 41, pp. 4237-4260.

Limbert G., Taylor M., 2002. On the constitutive modelling of biological soft connective tissues: A general theoretical framework and explicit forms of the tensors of elasticity for strongly anisotropic continuum fiber-reinforced composites at finite strain, International Journal of Solids and Structures, vol. 39, pp. 2343-2358.

Loret B., Simoes F.M.F., 2004. Articular cartilage with intra- and extrafibrillar waters : a chemo-mechanical model, Mechanics of Materials, vol. 36, pp. 515-541.

Mangwani J., Hakmi M. A., Smith T. W. D., 2001. Chronic lateral ankle instability: review of anatomy, biomechanics, pathology, diagnosis and treatment, The Foot, vol. 11, pp. 76-84.

Marsden J.E., Hughes T.J.R., 1983. Mathematical Foundations of Elasticity, Prentice-Hall, Englewood Cliffs, NJ.

Matteoli S., Crovi A., Wilhjelm J.E., 2010. Modeling the human heel pad, Simpleware Users' Meeting, Solihull, 3 June 2010.

McCrum, N.G., Buckley, C.P., Bucknall, C.B., 1997. Principles of polymers engineering, Oxford Science Publications, Oxford.

Milner C.E, Soames R.W., 1997. Anatomical variations of the anterior talofibular ligament of the human ankle joint, Journal of Anatomy, vol. 191, pp.457-458.

Mkandawire C., Ledoux W.R., Sangeorzan B.J., Ching R.P, 2005. Foot and ankle ligament morphometry. Journal of Rehabilitation Research and Development, vol. 42 (6), pp. 809-820.

Muhle C., Frank R.F., Rand T., Yeh L., Wong E.C., Skaf A., Dantas R.W.M., Haghighi P., Trudell D., Resnick D., 1999. Collateral ligaments of the ankle: high-resolution MR imaging with a local gradient coil and anatomic correlation in cadavers, RadioGraphics, vol. 19, pp. 673-683.

Natali A.N., Carniel E.L., Pavan P.G., Gasparetto A., Sander F.G., Dorow C., Gaiger M., 2006. Constitutive formulation for numerical analysis of visco-elastic damage phenomena in soft biological tissues, ASME proceedings of ESDA2006, Torino (I), pp. 1-8.

Natali A.N., Pavan P.G., Carniel E.L., Dorow C., 2003. A transversally isotropic elasto-damage constitutive model for the periodontal ligament, Computer Methods in Biomechanics and Biomedical Engineering, vol. 6, pp. 329-336.

Natali A.N., Pavan P.G., Carniel E.L., Dorow C., 2004. Viscoelastic response of the periodontal ligament: an experimental-numerical analysis, Connective Tissue Research, vol. 45, pp. 222-230.

Natali A.N., Pavan P.G., Carniel E.L., Lucisano M.E., Taglialavoro G., 2005. Anisotropic elasto-damage constitutive model for the biomechanical analysis of tendons, Medical Engineering and Physics, vol. 27, pp. 209-214.

Nishihira M., Yamamoto K., Sato Y., Ishikawa H. Natali A.N., 2003. Mechanics of periodontal ligament. In Natali A.N. (editor), Dental biomechanics, Taylor & Francis, London, pp. 20-34.

Ogden R.W., 1984. Non-linear elastic deformations, Ellis Horwood Ltd., West Sussex.

Ottani V., Raspanti M., Ruggeri A., 2001. Collagen structure and functional implications, Micron, vol. 32, pp. 251-260.

Reach J.S., Amrami K.K., Felmlee J.P., Stnley D.W., Alcorn J.M., Turner N.S., Carmichael S.W., 2007. Anatomic compartments of the foot: a 3-tesla magnetic resonance imaging study, Clinical Anatomy, vol. 20, pp. 201-208.

Redaelli A., Vesentini S., Soncini M., Vena P., Mantero S., Montevecchi F.M., 2003. Possible role of decorin glycosaminoglycans in fibril to fibril force transfer in relative mature tendons - a computational study from molecular to microstructural level, Journal of Biomechanics, vol. 36, pp. 1555-1569.

Rosenberg Z.S., Beltran J., Bencardino J.T., 2000. MR Imaging of the Ankle and Foot, Radiographics, vol. 20, pp. S153-S179.

Schroder J., Neff P., Balzani D., 2005. A variational approach for materially stable anisotropic hyperelasticity, International Journal of Solids and Structures, vol. 42, pp. 4352-4371.

Siegler S., Block J., Schneck C.D., 1988. The mechanical characteristics of the collateral ligaments of the human ankle joint, Foot & Ankle, vol.8, num.5, pp. 234-242.

Simo, J.C., Hughes, T.J.R., 1998. Computational Inelasticity, Springer, New York.

Spencer A.J.M., 1992. Continuum theory of the mechanics of fiber-reinforced composites, Springer-Verlag, New York.

Spilker R.L., Suh J.K., Mow V.C., 1992. A finite element analysis of the indentation stress-relaxation response of linear biphasic articular cartilage, Journal of Biomechanical Engineering, vol. 114, pp. 191-201.

Stytz M.R., Frieder G., Frieder O., 1991. Three-dimensional medical imaging: algorithms and computer systems, ACM Computing Surveys, vol. 23(4), pp. 421-499.

Truesdell C., Noll W., 1992. The non-linear field theories of mechanics (second edition), Springer-Verlag, Berlin.

Van Den Bekerom M.P.J., Oostra R.J., Alvarez P.G., Dijk N.V., 2008. The anatomy in relation to injury of the lateral collateral ligaments of the ankle, Clinical Anatomy, vol. 21, pp. 619-626.

Vannier M.W., Hildebolt C.F., Conover G., Knapp R.H., Yokoyama-Crothers N., Wang G., 1997. Three-dimensional dental imaging by spiral CT, Oral surgery, Oral Medicine, Oral Pathology Oral and Maxillofacial Radiology, vol. 84(5), pp. 561-570.

Wang K.T.D., Wang C., Wang X., Liu A., Nester C.J., Howard D., 2009. An in vivo experimental validation of a computational model of human foot, Journal of Bionic Engineering, vol. 6, pp. 387-397.

Weiss J.A., Maker B.N., Govindjee S., 1996. Finite element implementation of incompressible, transversely isotropic hyperelasticity, Computer methods in applied mechanics and engineering, vol. 135, pp. 107-128.

Yu J., Cheung J.T.M., Fan Y., Zhang Y., Leung A.K.L., Zhang M., 2008. Development of a finite element model of female foot for high heeled shoe design, Clinical Biomechanics, vol. 23, pp. S31-S38.

CHAPTER 4

EVALUATION OF THE CONSTITUTIVE PARAMETERS OF THE LIGAMENTS OF THE HINDFOOT

4.1 Introduction

Once constitutive model is formulated, it is necessary to evaluate the constitutive parameters that characterise the mechanical behaviour of the hindfoot ligaments tissues. This chapter describes a procedure for the evaluation of constitutive parameters using a combined experimental and computational approach.

The non-linearity of the mechanical behaviour of ligaments tissue requires that constitutive parameters are evaluated by directly comparing analytical and numerical model results with experimental data. To define the discrepancy existing between experimental data and model results a specific cost function is formulated. Constitutive parameters are evaluated by minimizing the cost function through a stochastic-deterministic procedure. To define a preliminary set of constitutive parameters analytical model is provided, taking into consideration the fiber-reinforced visco-hyperelastic formulation and the boundary conditions of specific experimental tensile tests. In order to come up with a formulation capable of interpreting the actual response of ligaments tissues, constitutive parameters are subsequently improved by means of a comparison with results from a numerical analysis that consider the complex histo-morphometric configuration of experimental samples and boundary conditions. Numerical analyses are performed assuming different sets of parameters starting from the preliminary set. The minimization of the discrepancy between experimental and numerical model results entails the definition of a reliable set of parameters.

4.2 Procedure for identifying the constitutive parameters of the ligaments

The definition of parameters that govern the constitutive equations of biological materials is a challenge that becomes difficult to face when the number of parameters is significant. Such a case occurs when anisotropic materials and refined nonlinear laws are considered (Grédiac et al. 2002; Araújo et al. 1996). The usual approach consists in the inverse analysis of constitutive models. An inverse analysis assumes that stress-strain history is given by experimental procedures and it attempts to estimate parameter values that would yield the best fit to the given stress-strain history (Lei and Szeri 2006). Constitutive parameters are consequently evaluated using experimental data, corresponding analytical model results and optimization techniques. Mechanical tests should be performed on geometrically simple specimens and appropriate boundary conditions should be adopted to generate the most homogeneous stress-strain fields possible. Indeed, simple experimental tests can be described using analytical formulations. For more complicated situations, numerical methods must be adopted.

Furthermore, experimental data should explore several different deformation modes in order to provide the necessary information for the characterisation of the generic stress-strain behaviour of the tissue and the univocal definition of constitutive parameters (Natali et al. 2006).

4.2.1 Definition of the cost function

The procedure adopted for the definition of the constitutive parameters requires the minimization of the discrepancy between experimental and analytical or numerical model results through a specific cost function.

The cost function depends on the accuracy of the input data (such as experimental data), the quantity of data at disposal and the weight that each data is associated with. There are several cost function proposed in literature (Praagman et al. 2006; Cash et al 2005, Stokes et al. 2001; Kyriacou and Davatzikos 1998; Crowninshield and Brand 1981). With regard to the biomechanical contest, the cost function used (Natali et al. 2009a, 2009b, 2010b) is reported in equation 4.1 where the weight of each data in the output is related with the ratio between the experimental data and model results:

$$\Omega(\boldsymbol{\omega}) = \frac{1}{n}\sqrt{\sum_{i=1}^{n}\left[2 - \frac{P_{ii}^{mod}\left(\boldsymbol{\omega}, \lambda_i^{exp}\right)}{P_{ii}^{exp}} - \frac{P_{ii}^{exp}}{P_{ii}^{mod}\left(\boldsymbol{\omega}, \lambda_i^{exp}\right)}\right]^2} \tag{4.1}$$

where $\boldsymbol{\omega}$ is the set of constitutive parameters, n the number of experimental data, λ_i^{exp} the i^{th} experimental input datum, P_{ii}^{exp} the i^{th} experimental output value, and P_{ii}^{mod} the i^{th} analytical or numerical model output result corresponding to the constitutive parameters $\boldsymbol{\omega}$ and the experimental input λ_i^{exp}. The function Ω is a measure of the overall difference between experimental and model results when constitutive parameters $\boldsymbol{\omega}$ are adopted. The optimization problem involves the evaluation of the set of constitutive parameters $\boldsymbol{\omega}_{opt}$ that minimizes Ω.

Some limitations on constitutive parameters may be necessary, including, for example, the imposition on the tendency of the hyperelastic strain energy function to increase strictly with strain. It may be difficult to define these conditions by boundaries the parameters domain and should be more easily implemented by penalty contributions to the cost function (Boukari and Fiacco 1995):

$$\Omega(\boldsymbol{\omega}) = \frac{1}{n}\sqrt{\sum_{i=1}^{n}\left[2 - \frac{P_{ii}^{mod}\left(\boldsymbol{\omega}, \lambda_i^{exp}\right)}{P_{ii}^{exp}} - \frac{P_{ii}^{exp}}{P_{ii}^{mod}\left(\boldsymbol{\omega}, \lambda_i^{exp}\right)}\right]^2} + \frac{1}{n}\sum_{i=1}^{n}\Theta_i\left(\boldsymbol{\omega}, \lambda_i^{exp}, P_{ii}^{exp}, P_{ii}^{mod}\right) \tag{4.2}$$

where the penalty term Θ_i assumes a reasonably high value when the model result P_{ii}^{mod} does not satisfy a specified criterion.

4.2.2 Implementation of a stochastic-deterministic procedure

If the adopted constitutive model is highly non-linear, the cost function is often characterised by multimodal behaviour (i.e. the function presents a global minimum and further local minima). Solving the optimization problem by deterministic methods (Stoer and Bulirsch 1992) may result in the definition of only one of the local minima, without generating the optimal solution. On the other hand, a stochastic algorithm performs well in the presence of a very high number of variables. This is based on random evaluations of the cost function, in such a way

that transitions out of a local minimum are possible, but it does not guarantee reaching the global minimum, but only moving close to the minimum itself.

It becomes necessary, therefore, to perform the optimization using a new algorithm formulated by coupling a stochastic and deterministic method.

A specific simulated annealing procedure (Corana et al. 1987; Kirkpatrick et al. 1983) and the Nelder-Mead method (Begambre and Laier 2009; Lagarias et al. 1998) can be adopted for this purpose. The new procedure explores all minima, evaluates the region where the global minimum is located and then returns to the exact position of the global minimum itself. More specifically, the computation begins from an initial set of constitutive parameters that is recorded in the vector $\boldsymbol{\omega}_0$. According to the simulating annealing technique, new candidate points $\boldsymbol{\omega}'$ are generated around the current point $\boldsymbol{\omega}_{i,}$ by applying random moves. A new point $\boldsymbol{\omega}'$ is accepted or rejected according to the Metropolis criterion (Metropolis et al. 1953) leading to a new current position $\boldsymbol{\omega}_{i+1}$. The best point reached corresponding to the set of constitutive parameters that mainly minimizes the cost function is recorded as $\boldsymbol{\omega}^*_{opt.}$ The solution is used as input to the Nelder Mead method that returns a new point $\boldsymbol{\omega}^{**}_{opt}$ that is compared with the previous $\boldsymbol{\omega}^*_{opt}$. The best of them is recorded as $\boldsymbol{\omega}_{opt}$ until no more useful cost function improvements can be expected. The procedure returns the set of constitutive parameters associated with the best solution.

To evaluate the efficiency and the reliability of the described procedure, a test is used that refers to the Rosenbrock function, whose minimization is a classical test problem that is extensively adopted to evaluate the performance of different optimization algorithms (Begambre and Laier 2009; Hillstrom 1977). Results of the comparison between the performance of the suggested algorithm and the only simulating annealing algorithm are reported by Natali et al., 2009b.

4.2.3 Definition of the analytical models for uni-axial tests

The definition of deformation modes to be investigated by experimental methods is a fundamental task in the evaluation of constitutive parameters. Different stress-strain fields must be investigated to univocally achieve a set of parameters able to describe the generic mechanical behaviour of the biological tissue (Natali et al. 2006).

The first step of the procedure is to develop analytical models to interpret the experimental tests, accounting for the constitutive formulation and the specific boundary conditions. With regard to the uniaxial tensile tests (Funk et al. 2000; Attarian et al. 1985), the analytical model has to provide a relationship between nominal stress along the loading direction (i.e. the ratio between the load applied and the initial cross sectional area of the specimen) and the imposed strain configuration. For a hyperelastic material, the general stress-strain relationship is evaluated as $\mathbf{P} = 2\mathbf{F}\,\partial W/\partial \mathbf{C}$, where $\mathbf{P}$ is the first Piola-Kirchhoff stress tensor, a measure of nominal stress, and $\mathbf{F}$ is the deformation gradient.

The definition of the analytical model, taking into consideration the fiber-reinforced visco-hyperelastic model, has to provide a relationship between nominal stress along the loading direction and the imposed strain hystory. Considering the proposed formulation of the strain energy function, reported in Chapter 3, the general stress-strain relationship is evaluated as:

$$\mathbf{P}\left(\mathbf{C},\mathbf{q}_m^i,\mathbf{q}_f^i\right)=\mathbf{P}_{mv}\left(\mathbf{C},\mathbf{q}_m^i\right)+\mathbf{P}_{mi}\left(\mathbf{C},\mathbf{q}_m^i\right)+\mathbf{P}_f\left(\mathbf{C},\mathbf{q}_f^i\right) \tag{4.3}$$

$$\mathbf{P}_{mv}\left(\mathbf{C},\mathbf{q}_m^i\right)=\frac{2\mathbf{F}\partial\psi_{mv}}{\partial\mathbf{C}}=\mathbf{P}_{mv}^{\infty}\left(\mathbf{C}\right)+\sum_{i=1}^{n}\left(\mathbf{P}_{mv}^{i}\left(\mathbf{C},\mathbf{q}_m^i\right)\right)=\mathbf{P}_{mv}^{\infty}\left(\mathbf{C}\right)+\left(\frac{\gamma_m^j}{\gamma_m^{\infty}}\mathbf{P}_{mv}^{\infty}\left(\mathbf{C}\right)-\mathbf{q}_m^i\right) \tag{4.4}$$

$$\mathbf{P}_{mi}\left(\mathbf{C},\mathbf{q}_m^i\right)=\frac{2\mathbf{F}\partial\psi_{mi}}{\partial\mathbf{C}}=\mathbf{P}_{mi}^{\infty}\left(\mathbf{C}\right)+\sum_{i=1}^{n}\left(\mathbf{P}_{mi}^{i}\left(\mathbf{C},\mathbf{q}_m^i\right)\right)=\mathbf{P}_{mi}^{\infty}\left(\mathbf{C}\right)+\left(\frac{\gamma_m^j}{\gamma_m^{\infty}}\mathbf{P}_{mi}^{\infty}\left(\mathbf{C}\right)-\mathbf{q}_m^i\right) \tag{4.5}$$

$$\mathbf{P}_{f}\left(\mathbf{C},\mathbf{q}_f^i\right)=\frac{2\mathbf{F}\partial\psi_{f}}{\partial\mathbf{C}}=\mathbf{P}_{f}^{\infty}\left(\mathbf{C}\right)+\sum_{i=1}^{n}\left(\mathbf{P}_{f}^{i}\left(\mathbf{C},\mathbf{q}_f^i\right)\right)=\mathbf{P}_{f}^{\infty}\left(\mathbf{C}\right)+\left(\frac{\gamma_f^j}{\gamma_f^{\infty}}\mathbf{P}_{f}^{\infty}\left(\mathbf{C}\right)-\mathbf{q}_f^i\right) \tag{4.6}$$

where

$$\mathbf{P}_{mv}^{\infty}\left(\mathbf{C}\right)=\frac{2\mathbf{F}\partial W_{mv}^{\infty}}{\partial\mathbf{C}}=\left[\frac{K_v}{2+r\left(r+1\right)}\right]\left[2I_3^{1/2}\left(I_3^{1/2}-1\right)-rI_3^{-r/2}+rI_3^{1/2}\right]\mathbf{F}^{-T} \tag{4.7}$$

$$\mathbf{P}_{mi}^{\infty}\left(\mathbf{C}\right)=\frac{2\mathbf{F}\partial W_{mi}^{\infty}}{\partial\mathbf{C}}=C_1\exp\left[\alpha_1\left(\tilde{I}_1-3\right)\right]\left(2I_3^{-1/3}\mathbf{F}-2/3\,\tilde{I}_1\mathbf{F}^{-T}\right) \tag{4.8}$$

$$\mathbf{P}_{f}^{\infty}\left(\mathbf{C}\right)=\frac{2\mathbf{F}\partial W_{f}^{\infty}}{\partial\mathbf{C}}=2\left(C_4/\alpha_4\right)\left\{\exp\left[\alpha_4\left(I_4-1\right)\right]-1\right\}\mathbf{F}\left(\mathbf{a}_0\otimes\mathbf{a}_0\right) \tag{4.9}$$

The analytical solution of differential equations of viscous variables $\mathbf{q}^i$ is quite difficult and, therefore, numerical integration is more suitable (Simo and Hughes 1998). With regard to the uni-axial compression test along direction *i*, the relationship between nominal stress component $\mathbf{P}_i$, strain and time can be formulated as:

$$\mathbf{P}_{mv}(\mathbf{C},t) = \mathbf{P}_{mv}^{\infty}(\mathbf{C}) + \sum_{i=1}^{n} \gamma_m^j h_{mv}^i(t) \tag{4.10}$$

$$\mathbf{P}_{mi}(\mathbf{C},t) = \mathbf{P}_{mv}^{\infty}(\mathbf{C}) + \sum_{i=1}^{n} \gamma_m^j h_{mi}^i(t) \tag{4.11}$$

$$\mathbf{P}_{f}(\mathbf{C},t) = \mathbf{P}_{f}^{\infty}(\mathbf{C}) + \sum_{i=1}^{n} \gamma_f^j h_{f}^i(t) \tag{4.12}$$

The evolution of viscous variables h^i_z, with $z=mv,mi,f$, is computed by an incremental algorithm (Simo and Hughes 1998):

$$h_{mv}^i\left(t^{p+1}\right) = \exp\left\{-\frac{t^{p+1}-t^p}{\tau_m^i}\right\} h_j^i\left(t^p\right) + \frac{1}{\gamma_m^{\infty}} \exp\left\{-\frac{t^{p+1}-t^p}{2\tau_m^i}\right\}\left[P_{mv}^{\infty}\left(t^{p+1}\right) - P_{mv}^{\infty}\left(t^p\right)\right] \tag{4.13}$$

$$h_{mi}^i\left(t^{p+1}\right) = \exp\left\{-\frac{t^{p+1}-t^p}{\tau_m^i}\right\} h_j^i\left(t^p\right) + \frac{1}{\gamma_m^{\infty}} \exp\left\{-\frac{t^{p+1}-t^p}{2\tau_m^i}\right\}\left[P_{mi}^{\infty}\left(t^{p+1}\right) - P_{mi}^{\infty}\left(t^p\right)\right] \tag{4.14}$$

$$h_{f}^i\left(t^{p+1}\right) = \exp\left\{-\frac{t^{p+1}-t^p}{\tau_f^i}\right\} h_j^i\left(t^p\right) + \frac{1}{\gamma_f^{\infty}} \exp\left\{-\frac{t^{p+1}-t^p}{2\tau_f^i}\right\}\left[P_{f}^{\infty}\left(t^{p+1}\right) - P_{f}^{\infty}\left(t^p\right)\right] \tag{4.15}$$

where t^{p+1} and t^p are subsequent time steps.

For the uniaxial loading condition the deformation gradient can be assumed to be a diagonal tensor with principal stretches λ_1, λ_2, λ_3. With regard to a transversally isotropic fiber reinforced material and identifying *x* as the preferential fiber direction, the uniaxial stress states along the fibers are respectively obtained by applying deformation gradients of the type reported in the equation 4.16, where the stretch along *x* is imposed, while the other two stretches can be measured by specific optical or strain-gauge systems.

$$\mathbf{F} = \begin{bmatrix} \overline{\lambda}_x & 0 & 0 \\ 0 & \lambda_y & 0 \\ 0 & 0 & \lambda_z \end{bmatrix} \tag{4.16}$$

Accounting for the deformation gradient assumed and the orientation of fibers, the specific formulations of nominal stress components can be evaluated. With regard to the data from uniaxial tensile tests (Funk et al. 2000; Attarian et al. 1985), only the stretch along the loading direction is experimentally evaluated. On the other hand, the first Piola-Kirchhoff stress tensor defined by equation 4.3 depends on principal invariants $\tilde{I}_1, I_3, I_4$ that, in turn, are functions of all the principal stretches λ_1, λ_2, λ_3. The stretch components that are not experimentally evaluated can be calculated using analytical methods.

With regard to the specific experimental situation the axial loading direction is indicated as *i*. The stress components along the remaining directions *j* and *k* are null because of the uniaxial configuration of experimental tests, as:

$$P_{jj}\left(\lambda_i, \lambda_j, \lambda_k\right) = 0, \;\; P_{kk}\left(\lambda_i, \lambda_j, \lambda_k\right) = 0 \tag{4.17}$$

Accounting for the experimental value of stretch component $\lambda_i^{\exp}$, the solution of the algebraic non-linear system 4.17 leads to stretch components λ_j, λ_k, making it possible to evaluate the nominal stress component $P_{ii}(\lambda_i^{exp}, \lambda_j, \lambda_k)$ along the loading direction. In order to obtain a set of constitutive parameters capable of correctly interpreting the lateral behaviour of the tissue, it is necessary to introduce specific conditions on the Poisson ratios (Natali et al. 2007).

According to the large strain field assumed, tangent Poisson ratios are properly defined by the following formulation (Natali et al. 2009a):

$$\nu_{il} = -\frac{d\ln\lambda_l}{d\ln\lambda_i} = -\frac{\lambda_i}{\lambda_l}\frac{d\lambda_l}{d\lambda_i} \qquad l = j,k \tag{4.18}$$

The evaluation of the tangent Poisson moduli ν_{ij}, ν_{ik} for the experimental value of stretch component $\lambda_i^{\exp}$ requires the knowledge of the corresponding stretches λ_j, λ_k

and their first derivatives. Given the non-linear algebraic system 4.17 and an experimental value of stretch component λ_i^{exp}, accounting for regularity of functions $P_{jj}(\lambda_i, \lambda_j, \lambda_k)$ and $P_{kk}(\lambda_i, \lambda_j, \lambda_k)$, the implicit function theorem (Krantz et al. 2002) states the existence of implicit functions $\lambda_j(\lambda_i)$ and $\lambda_k(\lambda_i)$ satisfying system 4.17 for values of λ_i close to λ_i^{exp}. Furthermore, from the implicit function theorem it is possible to evaluate the derivatives of functions $\lambda_j(\lambda_i)$ and $\lambda_k(\lambda_i)$ as:

$$\begin{bmatrix} \frac{d\lambda_j}{d\lambda_i} \\ \frac{d\lambda_k}{d\lambda_i} \end{bmatrix} = -\begin{bmatrix} \frac{\partial P_{jj}}{\partial \lambda_j} & \frac{\partial P_{jj}}{\partial \lambda_k} \\ \frac{\partial P_{kk}}{\partial \lambda_j} & \frac{\partial P_{kk}}{\partial \lambda_k} \end{bmatrix}^{-1} \begin{bmatrix} \frac{\partial P_{jj}}{\partial \lambda_i} \\ \frac{\partial P_{kk}}{\partial \lambda_i} \end{bmatrix} \tag{4.19}$$

The values of stretch components λ_j, λ_k corresponding to the experimentally imposed stretch λ_i^{exp} are evaluated by solving the system 4.17, while equation 4.19 provides the derivatives. The tangent Poisson ratios υ_{ij}, υ_{ik} can, consequently, be evaluated by equation 4.18.

4.2.4 Evaluation of a preliminary set of constitutive parameters by means of analytical model

The analytical model reported in the previous paragraph is developed with regard to the fiber-reinforced visco-hyperelastic formulation and the boundary conditions of the uni-axial experimental tests, introducing some hypotheses, such as perfectly uni-axial loading condition, homogeneous stress-strain fields and uniform distribution of collagen fibers.

Preliminary sets of constitutive parameters are evaluated minimizing the cost function (4.1) that represents the discrepancy between the analytical model and the experimental data. This step leads to the identification of the preliminary sets $\boldsymbol{\omega}_0^{\,i}$ (apex i specifies the ligament).

In detail the analyses consider the experimental data of Funk et al. (2000) that developed high strain rate tests to evaluate the mechanical response of instantaneous ankle ligaments, and that of Attarian et al. (1985a) that performed elongation tests at two different strain rates, as 5 cm/sec and 0.01 cm/sec. To analyze the two kind of

experimental tests, the fiber-reinforced hyperelastic and the fiber-reinforced visco-hyperelastic formulation is adopted, respectively. In detail, the experimental data reported by Funk et al. 2000 are adopted to evaluate the hyperelastic parameters. While the experimental data obtained at low strain rate (Attarian et al. 1985) are adopted to assess the reliability of the achieved hyperelastic parameters and to evaluate the viscous ones.

The parameters achieved until now are used as starting point in the procedure that minimize the discrepancy between experimental data and analytical model results. In this case both experimental data are compared with fiber-reinforced visco-hyperelastic model results. The minimization determines the preliminary sets of constitutive parameters $\boldsymbol{\omega}_0^i$. With regard to the hyperelastic parameters, the analyses performed show that the same ground matrix parameters (Table 1) can be assumed for all the ligaments with adequate accuracy.

Kv (MPa)	*r*	C_1 (MPa)	α_1
5.844	4.170	0.161	0.140

Table 4.1. Hyperelastic parameters of ground matrix contribution obtained from the comparison between experimental data and analytical model results

On the other hand, different hyperelastic fiber parameters (Table 4.2) are assumed.

	C_4 (MPa)	α_4
ATFL	0.177	3.701
CFL	0.193	12.074
PTFL	0.098	17.011
TCL	0.073	22.073
PTTL	0.361	12.059
ATTL	0.663	8.484
ATiFL	0.740	9.536
PTiFL	1.047	7.688

Table 4.2. Hyperelastic parameters of the fibers contribution obtained from the comparison between experimental data and analytical model results

The results can be interpreted assuming that all the ankle ligaments are composed by similar ground matrix, and the different mechanical responses are due to different collagen fiber conformations. As reported in Chapater 3, C_4 is related to the initial stiffness of the fibers contribution as $E_f=4C_4$ while α_4 depends on the initial fibers wavy conformation. In detail the more collagen fibers present crimped configuration the higher the value of α_4 is, this matches to a more significant non linearity of the stress-strain response. While the more rigid (ore dense) fibers are the higher the value of C_4 is. This assumption is enforced by the evaluation of viscous parameters, performed by the analysis of tests on ATFL and CFL only. The results show that the stress-strain curves at different strain rates of both ligaments can be interpreted by assuming the same viscous parameters reported in Table 4.3. In fact, the same viscous processes develop within the different ligaments.

τ_m (s)	γ_m	τ_f (s)	γ_f
0.201	0.787	0.146	0.156

Table 4.3. Viscous parameters of ground matrix and fibers contribution obtained from the comparison between experimental data and analytical model results

In Figure 4.1 the comparison between the experimental data reported by Attarian et al. (1985) and analytical model results are reported.

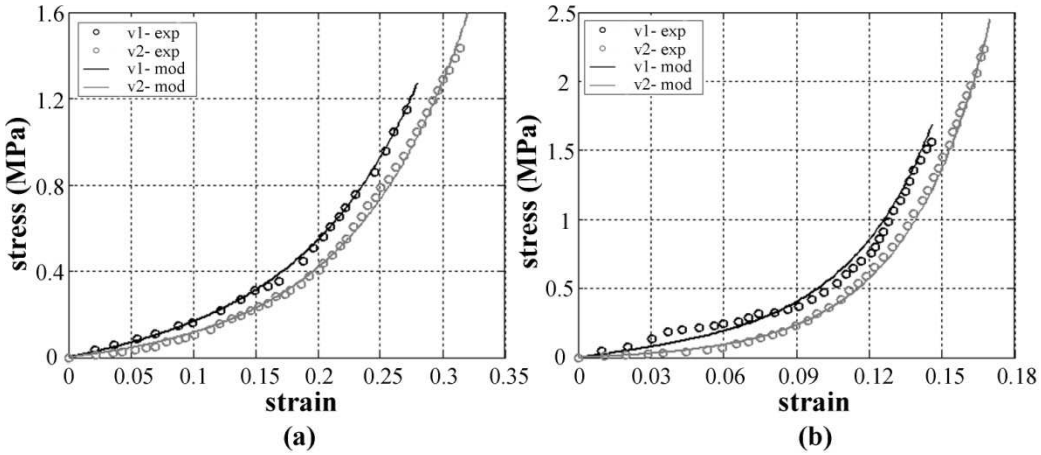

Figure 4.1. Comparison between analytical model results (continuous line) and experimental data (circles) of the ATFL (a) and CFL (b) for two different strain rates: v1= 5cm/sec and v2= 0.01cm/sec (Attarian et al. 1985a)

In Figure 4.2 the comparison between the experimental data reported by Funk et al. (2000) and analytical model results are reported.

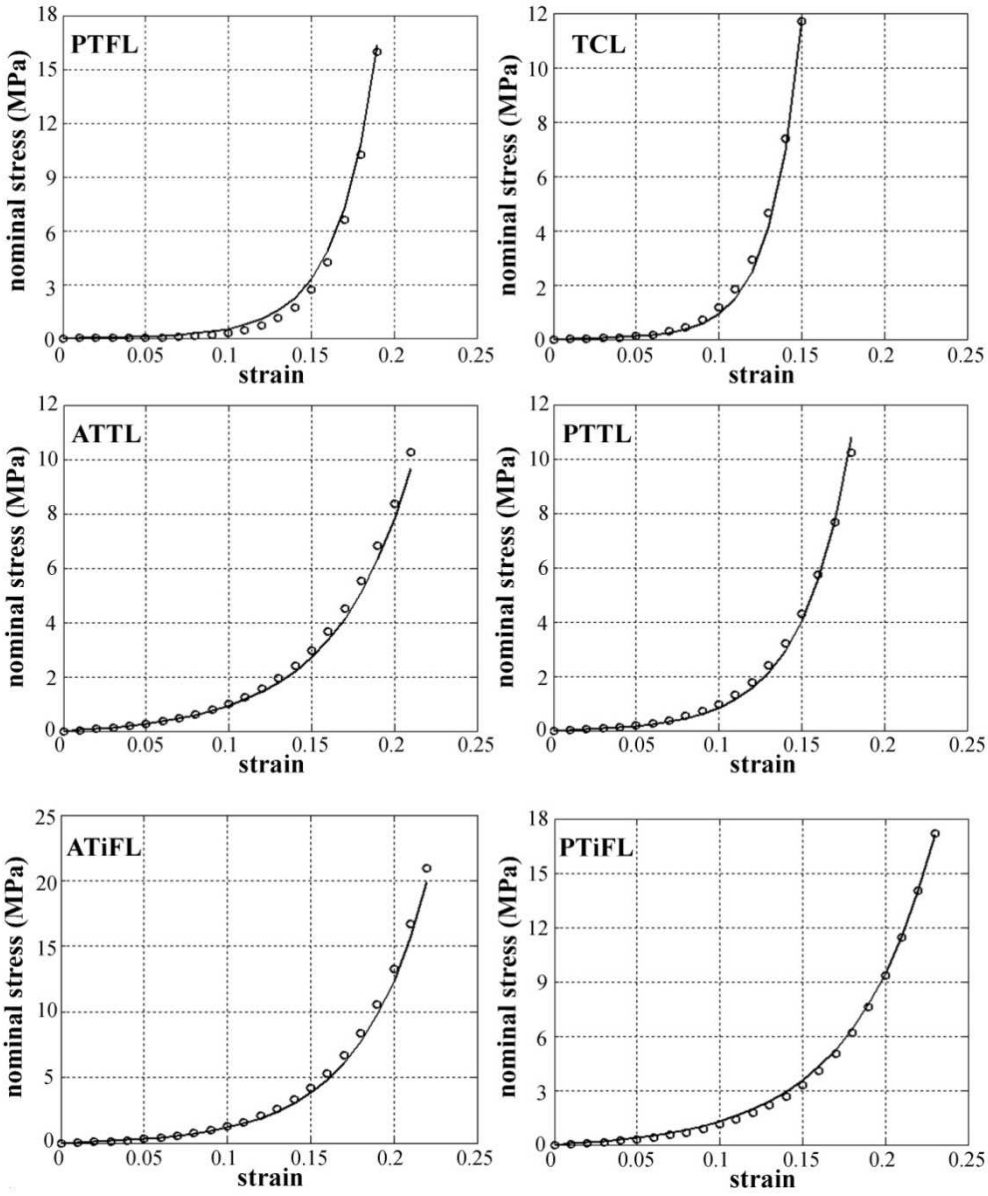

Figure 4.2. Comparison between analytical model and experimental (circles) results of the PTFL, TCL, ATTL, PTTL, ATiFL and PTiFL ligament (Funk et al. 2000)

As shown in Figure 4.1 and 4.2 the constitutive parameters obtained through the analytical approach allow to achieve a good agreement between experimental and model results.

In spite of this, the analytical model that is developed not accounting for the real geometry of the specimen and introducing some hypotheses, such as perfectly uni-axial loading condition, homogeneous stress-strain fields and uniform distribution of collagen fibers.

Numerical methods do not present such limitations, and experimental conditions can be analysed with greater accuracy. It follows the necessity to upgrade the constitutive parameters trough numerical analyses.

4.2.5 Upgrading the constitutive parameters by means of numerical model

As reported before, the main limitations of the analytical model pertain to the assumptions of uni-axial stress configuration, uniform stress and strain fields and homogenous distribution of fibers directions. Such assumptions affect the quality of the achieved parameters ω_0^i and is overcome by numerical models, which allow to consider the actual configuration of experimental samples and boundary conditions (Attarian et al. 1985; Funk et al. 2000).

For this purpose specific numerical model of each experimental sample is developed, considering the actual geometry of the bone-ligament-bone specimens. The details of the procedure adopted to define the numerical model are reported in Chapter 3.

The mechanical behaviour of bone tissue is characterized by orthotropic linearly elastic formulation (Natali et al. 2010a), while the fiber reinforced visco-hyperelastic formulation has been adopted to characterise the mechanical behaviour of the ligaments. Constitutive models are implemented by a user subroutine in a general purpose Finite Element software (ABAQUS 6.8, Simulia, Dassault Systèmes, Providence, RI, USA).

Concerning the experimental set-up, the elongation of the ligament is applied by fixing a bone element and imposing a displacement to the other bone. The displacement is imposed along the principal direction of the fibers of the ligament.

In Figure 4.3 the numerical models used to simulate the experimental tests are reported.

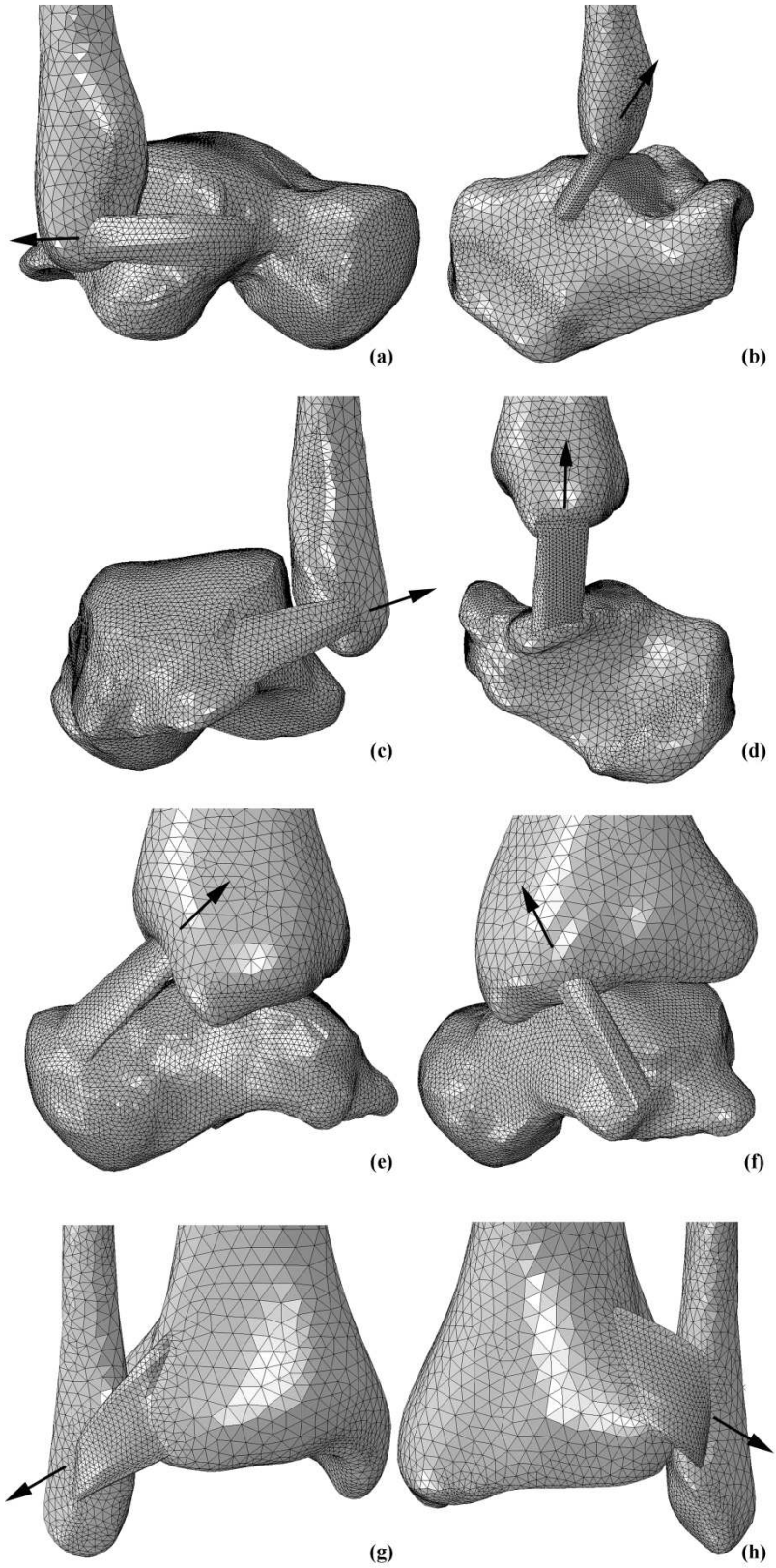

Figure 4.3. Numerical models of specimens: (a) talus – ATFL - fibula, (b) calcaneus – CFL – fibula, (c) talus-PTFL-fibula, (d) talus – TCL – tibia, (e) talus – ATTL – tibia, (f) talus – PTTL – tibia, (g) fibula – ATiFL – tibia and (h) fibula – PTiFL – tibia. The arrows indicate the direction of the load

4.2.5.1 Definition of the direction of collagen fibers

With regard to the histological analysis a fundamental feature of the ligaments of the hindfoot is the distribution of collagen fibers along a preferential direction. To introduce this characteristics in the numerical model (Figure 4.4) a specific procedure has been defined.

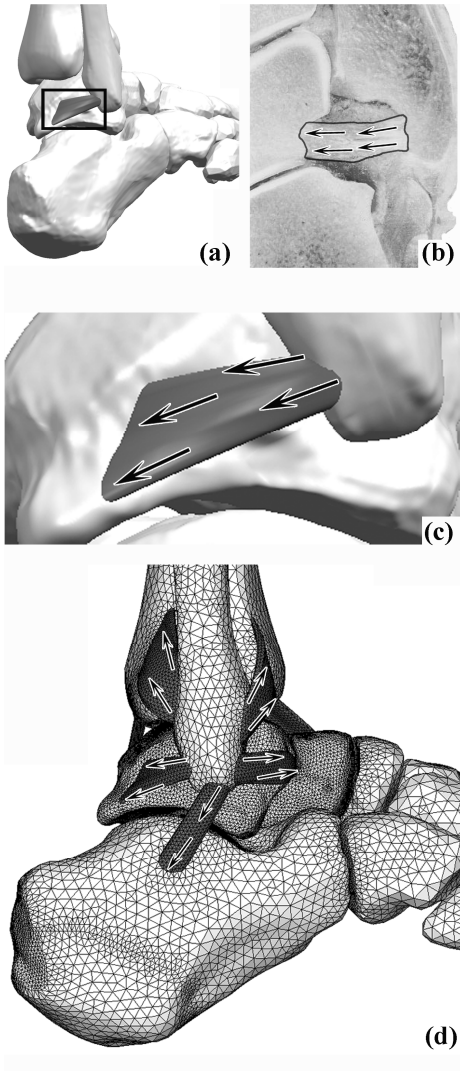

Figure 4.4. Representation of the direction of ankle ligament fibers: (a) solid model of the ankle structure, (b) detail of the histology of the PTFL ligament, (c) detail of fiber distribution in the PTFL solid models and (d) representation of the directions of fibers in ankle ligaments

To this purpose different steps are performed. The procedure starts by processing the solid model of each ligament using UGS software. Two sections that represent the distal and the proximal insertion areas are defined. Furthermore, the body of each

ligament is divided in several transversal sections and the centroid of each section is evaluated (Figure 4.5).

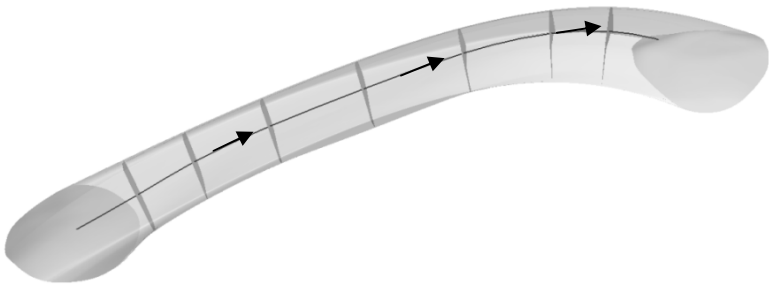

Figure 4.5. Schematic representation of the spline that joins the centroid of each section of the ATFL ligament. The arrows indicates the tangent vector in different point of the curve

The coordinates of the centroid of the *n* section are reported as a sequence of points ($P_{o(x,y,z)}$ …. $P_{n(x,y,z)}$) into the Matlab software and are interpolated with a poly-line.
To determine the orientation of the fibers, the tangent vector of each point of the poly-lines is evaluated.
An ad hoc routine is developed which is able to interpret the behaviour of the ligament tissues with a fibrer reinforced visco-hyperelastic formulation and to assign the specific orientation of each point of the ligament on the basis of histological data reported in literature (Kumai et al. 2002; Keller et al. 2010). In detail, for each Gauss point of the model the orientation of the fibers is defined to be equal to the orientation of the nearest point of the poly-lines.
When the geometry of the ligament is complex and the insertion areas of the same ligament are very different another procedure is adopted. The fiber distribution within the ligament is evaluated through unit vectors that specify the local fiber direction in a set of points within the ligament. Coordinate points and corresponding vector components are collected in a matrix. The fiber vector of a given point within the ligament is computed by averaging fiber vectors of the three closest points whose information are collected within the matrix.
An example of local fibers distribution is reported in Figure 4.6.

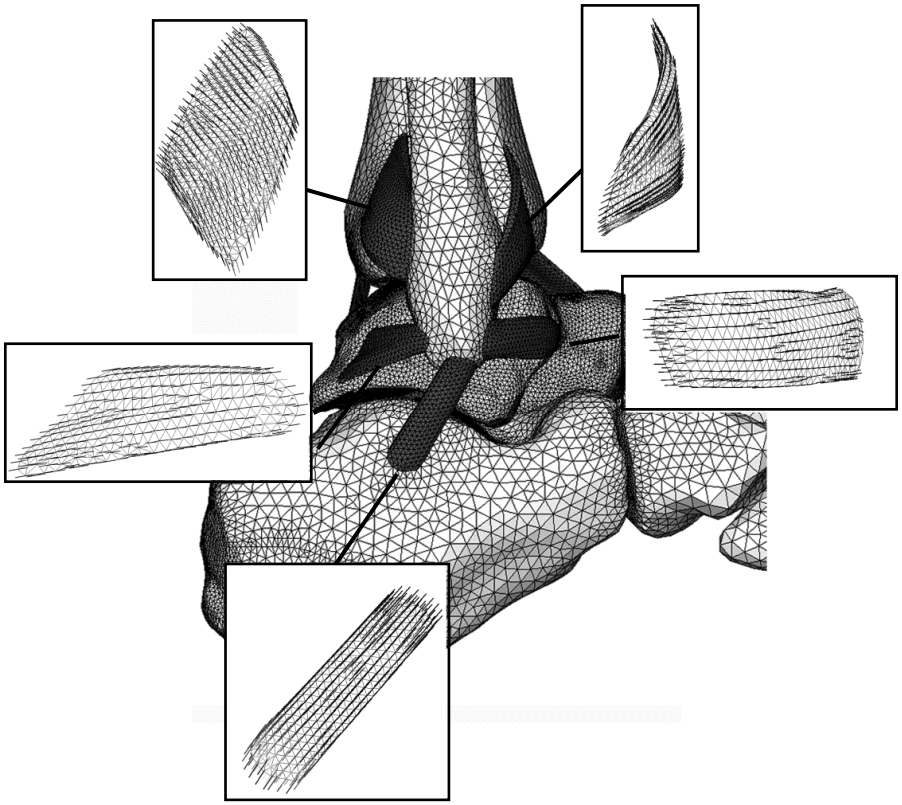

Figure 4.6. Distribution of the collagen fibers in the ligaments of the lateral side of the ankle. In detail for each Gauss point is reported the vector that indicates the local direction of the fibers of the ligaments

4.2.5.2 Comparison between experimental data and numerical model results

Numerical analysis is performed for each ligament assuming different sets of parameters $\boldsymbol{\omega}_k^i$ starting from the parameters $\boldsymbol{\omega}_0^i$ that are achieved with the analytical approach. In detail only fibers hyperelastic parameters (C_4 and α_4) are changed up to convergence of numerical and experimental results.

The procedure provides an evaluation of the discrepancy between experimental data and numerical model results for the different sets of parameters investigated. The discrepancy is evaluated using the previously reported cost function (4.1), whose minimization lead to the optimal set of the constitutive parameters.

The numerical analyses lead to the optimal sets of parameters that describe the mechanical properties of each ankle ligaments $\boldsymbol{\omega}^i$ (Table 4.4) and confirm the previous assumptions about the parameters themselves.

	C_4 (MPa)	α_4
ATFL	0.266	5.181
CFL	0.093	8.874
PTFL	0.133	14.248
TCL	0.093	26.623
PTTL	0.917	11.398
ATTL	0.266	10.362
ATiFL	1.462	6.735
PTiFL	2.658	8.290

Table 4.4. Upgrading of the hyperelastic parameters of fiber contribution obtained from the comparison between experimental data and numerical model results

It is important to emphasize that the numerical approach is not used to improve the fitting of the experimental results, but to improve the reliability of the constitutive parameters. The stress state within the ligament during the experimental tests is not uniaxial and homogeneous, as it is assumed within analytical formulations. Numerical analyses account for the actual geometry of the specimens and the real stress configuration.

The comparison between the experimental data and numerical model results for the lateral collateral ankle ligaments are reported in Figure 4.7.

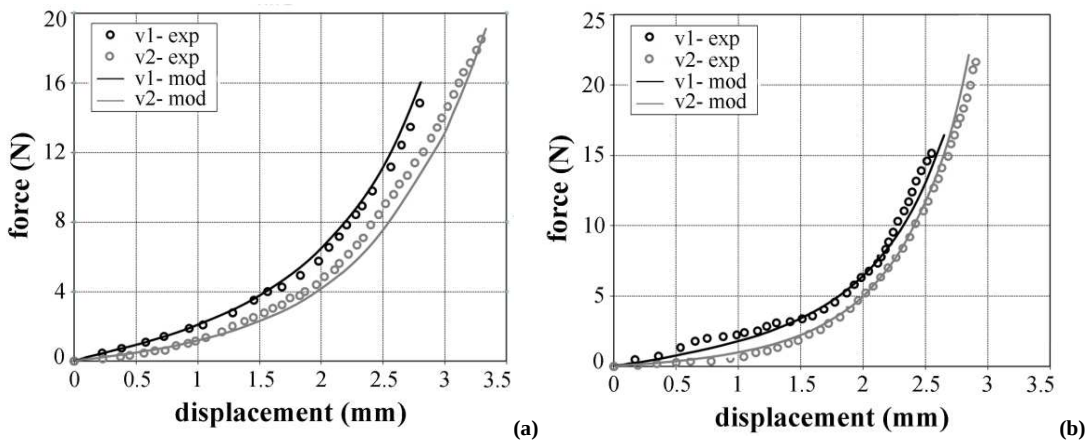

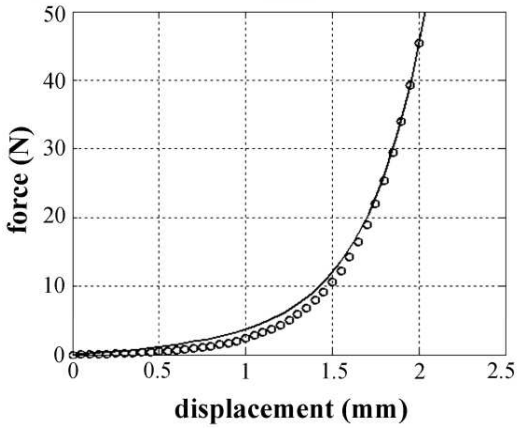

Figure 4.7. Comparison between numerical model results (continuous line) and experimental data (circles) of the lateral-collateral ankle ligaments: (a) ATFL (v1=5cm/sec, v2=0.01 cm/sec), (b) CFL v1=5cm/sec, v2=0.01 cm/sec) and (c) PTFL (28 cm/sec)

The comparison between the experimental data and numerical model results for the lateral collateral ankle ligaments are reported in Figure 4.8 and Figure 4.9.

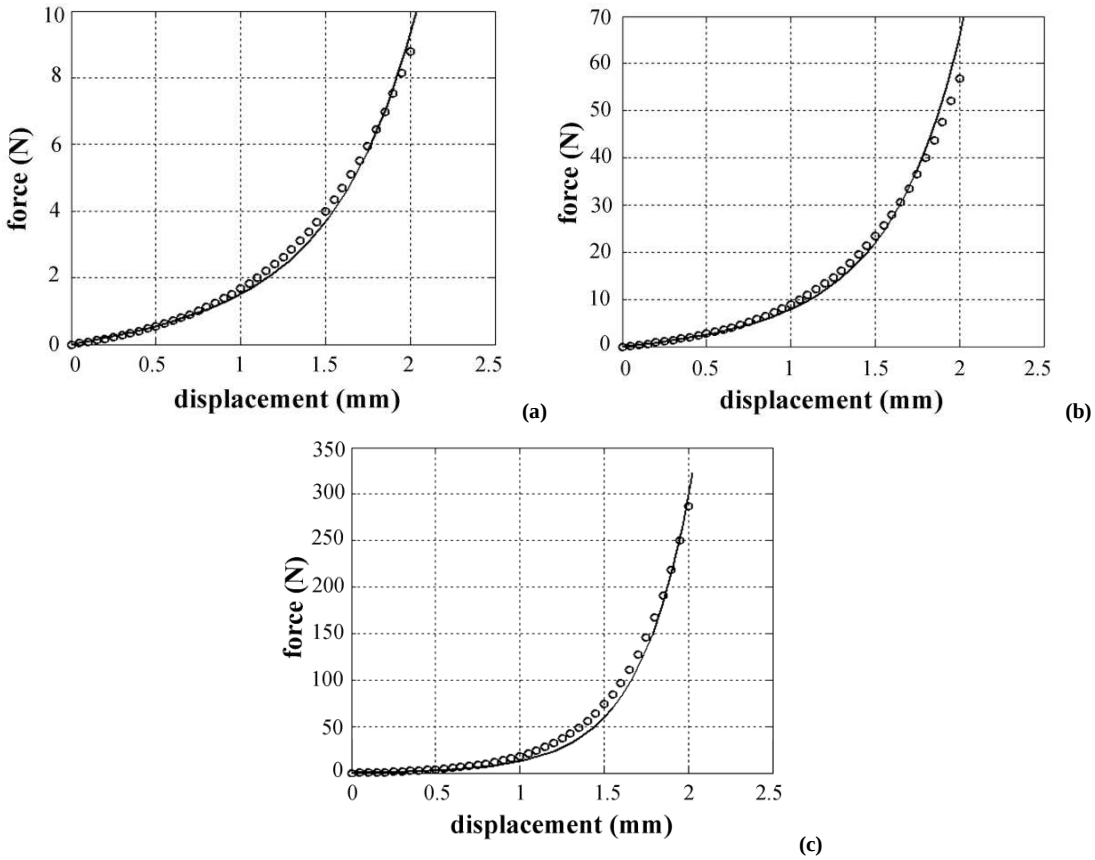

Figure 4.8. Comparison between numerical model results (continuous line) and experimental data (circles) of the deltoid ligaments at 28 cm/sec: (a) TCL, (b) ATTL and (c) PTTL

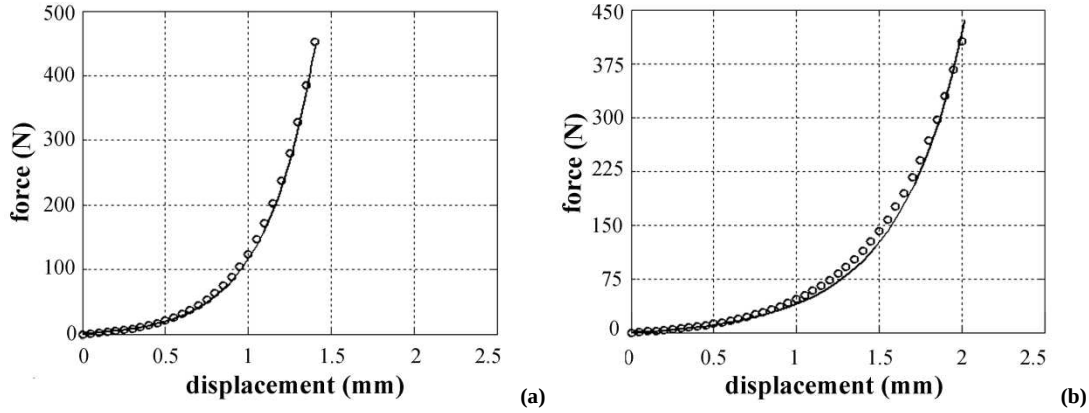

Figure 4.9. Comparison between numerical model results (continuous line) and experimental data (circles) of ligaments that join the distal epiphyses of the tibia and fibula at 28 cm/sec: (a) ATiFL and (b) PTiFL

With regard to the ligaments of the subtalar joint no experimental data that allow the evaluation of constitutive parameters have been published, to the author's knowledge. Nevertheless, same authors (Imhauser 2004) confirm that the subtalar ligaments appear to have similar physical structures to the ATFL. With these assumptions in mind, it is possible to assign to the subtalar ligaments the same constitutive parameters of the ATFL.

	Hyperelastic parameters						Viscous parameters			
	K_v (MPa)	r	C_1 (MPa)	α_1	C_4 (MPa)	α_4	τ_m (sec)	γ_m	τ_f (sec)	γ_f
INTRA	5.844	4.170	0.161	0.140	0.266	5.181	0.201	0.787	0.146	0.156
CERV	5.844	4.170	0.161	0.140	0.266	5.181	0.201	0.787	0.146	0.156

Table 5.7. Hyperelastic and viscous parameters of the subtalar ligaments

4.3 References

Araújo A.L., Mota Soares C.M., Moreira de Freitas M.J., 1996. Characterization of material parameters of composite plate specimens using optimization and experimental vibrational data, Composites: Part B, vol. 27, pp. 185-191.

Attarian D.E, McCrackin H.J., DeVito D.P., McElhaney J.H., Garrett W.E., 1985. Biomechanical characteristis of human ankle ligaments, Foot & Ankle, vol. 6(2), pp. 54-58.

Begambre O., Laier J.E., 2009. A hybrid particle swarm optimization – simplex algorithm (PSOS) for structural damage identification, Advances in Engineering Software, vol. 40(9), pp. 883-891.

Boukari D., Fiacco A.V., 1995. Survey of penalty, exact-penalty and multiplier methods from 1968 to 1993, Optimization, vol. 32, pp. 301–334.

Carniel E.L., 2006. Formulation of constitutive models for the analysis of the mechanical behaviour of soft biological tissues. Doctoral thesis of Padua University.

Cash D.M., Miga M.I., Sinha T.K., Galloway R.L., Chapman W.C., 2005. Compensating for Intraoperative Soft-Tissue Deformations Using Incomplete Surface Data and Finite Elements, Ieee transactions on medical imaging, vol. 24 (11), 1479-91.

Corana A., Marchesi M., Martini C., Ridella S., 1987. Minimizing multimodal functions of continuous variables with the "Simulated Annealing" algorithm, ACM Transactions on Mathematical Software, vol. 13, pp. 262-280.

Crowninshield R. D. and Brand R. A., 1981. A physiologically based criterion of muscle force prediction in locomotion, Journal of Biomechanics, vol. 14, pp. 793–801.

Funk J.R., Hall G.W., Crandall J.R., Pilkey W.D., 2000. Linear and quasi linear viscoelastic characterization of ankle ligaments, Journal of Biomechanical Engineering, vol. 122, pp. 15-22.

Grédiac M., Toussaint E., Pierron F., 2002. Special virtual fields for the direct determination of material parameters with the virtual fields method. 1 – Principle and definition, International Journal of Solids and Structures, vol. 39, pp. 2691-2705.

Hillstrom, K.E., 1977. A simulation test approach to the evaluation of nonlinear optimization algorithms, T. Math. Software, vol. 3, pp. 305-315.

Imhauser C.W., 2004. The development and evaluation of a 3 dimensional, image-based, patient-specific, dynamic model of the hindfoot, Drexel University.

Keller K., Nasrilari M., Filler T., Jerosch J., 2010. The anterior tibio-talar ligament: one reason for anterior ankle impingement, Knee Surgery, Sports Traumatology, Arthroscopy, vol. 18, pp. 225–232.

Kirkpatrick S., Gelatt C.D., Vecchi M.P., 1983. Optimization by simulated annealing, Science, vol. 220, pp. 671-679.

Krantz S.G., Parks H.R., The Implicit Function Theorem: History, Theory, and Applications, Birkhäuser, Boston, 2002.

Kumai T., Takakura Y., Rufai A., Milz S., Benjamin M., 2002. The functional anatomy of the human anterior talofibular ligament in relation to ankle sprains, Journal of Anatomy, vol. 200, pp. 457-465.

Kyriacou S.K. and Davatzikos C., 1998, A biomechanical model of soft tissue deformation, with applications to non-rigid registration of brain images with tumor pathology, Lecture Notes in Computer Science, vol. 1496, pp. 531-538.

Lagarias, J.C., J.A. Reeds, M. H. Wright and P. E. Wright, 1998. Convergence properties of the Nelder Mead simplex method in low dimensions, SIAM Journal on Optimization, vol. 9, pp. 112-147.

Lei F., Szeri A.Z., 2007. Inverse analysis of constitutive models: biological soft tissues, Journal of Biomechanics, vol. 40 (4), pp. 936-940.

Metropolis N., Rosenbluth A., Rosenbluth M., Teller A., Teller E., 1953. Equation of state calculations by fast computing machines, Journal of Chemical Physics, vol. 21, pp. 1087-1090.

Natali A.N., Carniel E.L., Gregersen H., 2009a. Biomechanical behaviour of oesophageal tissues: material and structural configuration, experimental data and constitutive analysis, Medical Engineering & Physics, vol. 31, pp. 1056-1062.

Natali A.N., Carniel E.L., Pavan P.G., 2010a. Modelling of mandible bone properties in the numerical analysis of oral implant biomechanics, Computer Methods and Programs in Biomedicine, vol. 100(2), pp. 158-165.

Natali A.N., Carniel E.L., Pavan P.G., Dario P., Izzo I., 2006. Hyperelastic models for the analysis of soft tissue mechanics: definition of constitutive parameters, proceedings of BioRob2006, Pisa (I), pp. 1-4.

Natali A.N., Fontanella C.G., Carniel E.L., Miller-Young J., 2010b. Biomechanical behaviour of heel pad tissues: experimental testing, constitutive formulation and numerical modeling, Proceedings of the Institution of Mechanical Engineers, Part H, Journal of Engineering in Medicine, vol. 225, pp. 449-459.

Natali A.N., Forestiero A., Carniel E.L., 2009b. Parameters identification in constitutive models for soft tissues mechanics, Russian journal of Biomechanics, vol. 4(46), pp. 29-39.

Natali, A.N., Carniel, E.L., Pavan, P.G., Bourauel C., Ziegler A., Keilig L., 2007. Experimental–numerical analysis of minipig's multi-rooted teeth, Journal of Biomechanics, vol. 40, pp. 1701-1708.

Praagman M., Chadwick E.K.J., Van der Helm F.C.T., Veegera H.E.J., 2006. The relationship between two different mechanical cost functions and muscle oxygen consumption, Journal of Biomechanics, vol. 39, pp.758–765.

Simo, J.C., Hughes, T.J.R., 1998. Computational Inelasticity, Springer, New York.

Stoer J., Bulirsch R., 1992. Introduction to numerical analysis (second edition), Springer-Verlag, New York.

Stokes I.A.F., Gardner-Morse M., 2001, Lumbar spinal muscle activation synergies predicted by multi-criteria cost function, Journal of Biomechanics, vol.3, pp 733–740.

CHAPTER 5

RESULTS OF NUMERICAL ANALYSES AND EVALUATION OF THE BIOMECHANICAL BEHAVIOUR OF THE ANKLE LIGAMENTS DURING FOOT MOTION

5.1 Introduction

With the aim of understanding the mechanical properties of the ligaments that cannot be observed during the experimental tests, in this chapter are reported the results of the numerical analyses that interpret the tensile test on bone-ligament-bone specimens. The constitutive characterisation of the hindfoot ligaments tissues, by means of the definition of mathematical constitutive laws and the evaluation of constitutive parameters, must be followed by the evaluation of the biomechanical behaviour of the ligaments during the motion of the foot. This task can be performed by analysing in vitro experimental tests that measured the strain of the central part of the ankle ligaments during the dorsiflexion and plantarflexion of the foot. Numerical analyses that interpret this experimental condition are performed. A comparison between the results of experimental tests and numerical models has been carried out and the stress fields are reported. A high correlation between numerical and experimental results has been achieved, demonstrating the reliability of the proposed formulations. A numerical analysis that interprets the characteristic phenomenon of inversion of the ankle joint is also reported. This kind of work is the basis for the biomechanical evaluation of the ankle and subtalar joint with intact ligaments and after the rupture of some of them. At this purpose in literature there are several experimental tests that evaluate the biomechanical behaviour of the hindfoot joints with intact ligaments and after the serial sectioning of some of them.

5.2 Analysis of the mechanical behaviour of the ankle ligaments during uni-axial tensile tests

As reported in Chapter 4 numerical analyses that reproduce the uni-axial tensile tests (Funk et al. 2000; Attarian et al. 1985) on the ankle ligaments are performed. The analyses considered all the boundary conditions of the experimental tests. With reference to the experimental set-up, elongation of the ligament is applied by fixing a bone element and imposing a displacement to the other bone element along the principal direction of the fiber ligament itself.

5.2.1 Displacement and stress field

The contours of the displacement and maximum principal stress field are reported for each ligament. Because ligaments have very different geometry from each other, to compare the numerical results, the biomechanical responses corresponding to a strain of 12% are reported. As shown in Figure 5.1 this value is attained by all the ligaments.

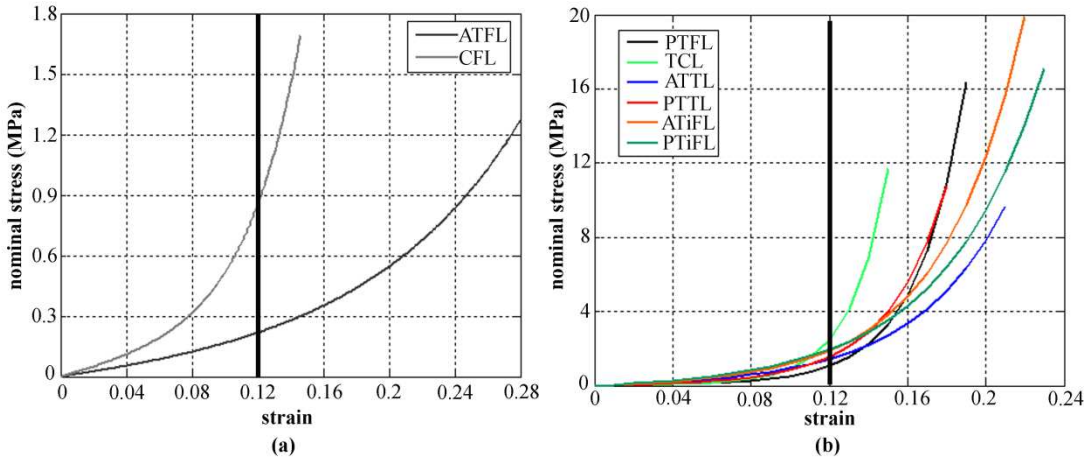

Figure 5.1. Comparison between the stress-strain behaviour of each ankle ligament: experimental results obtained by Attarian et al. 1985at v= 5 cm/sec (a) and Funk et al. 2000 at 28 cm/sec (b)

With regard to the tests performed by Attarian et al. 1985, with a strain equal to 12 %, the ligament that presents a major level of stress is the CFL. In the work of Funk et al. 2000 the ligament that presents the minimum stress is the ATTL, while the ligament that presents the maximum stress is the TCL. The contours of the stress and

displacement field obtained by the numerical analyses are reported in the following figures.

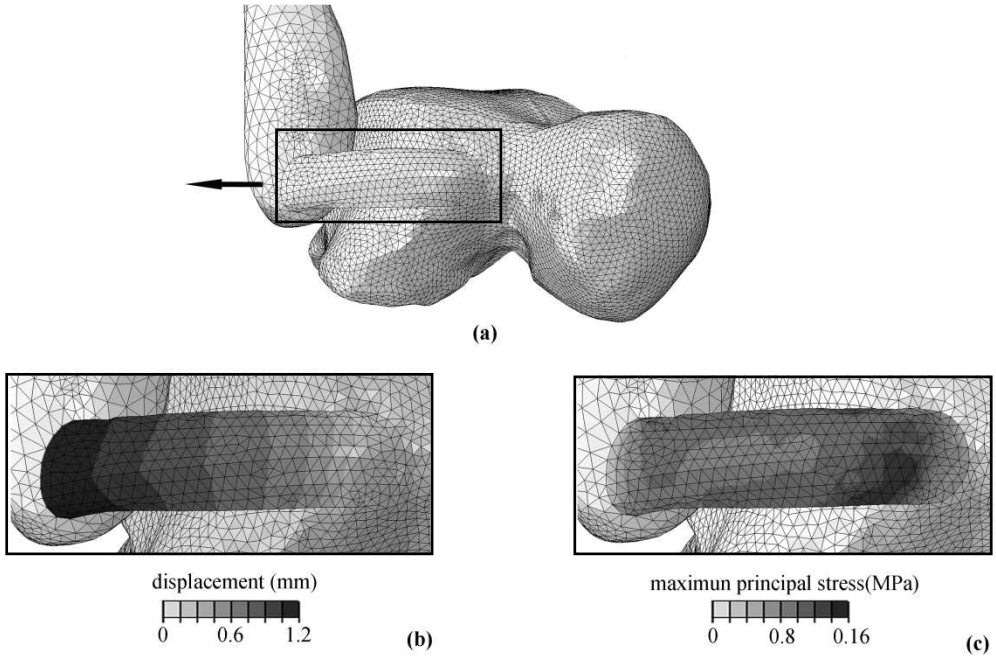

Figure 5.2. Numerical model results: numerical model (a), detail of the displacement (b) and maximum principal stress field (c) of the ATFL (v= 5 cm/sec)

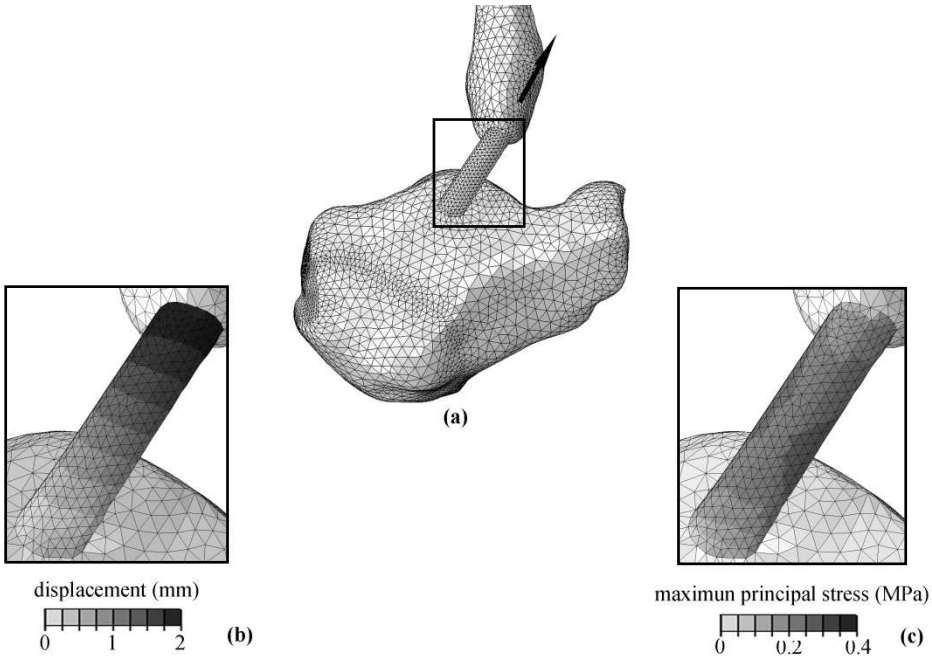

Figure 5.3. Numerical model results: numerical model (a), detail of the displacement (b) and maximum principal stress field (c) of the CFL (v=5 cm/sec)

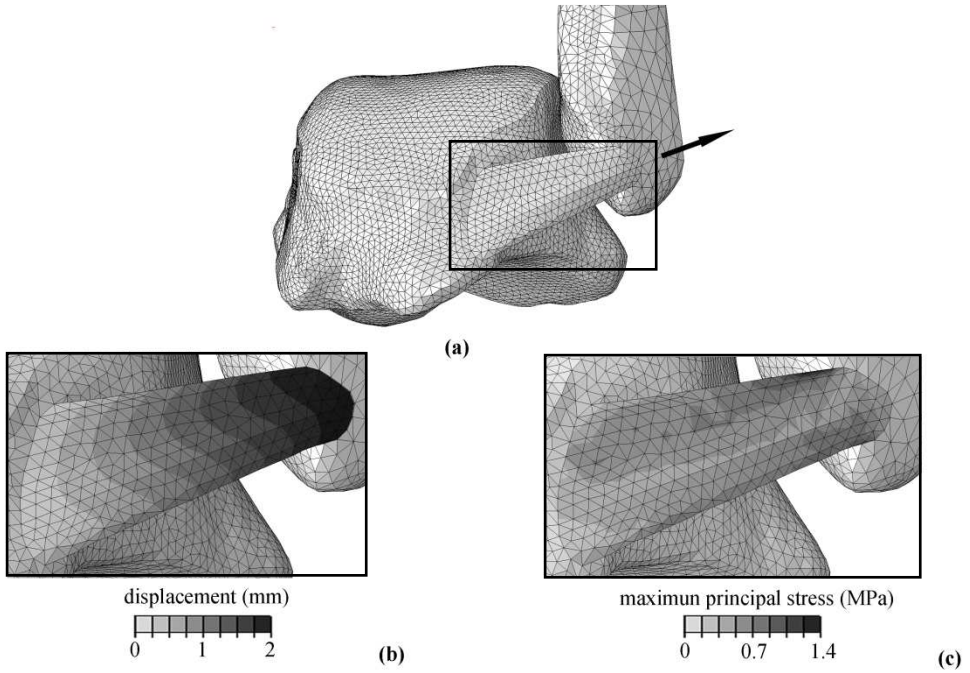

Figure 5.4. Numerical model results: numerical model (a), detail of the displacement (b) and maximum principal stress field (c) of the PTFL

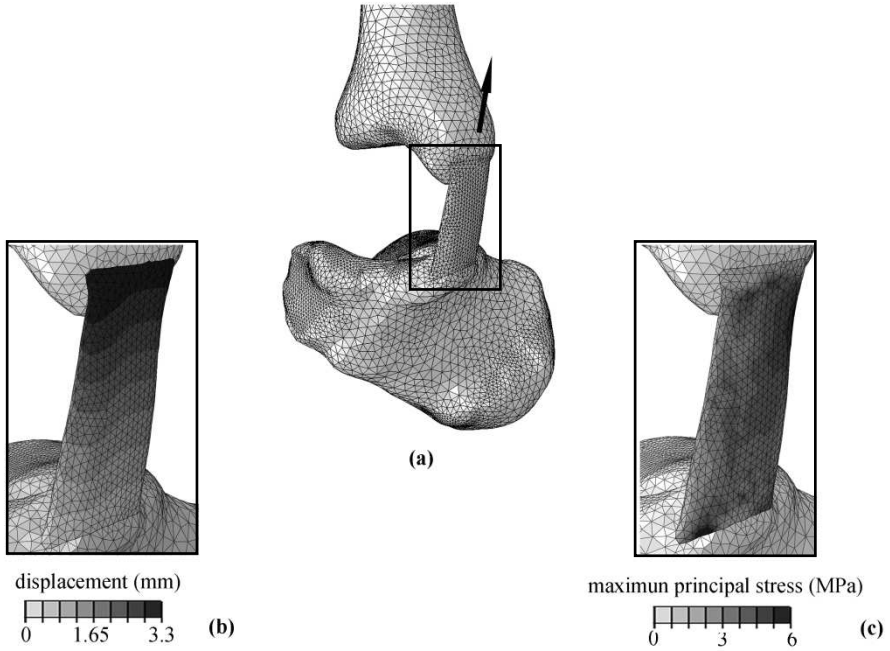

Figure 5.5. Numerical model results: numerical model (a), detail of the displacement (b) and maximum principal stress field (c) of the TCL

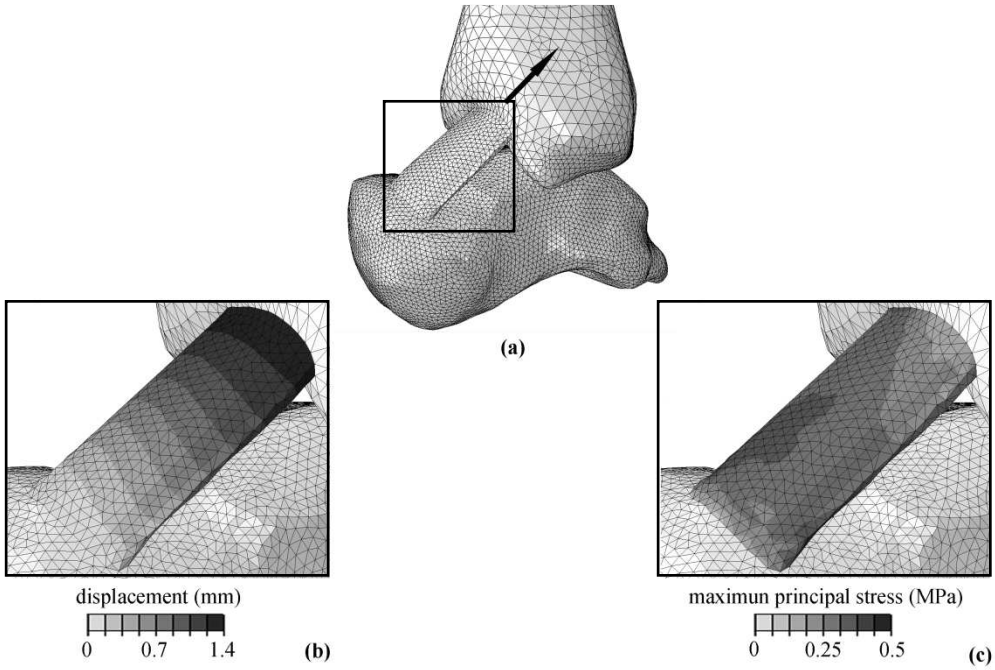

Figure 5.6. Numerical model results: numerical model (a), detail of the displacement (b) and maximum principal stress field (c) of the ATTL

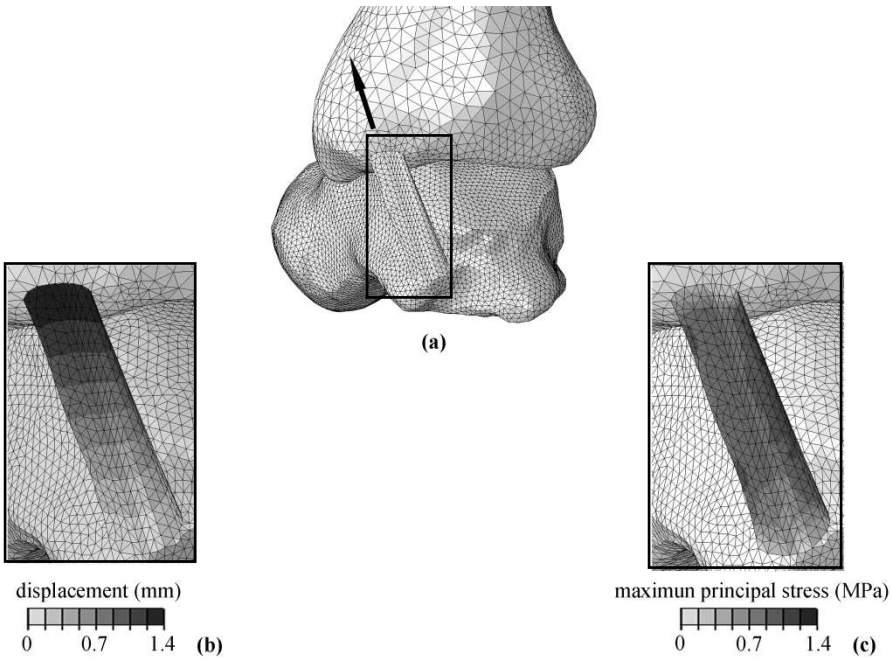

Figure 5.7. Numerical model results: numerical model (a), detail of the displacement (b) and maximum principal stress field (c) of the PTTL

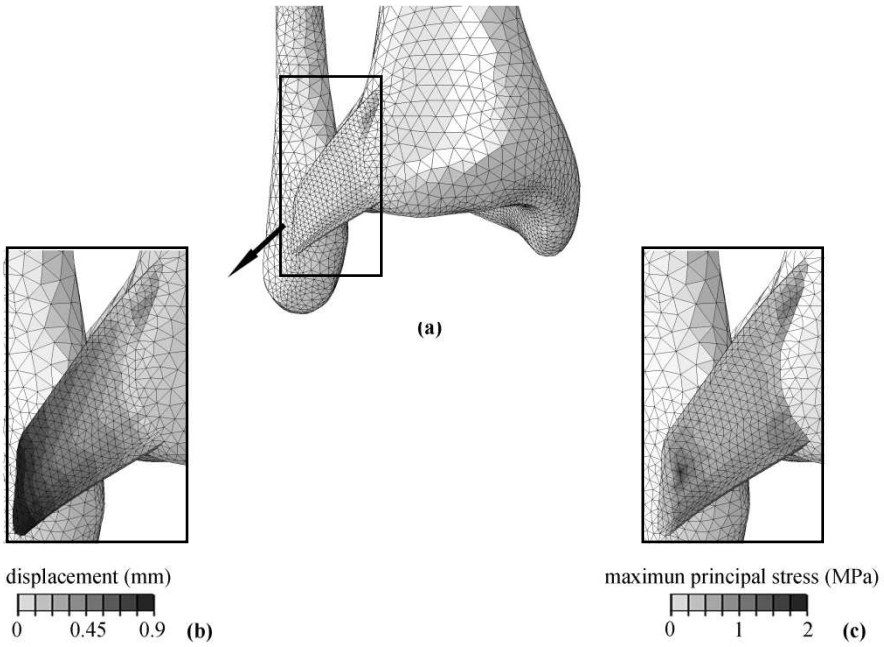

Figure 5.8. Numerical model results: numerical model (a), detail of the displacement (b) and maximum principal stress field (c) of the ATiFL

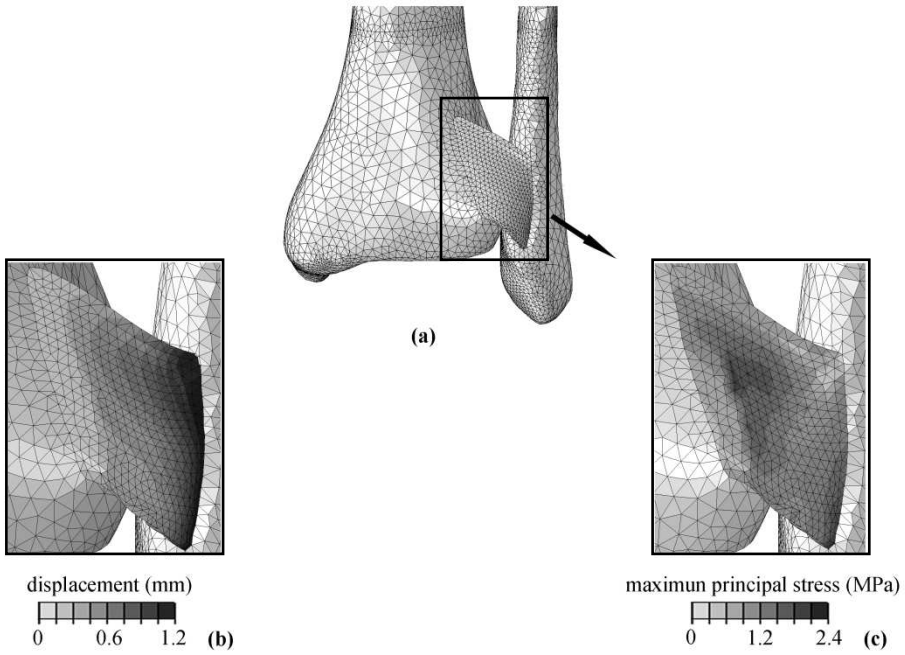

Figure 5.9. Numerical model results: numerical model (a), detail of the displacement (b) and maximum stress field (c) of the PTiFL

5.3 Numerical analyses of the ankle ligaments during dorsiflexion and plantarflexion movements

The validation of the procedure adopted for the evaluation of the constitutive parameters is performed by the analysis of experimental situations that have not been accounted in the evaluation of constitutive parameters.

For this purpose the *in vitro* experimental tests reported by Ozeky et al. (2002) are investigated. The authors measured the strain changes of the central part of the anterior talofibular ligament (ATFL), the posterior talofibular ligament (PTFL), the calcaneofibular ligament (CFL) and the tibiocalcaneal ligament (TCL) during the dorsiflexion and plantarflexion movements of the ankle. A fresh frozen amputated ankle was used and all muscles, tendons, nerves and vessels were removed from the specimen keeping intact the ligaments and the capsular structure of the ankle. The sole of the foot was placed on the testing table with an elastic band while the tibia was moved manually to perform dorsiflexion and plantarflexion. An axial loading force was not applied.

The experimental tests are interpreted by numerical analyses on the hindfoot. As reported in Chapter 3, the numerical models of the hindfoot are obtained from the solid model using MSC-Patran software (MSC.Software Corporation, Santa Ana, CA). Bones and soft tissue regions are meshed with linear tetrahedral elements.

With regard to the mechanical characterization of the tissues involved, the bony segments are assumed to be orthotropic and linearly elastic (Natali et al. 2010a) while the ligaments tissues are described with the visco-hyperelastic constitutive model and the constitutive parameters obtained beforehand.

With reference to the experimental set-up, experimental boundary conditions are applied by fixing the calcaneus and imposing a rotation of the tibia and fibula around the intermalleolar axis. As reported in the literature (Siegler et al. 2005), this axis is defined as the line that joins the medial and the lateral malleolus.

A schematic representation of the numerical model and the boundary condition applied is reported in the Figure 5.10.

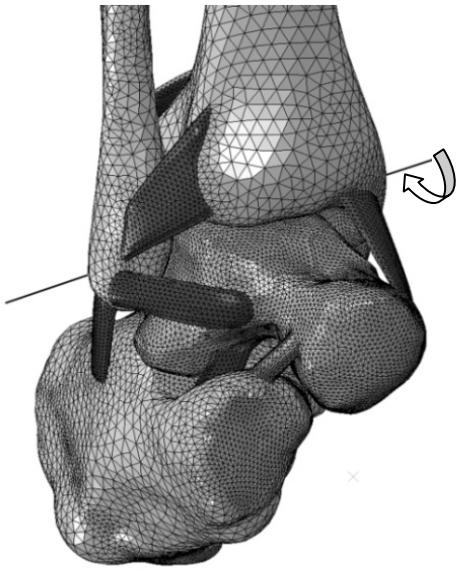

Figure 5.10. Numerical model of the hindfoot for the evaluation of the biomechanical behaviour of the ankle ligaments during dorsiflexion and plantarflexion movements

5.3.1 Comparison between numerical and experimental results

The numerical results are compared with the experimental data reported by Ozeky et al. 2000.

In Figure 5.11 the flexion angle-strain curves of the ATFL, PTFL, CFL and TCL are shown. The strain of the ligament (%) reported in the following graphs are evaluated as $(L_q - L_n)/(L_n)$ where L_q indicates the ligament length at q (°) of ankle dorsi-plantar flexion, while L_n indicates the length of each ligament at the neutral position. The numerical results are reported in a physiological range.

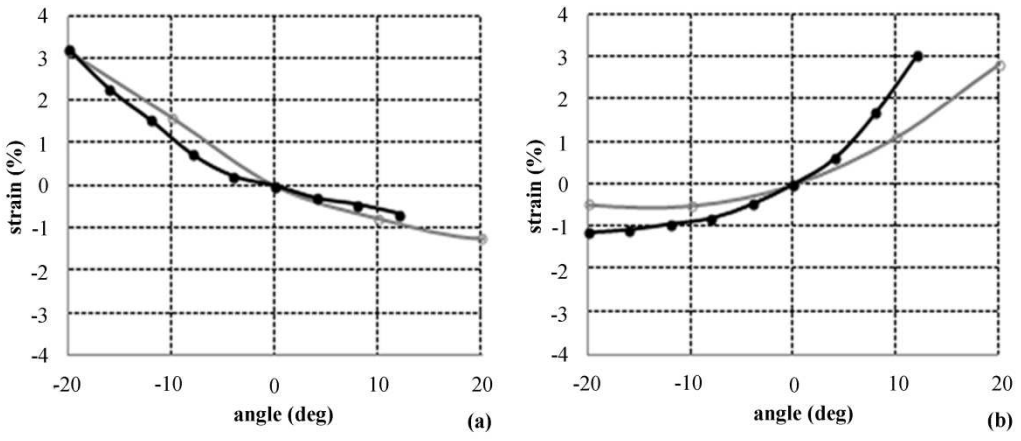

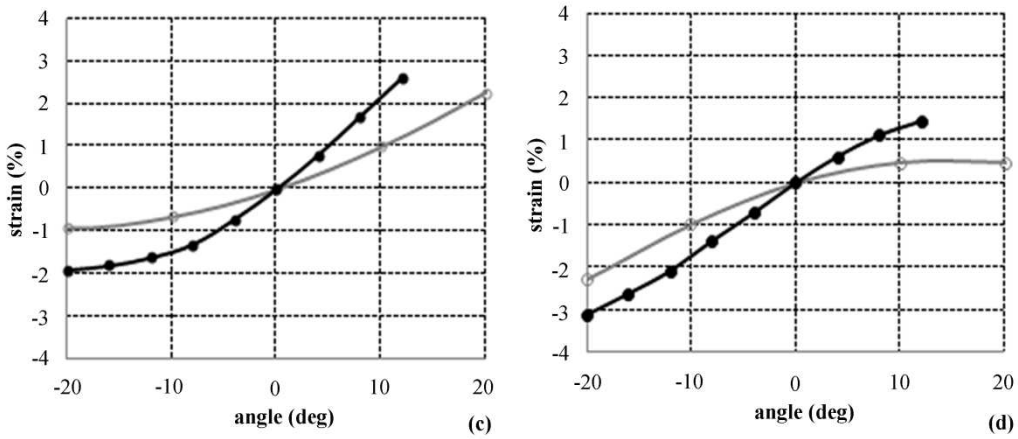

Figure 5.11. Comparison between numerical results (black line) and experimental data (grey line) (Ozeky et al. 2002) of the flexion angle-strain curve of several ligaments of the ankle: (a) ATFL,(b) PTFL, (c) CFL and (d) TCL. The Y axis indicated the strain and the X-axis indicated the dorsi/plantarflexion angle. The dorsiflexion and the plantarflexion angle are reported as plus and minus on the X-axis, respectively

The trend of the numerical results are in agreement with the experimental data. More specifically, the elongation of the ATFL occurs during plantarflexion, while the elongation of the PTFL, CFL and TCL occur during dorsiflexion movement.

The value of the strain is strongly affected by the value of the initial length. The length of the ligaments of the numerical model is similar to the mean value reported by Ozeky et al. 2002 (Table 5.1), but the experimental tests are reported for one of the twelve specimens used for the trials, even if no information is reported on it. The mean length (mm) and the standard deviation of the ligaments in the neutral position are reported:

	mean length	sd
ATFL	19.8	1.92
PTFL	23.7	3.1
CFL	29.9	4.24
TCL	27.7	3.76

Table 5.1. Length of the experimental ligaments in neutral position

5.3.2 Stress field

With regard to the numerical analyses of the dorsiflexion and plantarflexion movements of the ankle, the contours of the maximum principal stress are reported.

More specifically, in Figure 5.11 and Figure 5.12, results are reported for the collateral lateral ankle ligaments during dorsiflexion and plantarflexion motion, respectively. The movements are considered in a physiological range.

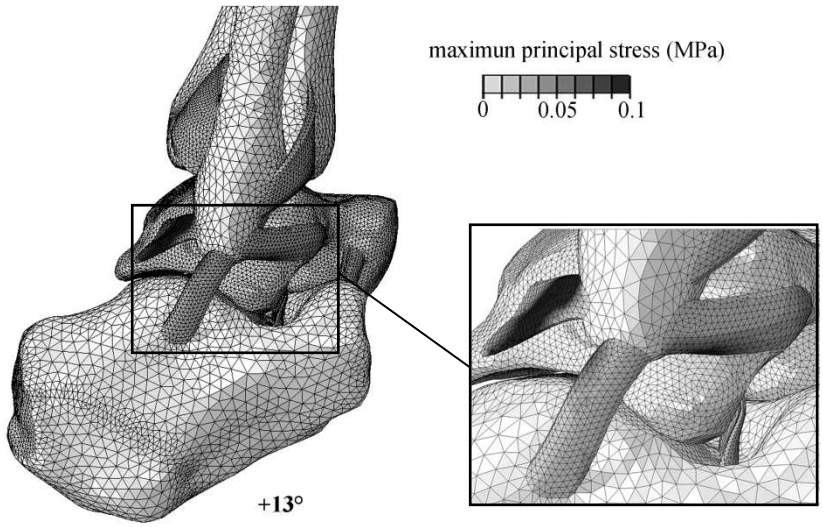

Figure 5.11. Numerical model results: maximum principal stress of the collateral lateral ankle ligaments for a dorsiflexion of 13°

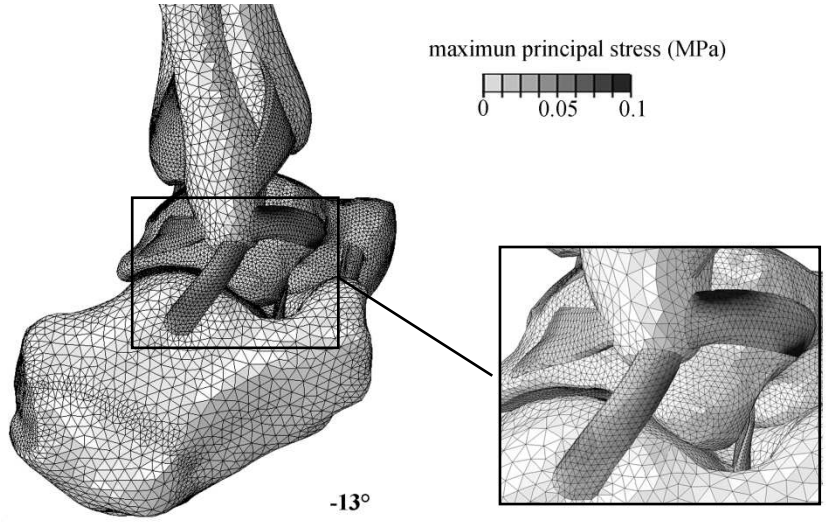

Figure 5.12. Numerical model results: maximum principal stress of the collateral lateral ankle ligaments for a plantarflexion of 13°

With regard to the deltoid ankle ligament, the contour of the maximum principal stress is reported in Figure 5.13 and Figure 5.14.

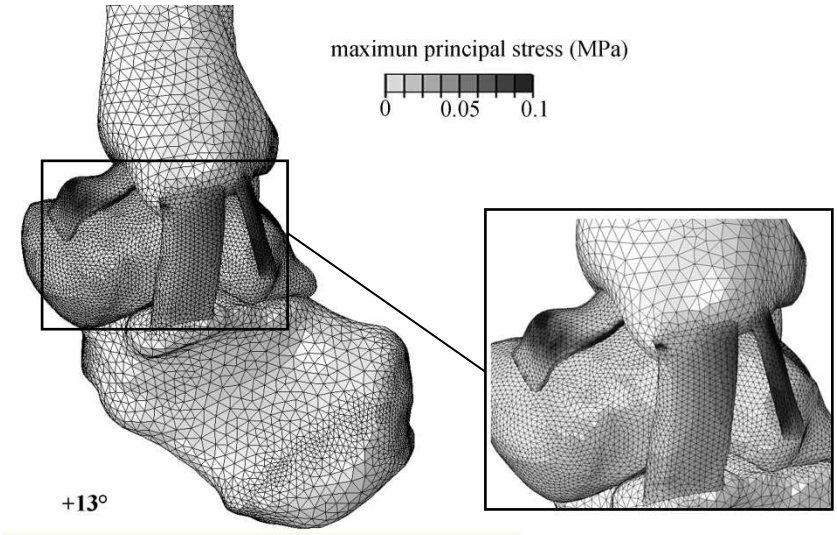

Figure 5.13. Numerical model results: maximum principal stress of the deltoid ankle ligament for a dorsiflexion of 13°

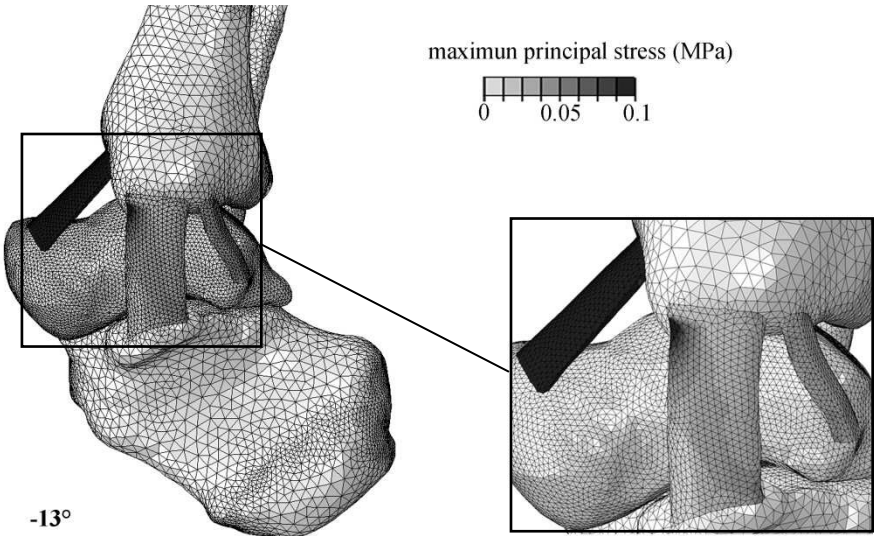

Figure 5.14. Numerical model results: maximum principal stress of the deltoid ankle ligament for a plantarflexion of 13°

The results show that during plantarflexion the stress field induced is mostly supported by the ATFL and ATTL, whereas during dorsiflexion the more active ligaments are the PTFL, the TCL and the PTTL.

These considerations are also in agreement with the results reported by Luo et al. 1997.

5.4 Numerical analysis of the ankle ligaments during the inversion movement

To provide an example, an interpretation of the characteristic phenomenon of inversion of the ankle joint is reported.

As reported in Chapter 3, a solid model of the right foot is developed. The model consists of 30 bony segments, including the distal segments of the tibia and fibula and the 28 foot bones. The model is obtained starting from CT and laser scanning data and using specific solid modelling software. The bony structures are merged with the encapsulated soft tissues to respect the conformation of the foot of the subject. The numerical model is obtained from the solid model with MSC-Patran software (MSC Software Corporation, Santa Ana, CA).

Bones and soft tissue regions are meshed with linear tetrahedral elements. With regard to the biomechanical properties, the bony segments are assumed to be orthotropic and linearly elastic (Natali et al., 2010a). The adipose tissues of the foot plant are modelled by developing and implementing a specific visco-hyperelastic constitutive model (Natali et al., 2010b) in the finite element code. The other soft tissue regions around the bony segments are considered to be homogeneous and are described with a standard almost-incompressible hyperelastic model (Goske et al., 2006). The ankle ligaments are described by means of the visco-hyperelastic model with the constitutive parameters obtained beforehand.

The inversion movement of the foot are reported in Figure 5.15. Figures 5.15a and 5.15b show the neutral configuration of the ankle and the displacement field after inversion, respectively. Figure 5.15c shows that the stress field induced is mostly supported by the lateral-collateral ligament complex with particular regard to ATFL and CFL. The results are proposed in a qualitative form and are in agreement with the results of other authors, in particular with Harmon 2004 and Van Den Bekerom et al. 2008, confirming that ankle sprain is mostly caused by damage to the ATFL and CFL ligaments, because of high tensile stress condition.

This example can attest the possibility offered by the present approach for an investigation of the ankle biomechanics in a more general sense, leading to the definition of the response under different conditions.

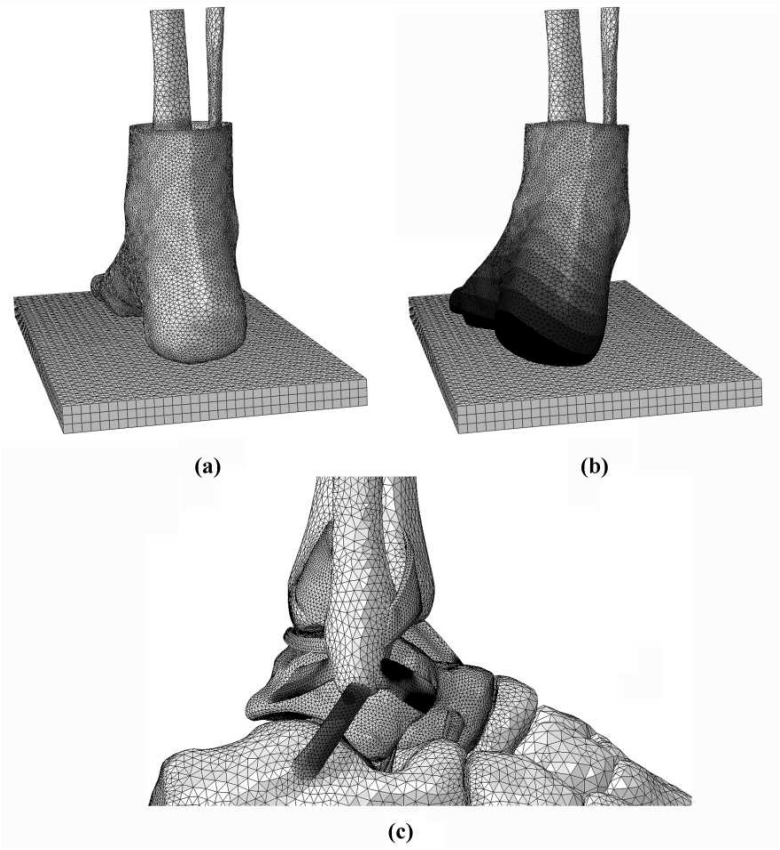

Figure 5.15. Numerical analysis of the inversion movement of the foot. (a) Neutral configuration and (b) displacements fields after inversion; for the latter configuration the contour of the maximum principal stress within ankle ligaments is reported (c)

The procedure developed in this work allows to evaluate the influence of each ligament in foot biomechanics. This kind of effort offers the possibility to interpret and analyse the ankle joint trauma.

More specifically, numerical analyses that interpret the movements of the foot with intact ligaments and after the rupture of the hindfoot ligaments could be performed. These kind of analyses can be developed with regard to several experimental tests reported in literature. In detail the biomechanical behaviour of the ankle joint is evaluated with intact ligaments and after the serial sectioning of the anterior talo-fibular and calcaneofibular ligament (Laiponte et al. 2007; Imhauser 2004; Ringleb 2003; Kovaleski et al. 2002; Rosenbaum et al. 1998) while the biomechanical behaviour of the subtalar joint is evaluated with intact ligaments and after the serial sectioning of the interosseus and cervical ligament (Kamiya et al. 2009).

5.5 References

Attarian D.E, McCrackin H.J., DeVito D.P., McElhaney J.H., Garrett W.E., 1985. Biomechanical characteristics of human ankle ligaments, Foot & Ankle, vol.6(2), pp. 54-58.

Funk J.R., Hall G.W., Crandall J.R., Pilkey W.D, 2000. Linear and quasi linear viscoelastic characterization of ankle ligaments, Journal of Biomechanical Engineering, vol. 122, pp. 15-22.

Goske S., Erdemir A., Petre M., Budhabhatti S., Cavanagh P.R., 2006. Reduction of plantar heel pressures: insole design using finite element analysis, Journal of Biomechanics, vol. 39, pp. 2363-2370.

Harmon G.K., 2004. The ankle examination, Primary Care, vol. 31, pp. 1025-1037.

Imhauser C.W., 2004. The Development and Evaluation of a 3-Dimensional, Image-Based, Patient-Specific, Dynamic Model of the Hindfoot, Doctoral thesis of Drexel University.

Kamiya T., Hideji K., Daisuke S., Eiichi U., Mineko F., Toshihiko Y., 2009. Mechanical stability of the subtalar joint after lateral ligament sectioning and ankle brace application. A biomechanical experimental study, The American Journal of Sports Medicine, vol. 37 (12), pp. 2451-2458.

Kovaleski J.E., Hollis J.M., Heitman R.J., Gurchiek L.R., Pearsall A.W., 2002. Assessment of ankle-subtalar joint complex laxity using an instrumented ankle arthrometer: an experimental cadaveric investigation, Journal of Athletic Training, vol. 37(4), pp. 467-474.

Lapointe S.J., Siegler S., Hillstrom H., Nobilini R.R., Mlodzienski A., Techner L., 1997. Changes in the flexibility characteristics of the ankle complex due to damage to the lateral collateral ligaments: an in vitro and in vivo study, Journal of Orthopedic Research, vol. 15, pp. 331-341.

Luo Z.P, Kitaoka H.B., Hsu H.C., Kura H., An K.N., 1997. Physiological elongation of ligamentous complex surrounding the hindfoot joints: in vitro biomechanical study, Foot & Ankle International, vol. 18(5), pp. 277-283.

Natali A.N., Carniel E.L., Pavan P.G., 2010a. Modelling of mandible bone properties in the numerical analysis of oral implant biomechanics, Computer Methods and Programs in Biomedicine, vol. 100(2), pp. 158-165.

Natali A.N., Fontanella C.G., Carniel E.L., 2010b. Constitutive Formulation and Analysis of Heel Pad Tissues Mechanics, Medical Engineering & Physics, vol. 32(5), pp. 516-522.

Ozeki S., Yasuda K., Kaneda K., Yamakoshi K., Takahiro Y., 2002. Simultaneous strain measurement with determination of a zero strain reference for the medial and lateral ligaments of the ankle, Foot & Ankle International, vol. 23(9), pp. 825-832.

Ringleb S.I., 2003. A three-dimensional stress MRI technique to quantify the mechanical properties of the ankle and subtalar joint – application to the diagnosis of ligament injuries, Doctoral thesis of Drexel University.

Rosenbaum D., Becker H.P., Wilke H.J., Claes L.E., 1998. Tenodeses destroy the kinematic coupling of the ankle joint complex. A three dimensional in vitro analysis of joint movement, Journal of Bone & Joint Surgery, vol. 80-B, pp. 162-168.

Siegler S., Udupa J.K., Ringleb S. I., Imhauser C. W., Hirsch B. E., Odhner D., Saha P. K., Okereke E. , Roach N**.,** 2005. Mechanics of the ankle and subtalar joints revealed through a 3D quasi-static stress MRI technique. Journal of Biomechanics, vol. 38(3), pp. 567-578.

Van Den Bekerom M.P.J., Oostra R.J., Alvarez P.G., Dijk N.V., 2008. The anatomy in relation to injury of the lateral collateral ligaments of the ankle: a current concepts review, Clinical Anatomy, vol. 21, pp.619-626.

CONCLUSIONS

This works deals with the constitutive formulation of ligaments tissue and presents a procedure for identifying constitutive parameters using experimental data, with the aim of developing a computational approach for investigating the actual biomechanical response. The preliminary definition of constitutive parameters is developed using an analytical model that is defined taking into consideration a fiber-reinforced visco-hyperelastic formulation and the boundary conditions of the uni-axial experimental tests performed on bone-ligament-bone specimens. The discrepancy between model results and experimental data is evaluated on the basis of a specific cost function, adopting a stochastic/deterministic procedure. The parameters evaluation is upgraded by means of numerical method, which allows to consider the real configuration of experimental samples and boundary conditions.

The numerical models of the bone-ligament-bone specimens are provided and the proposed visco-hyperelastic formulation is implemented. Numerical analyses are developed for different sets of parameters, which are evaluated starting from the preliminary set obtained by means of the analytical approach. The minimization of the discrepancy between experimental and numerical model results entails the definition of a reliable set of parameters.

The comparison between experimental and numerical results leads to the conclusion that the fiber-reinforced visco-hyperelastic constitutive model developed is able to interpret the mechanical response of the hindfoot ligaments. In agreement with experimental evidence, the constitutive formulation is capable of accounting for typical features of the mechanical behaviour of ankle ligaments tissue, such as non-linear elasticity, almost-incompressible behaviour, anisotropic configuration, and time-dependent phenomena.

The achieved sets of parameters for each ankle ligaments differ only for the hyperelastic parameters of the fibers. The results show that the ligaments of the hindfoot are composed by a similar ground matrix and the different mechanical responses are due to different collagen fibers conformations.

The procedure adopted is validated by means of numerical analyses that interpret experimental tests executed on the overall structure of the hindfoot and not only on bone-ligament-bone specimens. For this purpose, the numerical analysis of the dorsiflexion and plantarflexion of the hindfoot are performed and the strain of the central part of each ligament is evaluated. The numerical results are in agreement with experimental data confirming the accuracy of the procedure and the suitability of the constitutive parameters.

The procedure adopted offers the possibility of obtaining a proper evaluation of the biomechanical behaviour of the ligaments of the hindfoot under different loading condition. As an example, an interpretation of the characteristic phenomenon of inversion of the ankle joint is reported.

This work is the basis for the evaluation of the influence of each ligament in foot kinematics and biomechanics. More specifically, numerical analyses that interpret the movements of the foot with intact ligaments and after serial sectioning of the ankle ligaments can be performed. These kinds of analyses can be a procedure to interpret and analyse the ankle joint trauma such as severe sprains that involve complete tears of the anterior talofibular and calcaneofibular ligament.